Thèse de doctorat

Université de Limoges

ED 610 - Sciences et Ingénierie des Systèmes, Mathématiques, Informatique (SISMI)

Laboratoire XLIM - SRI

Thèse pour obtenir le grade de

Docteur de l'Université de Limoges

Discipline/ Spécialité: Electronique des Hautes Fréquences, Photonique et Systèmes/ Télécommunication

Présentée et soutenue par

Thai Bang HOANG

Le 11 Juillet 2019

INFRARED AND VISIBLE WIRELESS OPTICAL TECHNOLOGY FOR BODY SENSOR CONNECTIVITY

(Technologie optique sans fil infrarouge et visible pour la connectivité de capteurs corporels)

Thèse dirigée par **Anne JULIEN-VERGONJANNE**,

Codirigée par **Stéphanie SAHUGUEDE**

JURY:

M. Stéphane AZOU, Professeur, Ecole Nationale d'Ingénieurs de Brest (ENIB), Lab. STICC CNRS UMR 6285

M. Salah BOURENANNE, Professeur, Ecole Centrale de Marseille, Institut Fresnel CNRS UMR 7249

Mme. Anne JULIEN-VERGONJANNE, Professeure, ENSIL/ENSCI, XLIM CNRS UMR 7252

Mme. Stéphanie SAHUGUEDE, Maître de Conférences, ENSIL/ENSCI, XLIM CNRS UMR 7252

DEDICATE

FOR THE SCIENCE!

License CC BY-NC-ND 3.0

Rien n'est jamais perdu tant qu'il reste quelque chose à trouver

Pierre Dac

License CC BY-NC-ND 3.0

ACKNOWLEDGMENT

First of all, I would like to thank the members of committee Prof. Stéphane AZOU and Prof. Salah BOURENANNE spending time and working to validate my thesis.

At the time when my thesis is in a state of accomplishment, I would like to express my deep gratitude to Prof. Anne JULIEN-VERGONJANNE - my first supervisor from the bottom of my heart. I do not know how to say without the word THANK YOU VERY MUCH to her. Prof. Anne has supported me so much from the beginning until the last minute of my thesis. She has also guided me, encouraged me, and told me a lot of things not only in my field of study but also about the culture and lifestyle in France for me. As a result, all of these things have helped me overcome all the obstacles to go to the end of my Ph.D. period.

In addition, I would like to express my sincere thanks to my second supervisor Dr. Stéphanie SAHUGUEDE for her discussion, advice, and guidance to me, especially for the experiment part of the thesis.

On the one hand, during the time of my Ph.D. at Limoges University, I have known a lot of people: French and other countries who were with me had many enjoyable moments of life. I would like to express my gratitude to all of them which is an honor to know and discuss with them during this period.

On the other hand, I would like to express my gratitude to the Vietnamese friends: vợ chồng em Hiệu Hà, em Thiều, Thành, Tú, Nga. Thank you for all of you guys for your friendship, sharing emotions and motivations as well as encouragement during the time in Limoges City. All of these sweet memories will last long to the rest of my life.

Besides that, I have gained a lot of experiences about French cuisine, culture, and people with my second family in Limoges. I would like to express my thanks to one great man for all of these things: M. Jeans-Louis ROUSSEL.

Last but not least, I would like to express my special thanks to my families who are always by my side. I would like to give this thesis to my grandparents and my parents – bố Lý, mẹ Mai – for their advice, support, belief and endless love throughout my life. Special thanks go to my parents-in-law – bố Sinh, mẹ Trâm – for their encouragement and their wishes for my success and happiness.

Another thank I would like to express my appreciate to my dear sister- chị Ngọc, brother-in-law - anh Tùng, sister-in-law – hai em Minh Trang, Mai Anh for their help,

License CC BY-NC-ND 3.0

discussion and support during my years in France; and also my two “little naughty prince” Bo (Hoàng Long) and Bin (Hoàng Nguyên) who always have funny moments with me.

Finally, I would like to express my deepest gratitude to my loving wife and my “little princess” – Linh Nhâm and Susu (Kim Phụng) who are always with me during my Ph.D. years. They have sacrificed their lives in Vietnam to come to France to support me in pursuing my Ph.D. They have shared with me, helped my Ph.D. life become easier and overcome difficult moments during these years.

Limoges 07/2019

Doctorate candidate

HOANG THAI BANG

License CC BY-NC-ND 3.0

DROITS D'AUTEURS

Cette création est mise à disposition selon le Contrat : « **Attribution-Pas d'Utilisation Commerciale-Pas de modification 3.0 France** » disponible en ligne : *http://creativecommons.org/licenses/by-nc-nd/3.0/fr/*

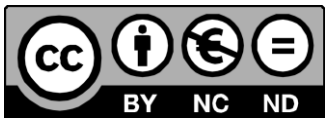

License CC BY-NC-ND 3.0

CONTENT

DEDICATE 2
ACKNOWLEDGMENT 4
DROITS D'AUTEURS 5
CONTENT 7
LIST OF ABBREVIATIONS 11
LIST OF FIGURES 14
LIST OF TABLES 20
GENERAL INTRODUCTION 21
CHAPTER I. INTRODUCTION TO OPTICAL WIRELESS COMMUNICATION 25
I.1. Background 25
I.2. Outdoor Optical Wireless Communication 27
I.2.1. Infrared FSO 27
I.2.2. UV Communications 28
I.2.3. VLC 28
I.3. Indoor Optical Wireless Communications 30
I.3.1. Infrared (IR) 30
I.3.2. Visible Light Communication (VLC) 32
I.4. OWC applied to health monitoring 34
I.5. Conclusion 36
CHAPTER II. TECHNICAL CHARACTERISTICS OF INDOOR OPTICAL WIRELESS COMMUNICATION 39
II.1. Introduction 39
II.2. Intensity Modulation and Direct Detection (IM/DD) 39
II.3. Optical Components 41
II.3.1. Optical sources 41
II.3.1.1. IR LED 41
II.3.1.2. VLC LED 46
II.3.1.3. Safety considerations 49
II.3.2. Optical receivers 51

License CC BY-NC-ND 3.0

II.4. Optical propagation 54
II.4.1. Types of OWC links 54
II.4.2. LOS links 55
II.4.3. NLOS link 56
II.5. Noise 58
II.5.1. Ambient light noise 58
II.5.2. Photo-detector noise 59
II.5.3. Receiver thermal noise 60
II.6. Digital modulation techniques 60
II.6.1. Single-carrier modulations 61
II.6.2. Multiple-carrier modulations 62
II.7. Conclusion 63
CHAPTER III. MOBILE IR CHANNEL BEHAVIOR 65
III.1. Introduction 65
III.2. Channel simulation tools 65
III.2.1 Monte-Carlo Ray Tracing methods 66
III.2.2 Introduction about RaPSor 66
III.2.2.1 Simulation scene file 67
III.2.2.2 Run RaPSor 70
III.3. Simulation of the IR channel 70
III.3.1. Definitions 71
III.3.2. Single-Input Single-Output (SISO) configuration in an empty room 72
III.3.3. Single-Input Multiple-Output (SIMO) in an empty room 77
III.3.3.1. Study of scenario (a) 79
III.3.3.2. Study of scenario (b) 83
III.3.4 Single-Input Multiple-Output (SIMO) with body presence 86
III.3.4.1 Body model 86
III.3.4.2. Transmitter orientation 90
III.3.4.3. Tx half-power angle 91
III.3.4.4. Rx orientation 92
III.3.4.5. Tx Height on the body (H_T) 93
III.3.5. Conclusion on IR Channel 94
III.4. Experimental validation 95
III.4.1. Introduction 95

License CC BY-NC-ND 3.0

III.4.2. Experimental setup description 95
III.4.2.1. Emitter / receiver hardware description 95
III.4.2.2. Scenario description 96
III.4.2.3. PER determination 98
III.4.3. Results with robotic platform 100
III.4.3.1. Impact of Rx orientation – m =45 100
III.4.3.2. Impact of Tx half power angle 101
III.4.4. Results with the human body 101
III.4.4.1. Impact of Tx half-power angle and height H_T – fixed R_X orientation 45° 101
III.4.4.2 Impact of the body – comparison with the robotic platform 102
III.4.5. Comparison with scenario (a) 103
III.4.6. PER evaluation using time of arrival 105
III.4.7. Results at higher baud rates 106
III.5. Conclusion 107
CHAPTER IV. MOBILE VLC CHANNEL BEHAVIOR 109
IV.1. Introduction 109
IV.2. Description of visible downlink configuration 109
IV.3. Simulation of Visible channel 110
IV.3.1. Impact of body 113
IV.3.2. Impact of Rx orientation 114
IV.3.3. Impact of distance to body 116
IV.3.4. Comparison of VLC and IR channel behavior 116
IV.4. Experiments 118
IV.4.1. Setup description 118
IV.4.2. Experimental results 121
IV.5. Conclusion 124
CHAPTER V. BODY SENSOR-BASED MONITORING SYSTEM PERFORMANCE 127
V.1. Introduction 127
V.2. IR uplink performance 128
V.2.1. Definitions 128
V.2.2. Performance analysis 129
V.3. Visible downlink performance 133
V.4. Overall performance of IR uplink and visible downlink 135

License CC BY-NC-ND 3.0

V.4.1. Definitions 135
V.4.2. Results analysis 135
V.4. Conclusion 139
CONCLUSION AND PERSPECTIVE 141
REFERENCES 147
APPENDIX 01: Matlab program corresponding to the creation of a scene in RaPSor 159
APPENDIX 02: Matlab program to create a script including moving object 163
APPENDIX 03: Description of 3D body 165
APPENDIX 04: Description of the 3D environment 169
APPENDIX 05: Header used in Appendix 02 171
APPENDIX 06: Matlab program corresponding to extraction of .xml results from RaPSor 172
APPENDIX 07: Figures of Chapter V for 60° oriented receivers 174

License CC BY-NC-ND 3.0

LIST OF ABBREVIATIONS

Abbreviation	Full name
APD	Avalanche Photo-Diode
AWGN	Additive White Gaussian Noise
BER	Bit Error Rate
BRDF	Bidirectional Reflectance Distribution Function
CDF	Cumulative Density Function
CIE	International Commission on Illumination
CPU	Central Processing Unit
CSK	Color Shift Keying
DC	Direct Current
DD	Direct Detection
DMT	Discrete Multi Tone
ECG	Electrocardiography
EGC	Equal Gain Combining
FOV	Field Of View
FSO	Free Space Optics
FTDI	Future Technology Devices International
GaAs	Gallium Arsenide
GPS	Global Positioning Systems
IEEE	Institute of Electrical and Electronics Engineers
IFFT	Inverse Fast Fourier Transform
IMDD	Intensity Modulation Direct Detection
IoT	Internet of Things
IR	Infrared
IrDA	Infrared Data Association
ISI	Inter Symbol Interference
LAN	Local Area Network
LED	Light Emitting Diode
LOS	Line Of Sight
LTE	Light Transport Equation

License CC BY-NC-ND 3.0

MC	Monte Carlo
MCG	Monte Carlo Gathering
MCMC	Markov Chain associated to the Monte Carlo method
MCRT	Monte Carlo Ray Tracing
MCS	Monte Carlo Shooting
MIMO	Multiple Input Multiple Output
MRC	Maximum Ratio Combining
NLOS	Non Line Of Sight
NRZ	Non Return to Zero
OFDM	Orthogonal Frequency Division Multiplexing
OLED	Organic LEDs
OOK	On Off Keying
OWC	Optical Wireless Communication
PAM	Pulse Amplitude Modulation
PAN	Personal Area Network
PAPR	Peak to Average Power Ratio
PC	Phosphor Converted
PD	Photodiode
PDF	Probability Density Function
PER	Packet Error Rate
PHY	Physical Layer
PIN	Positive Intrinsic Negative
PoE	Power of Ethernet
PPM	Pulse Position Modulation
PWM	Pulse Width Modulation
RAM	Random Access Memory
RF	Radio Frequency
RG	Risk Groups
RG	Ray Gathering
RGB	Red Green Blue
RMS	Root Mean Square
RS	Ray Shooting
RZI	Return to Zero Invert

License CC BY-NC-ND 3.0

SC	Selection Combining
SIMO	Single Input Multiple Output
SISO	Single Input Single Output
SNR	Signal to Noise Ratio
TIA	Transimpedance Amplifier
UV	Ultra-Violet
VLC	Visible Light Communication
VLCC	Visible Light Communication Consortium
VPPM	Variable PPM
WDM	Wavelength Division Multiplexing

License CC BY-NC-ND 3.0

LIST OF FIGURES

Figure 1.1. The exponential increase in the need for connected devices compared to population increase between the year 2003 and 2020 [3] 25
Figure 1.2. Electromagnetic spectrum [4] 26
Figure 1.3. Inter-buildings connections, source: [18] 27
Figure 1.4. Example of NLOS UV communication, source: [15] 28
Figure 1.5. Example of outdoor VLC applications, source: [24] 29
Figure 1.6. Example of indoor optical wireless network in "Broadband Room Service by Light," Scientific American Journal July 2007 31
Figure 1.7. Illustration of VLC luminaire [17] 32
Figure 1.8. Illustration of Li-Fi concept [44] 34
Figure 2.1. Block diagram of a typical IM/DD optical wireless system 40
Figure 2.2. Relative radiant Power (%) vs. wavelength; LED TSAL6400 [88] 42
Figure 2.3. Illustration of differential solid angle 42
Figure 2.4. Central intensity I_0 and intensity I_Θ 43
Figure 2.5. Generalized Lambertian pattern of a point source with *m*=3 [89] 43
Figure 2.6. Normalized intensity vs Lambertian order m 44
Figure 2.7. Radiant Intensity vs. Forward Current of LED TSAL6400 [31] 44
Figure 2.8. Illustration of surface swept out by a solid angle **Ω** 45
Figure 2.9. Trichromatic white LED with associated emission spectrum [91] 46
Figure 2.10. PC white LED with associated emission spectrum [91] 47
Figure 2.11. Eye sensitivity function and luminous efficacy for photopic vision [95] 48
Figure 2.12. Penetration of optical radiation into the eye [96] 49
Figure 2.13. Biological hazards considered with the standard IEC/EN 62471 [87] 50
Figure 2.14. Risk Groups of the standard IEC/EN 62471 [87] 50
Figure 2.15. Illustration of FOV receiver 52
Figure 2.16. Basic scheme of TIA 53
Figure 2.17. OWC link configurations: (a) directed LOS (b) non-directed LOS (c) diffuse [16] 54

License CC BY-NC-ND 3.0

Figure 2.18. LOS link and reflected path geometry 56
Figure 2.19. Material reflectivity for (a) IR and (b) visible domains [85] 58
Figure 2.20. Spectral ambient light source impact on photodiode [111] 59
Figure 2.21. Example of OOK-NRZ and 2-PPM signals 62
Figure 3.1. Description of RaPSor steps for channel simulation 67
Figure 3.2. Parameters for scene simulation file 68
Figure 3.3. Example of surface definition and associated XML code 68
Figure 3.4. Illustration of Transmitter, Receiver and object 3D definition. 69
Figure 3.5. Example of 2D interface of RaPSor 70
Figure 3.6. Scene geometry definition 71
Figure 3.7.(a). Example of impulse response for Tx close to room center 74
Figure 3.7.(b). Example of impulse response for Tx at the room corner 74
Figure 3.8.(a). Mean excess delay for 50 Tx positions 75
Figure 3.8.(b). RMS delay spread for 50 Tx positions 75
Figure 3.9. $PDF(H0)$ as a function of number of transmitter's position 76
Figure 3.10. The CDF as a function of number of transmitter's position 76
Figure 3.11. LED panel examples [131] 78
Figure 3.12. Illustration of scenarios (a) and (b) for IR channel 78
Figure 3.13. $PDF(H0)$ for scenario (a) as a function of *m* values; H_T=1.5m; α=90° 80
Figure 3.14. $CDF(H0)$ for scenario (a) as a function of *m* values; H_T=1.5 m; α=90° 81
Figure 3.15. $CDF(H0)$ for scenario (a) as a function of *m* values; H_T=0.2m 82
Figure 3.16. $CDF(H0)$ for scenario (a) as a function of H_T values; *m*=2 83
Figure 3.17. $CDF(H0)$ for scenario (b) as a function of Rx orientation angle α, H_T=1.5m, *m*=2 84
Figure 3.18. $CDF(H0)$ for scenario (b) as a function of *m*; α=45°, H_T=1.5m 85
Figure 3.19. $CDF(H0)$ for scenario (b) as a function of H_T *;* *m*=2; (i): α=45°; (ii): α=60° 85
Figure 3.20. Comparison of $CDF(H0)$ for scenario (a) and (b) H_T=0.2m; 1.5m*;* *m*=2; α=45°; α=60°, nobody presence. 86
Figure 3.21. Model of human body in 3D dimension 87

License CC BY-NC-ND 3.0

Figure 3.22. Comparison of $CDF(H0)$ for scenario (a) and (b) with 3D body (ρ=0.1); H_T=0.2m; 1.5m; *m*=2; α=45°; α=60° 88

Figure 3.23. Comparison of $CDF(H0)$ for scenario (b) with 2D and 3D body (ρ=0.1); H_T=0.2m; 1.5m; *m*=2; α=45° 89

Figure 3.24. $CDF(H0)$ scenario (b) as a function of body reflectivity ρ, H_T=0.2m and 1.5m, *m*=2; α=45° 90

Figure 3.25. Orientation angles of Tx 91

Figure 3.26. $CDF(H0)$ scenario (b) as a function of Tx orientation; 3D body with ρ=0.1, H_T=0.2m and 1.5m, *m*=2; α=45° 91

Figure 3.27. $CDF(H0)$ scenario (b) as a function of *m*; 3D body with (a) ρ =0.1 (b) ρ=0.5; (c) ρ=0.9, H_T=0.2m and 1.5m; α=45° 92

Figure 3.28. $CDF(H0)$ scenario (b) as a function of α; 3D body with ρ=0.1, (a): H_T= 1.5m; (b): H_T= 0.2m; *m*=2 93

Figure 3.29. $CDF(H0)$ scenario (b) as a function of H_T; 3D body with ρ=0.1; *m*=2; α=45° . 94

Figure 3.30. Receivers at the central panel, example of printed pieces to fix orientation 97

Figure 3.31. Switch connection and positions of receivers in the room with their numbering 97

Figure 3.32: Experimental setup, (a): sensor attached on the body (b): sensor attached on robotic platform 98

Figure 3.33: Experimental setup with the portable structure with FTDI receiver and Python program 99

Figure 3.34. Experimental results with different values of Rx orientations, *m*=45; HT=0.2m 100

Figure 3.35. Experimental results with different half-power angles *m*=5 and *m*=45, H_T=0.2m 101

Figure 3.36. Experimental results with human body, different values of H_T, different half-power angles m=5 and m=45, Rx orientation 45° 102

Figure 3.37. Experimental results with Tx worn by a human and the robotic platform, H_T=0.2m, *m*=45 102

Figure 3.38. Experimental results with Tx worn by a human and the robotic platform, H_T=0.2m, *m*=5 103

License CC BY-NC-ND 3.0

Figure 3.39. Experimental PER for scenario (b) with Rx orientations of 45° and 90° and for scenario (a) with perpendicular receivers; optical source m=45 ($\varphi 1/2$=10°). 104
Figure 3.40. Experimental PER for scenario (b) with Rx orientations of 45° and for scenario (a) with perpendicular receivers; optical source m=5 and m=45. 104
Figure 3.41. New sensor to do the experiment 106
Figure 4.1. Illustration of VLC downlink scenario 110
Figure 4.2. VLC downlink definition 111
Figure 4.3. Evolution of some body-related ρ according to the light wavelength [132] 112
Figure 4.4. Rx orientation changes definition 112
Figure 4.5. Visible channel $CDF(H0)$; case no body and 3D body with ρ=0.1; α=φ=0° 114
Figure 4.6. Visible channel $CDF(H0)$; case no body and 3D body with ρ=0.1; random values of Rx orientation angles (φ;α) 115
Figure 4.7. Visible channel $CDF(H0)$; 3D body with ρ=0.1; 0.5; 0.9; random values of Rx orientation angles (φ;α) 115
Figure 4.8. Visible channel $CDF(H0)$ as a function of distance to the body D_b; 3D body with ρ=0.1; random values of Rx orientation angles (φ; α) 116
Figure 4.9. IR scenario (b) and Visible channel $PDF(H0)$; 3D body with ρ=0.1; $H_{T\text{-}VLC}$=1.2m; $H_{T\text{-}IR}$=0.2m 117
Figure 4.10. IR scenario (b) and Visible channel $CDF(H0)$; 3D body with ρ =0.1; 118
$H_{T\text{-}VLC}$=1.2m; $H_{T\text{-}IR}$=0.2m 118
Figure 4.11. VLC luminaire and LiFi dongle from starter kit of PureLiFi [44] 119
Figure 4.12. LiFi network 120
Figure 4.13. Photos of device for the control of receiver orientation 120
Figure 4.14. Illustration of experiment protocol 121
Figure 4.15. Received power at 400nm without and with body presence 122
Figure 4.16. DC gain of visible channel without and with body presence 122
Figure 4.17. Received power at 500nm, 600nm and 700nm without and with body presence 123
Figure 4.18. Received power at 500nm at different Rx locations without (a) and with (b) body 124

License CC BY-NC-ND 3.0

Figure 5.1. Illustration of body sensor-based monitoring system. 127

Figure 5.2. Outage probability of IR channel scenario (b), Rx orientation 45°, m=2, $Ht - IR = 1.5m$, body reflectivity ρ =0.1; $Rb = 1Mbps$ 130

Figure 5.3. Outage probability of IR channel scenario (b), Rx orientation 60°, m=2, $Ht - IR = 1.5m$, body reflectivity ρ =0.1; $Rb = 1Mbps$ 130

Figure 5.4. $SNR0$ versus emitted power $Pt - IR$; IR channel scenario (b), Rx orientation 45° and 60°, m=2, $Ht - IR = 1.5m$, body reflectivity ρ =0.1; $Rb = 1Mbps$ 131

Figure 5.5. Outage probability of IR channel scenario (b), Rx orientation 45°, m=2, $Ht - IR = 0.2m$, body reflectivity ρ =0.1 ; $Rb = 1Mbps$ 132

Figure 5.6. Outage probability of IR channel scenario (b), Rx orientation 45°, m=2, $Ht - IR = 0.2m$, $Pt - IR = 100mW$;body reflectivity ρ =0.1;0.5;0.9; $Rb = 1Mbps$ 132

Figure 5.7. Outage probability of VLC channel, random Rx orientation, m=1, $Ht - VLC = 1.2m$;body reflectivity ρ =0.1; $Rb = 1Mbps$ 133

Figure 5.8. Outage probability of VLC channel, random Rx orientation, m=1, $Ht - VLC = 1.2m$; $Rb = 1Mbps$;body reflectivity ρ =0.1;0.5;0.9 134

Figure 5.9. Evolution of IR and VLC emitted powers for 3 given values of $Pout$; body reflectivity ρ=0.1, Height $HT - IR$=0.2m and $HT - IR$=1.5m; data rate $Rb = 1Mbps$..... 136

Figure 5.10. Evolution of, $Pt - IR - min$ (in plain lines) and $Pt - VLC - max$ (in dotted lines) for 3 given values of $Pout$ as a function of body reflectivity ρ Height $HT - IR$ =0.2m; $Rb = 1Mbps$. 137

Figure 5.11. Evolution of, $Pt - IR - max$ (in plain lines) and $Pt - VLC - min$ (in dotted lines) for 3 given values of $Pout$ as a function of body reflectivity ρ, Height $HT - IR$=0.2m; $Rb = 1Mbps$. 138

Figure 5.12. Evolution of, data rate for IR and VLC links for 2 given values of $Pout$; $Pt - IR$=300mW and $Pt - VLC$=2W ; body reflectivity ρ=0.1; Height $HT - IR$=0.2m 139

Figure corresponding to 5.5. Outage probability of IR channel scenario (b), Rx orientation 60°, m=2, $Ht - IR = 0.2m$, body reflectivity ρ=0.1; $Rb = 1Mbps$ 174

Figure corresponding to 5.6. Outage probability of IR channel scenario (b), Rx orientation 60°, m=2, $Ht - IR = 0.2m$, $Pt - IR = 100mW$;body reflectivity ρ=0.1;0.5;0.9; $Rb = 1Mbps$ 174

License CC BY-NC-ND 3.0

Figure corresponding to 5.9. Evolution of IR and VLC emitted powers for 3 given values of $Pout$; Rx orientation 60°, m=2, body reflectivity ρ=0.1, Height $HT-IR$=0.2m and $HT-IR$=1.5m; data rate $Rb=1Mbps$..... 175

Figure corresponding to 5.10. Evolution of, $Pt-IR-min$ (in plain lines) and $Pt-VLC-max$ (in dotted lines) for 3 given values of $Pout$ as a function of body reflectivity ρ Height $HT-IR$ =0.2m; Rx orientation 60°, $Rb=1Mbps$..... 175

Figure corresponding to 5.11. Evolution of, $Pt-IR-max$ (in plain lines) and $Pt-VLC-min$ (in dotted lines) for 3 given values of $Pout$ as a function of body reflectivity ρ, Rx orientation 60°, Height $HT-IR$=0.2m; $Rb=1Mbps$. 176

Figure corresponding to 5.12. Evolution of, data rate for IR and VLC links for 2 given values of $Pout$; $Pt-IR$=300mW and $Pt-VLC$=2W; Rx orientation 60°, body reflectivity ρ=0.1, Height $HT-IR$=0.2m 176

License CC BY-NC-ND 3.0

LIST OF TABLES

Table 3.1. SISO configuration –empty room 73
Table 3.2. SIMO configuration scenario (a) – empty room 79
Table 3.3. Relation between half power angle and *m* value 80
Table 3.4. SIMO configuration scenario (b) – empty room 83
Table 3.5. Experimental PER results versus baud rate 106
Table 4.1. Parameters for VLC downlink channel simulation 112

License CC BY-NC-ND 3.0

GENERAL INTRODUCTION

In recent years, the emergence of mobile devices such as smartphones has radically changed our daily lives. These devices allow many services and people have the "need" to be connected at any time and everywhere to different applications. The consequences are growing demand for mobile connectivity with higher and higher data rates, high quality of service and security. This trend is accelerating with the emergence of the Internet of Things (IoT), which is expected to connect more than 30 billion objects by 2025.

To match the requirements of future wireless networks, various solutions such as network densification with the new 5G standard are currently studied and proposed. Regardless of the increase in capacity, much more bandwidth will be required to cope with the expected growth in data traffic. In today's wireless systems, (cellular, Wi-Fi), the dominant RF technology is deployed in frequency bands generally below 6 GHz. However, this spectral domain is almost entirely occupied and much regulated. One solution may be to increase the carrier frequency with the use of millimeter bands but also of the optical domain, which is not licensed.

In particular, the large-scale availability of light-emitting diodes (LEDs) has led to the development of a new type of communication, the so-called visible light communication (VLC). LEDs modulated at very high speed, invisible to the human eye, are used both for their main purpose which is the lighting but also to communicate. VLC is a category of Optical Wireless Communications (OWC) that includes infrared and ultra-violet communications as well as visible light.

OWC technology offers many advantages. As a supplement to RF networks, this is an answer to wireless network saturation. In addition, because of the abundant optical spectrum, the achievable transmission speed is theoretically much faster than the RF one. This property is the basis of LiFi technology proposed for high-speed connectivity using visible light. This technology is particularly ideal for indoor environments because lighting systems are already installed. Besides, optical rays do not pass through walls, which makes it much easier to secure a network.

On the other hand, RF use can present some limitations concerning health impact. In 2011, the World Health Organization classified radio frequencies as “possibly carcinogenic”. As OWC does not interfere with RF devices, it can be safely used in many sensitive

License CC BY-NC-ND 3.0

applications, especially for medical monitoring. Actually, OWC can be used for real-time monitoring and report of patient movement and vital signs without the need for wires. This is the context of the studies presented in the Thesis.

For many years, the OWC technology has been used in indoor and outdoor contexts and we present in the first Chapter the different advantages, challenges and applications for infrared, visible and ultraviolet bands. We also provide state-of-the-art around indoor medical surveillance applications based on portable sensors. We note that there are still many issues related to the impact of the patient's body, sensor location, and mobility that have not been fully clarified. The objectives and motivations of the thesis are given in the conclusion of this chapter.

The proposed system consists of two devices worn by the patient and a central ceiling lighting. One of the worn devices is coupled to the medical sensor and can transmit data via infrared. The other device is, for example, a smartphone capable of decoding VLC data. The luminaire includes both infrared receivers and a VLC transmitter. The use of IR and VLC technologies allow avoiding interferences between uplink and downlink. In addition, using visible uplink could cause discomfort to the users.

Thus, our goal is to study the robustness of infrared and visible technologies with regard to the effect of the patient's body, the position of the body sensor and the patient's movement in the defined environment. The ultimate goal is to determine an overall performance of the link between the sensor and the smartphone.

Chapter II introduces the different technical concepts of infrared and visible transmissions with regard to front-ends, noise, link configuration, and modulations. We define in particular the studied configuration which is non-directed and non-line-of-sight (NLOS) as well as the physical and geometrical parameters of the transceivers to be optimized. To this end, we adopt an approach of theoretically studying the random behavior of transmission channels related to patient mobility for different characteristics of the transceivers. This is complemented by experiments to validate the conclusions.

Firstly, Chapter III deals with the analysis of the infrared channel. The theoretical study is based on the statistical distribution of the channel gain obtained from optical propagation simulations. The simulation tool is presented briefly. The software used is called RaPSor and has been developed in the XLIM laboratory for several years. It is based on Monte-Carlo and Ray-Tracing methods. We use it to model and simulate a 3D environment including transceivers

License CC BY-NC-ND 3.0

features. To model the impact of the human body, we also define a 3D object with reflectance properties. Each simulation provides the impulse response of the modeled link configuration.

The infrared transmission scenario is a single input-multiple output (SIMO) configuration with selection combining technique. The transmitter is carried on the patient's body and four receivers are considered at the corners of a lighting panel in the center of the ceiling. The key parameters to be optimized are the half-power angle of the source and the orientation of the receivers according to the position of the transmitter on the body. This scenario is compared to a more traditional spatial diversity configuration where the four receivers are uniformly distributed over the ceiling.

The results show the interest of the proposed scenario. We determine the optimal parameters taking into account the effects of blockages due to the presence of the body of the patient carrying the transmitter, particularly in the case where the sensor is close to the ground, for example, worn at the ankle.

The last part of Chapter III is devoted to the experimental validation of the theoretical conclusions about the channel behavior with respect to the orientation angles of the receivers and the half-power angle of the source. We also present the results of the tests performed to show the impact of the body. Then compare the packet losses for a sensor placed on a low-height mobile platform and for a sensor at the ankle of the human body.

All the results show that it is essential to model the presence of the body to determine the performance of the IR uplink.

In Chapter IV, the aim is to study the behavior of the downlink visible channel between a centrally LED lighting and a receiver placed at a given position in front of the patient. Theoretical analysis is conducted as before based on the simulations provided by RaPSor taking into account the 3D modeling of the patient's body.

In the case of the visible channel, the impact of the changes in orientation of the worn receiver related to the mobility of the patient is very important, unlike the case of the infrared channel. To complete, experiments conducted with commercially available LiFi products confirm this behavior.

Finally, the performance of the all-optical communication system for body-sensor medical applications is theoretically established in Chapter V.

Performance of both links, firstly separately, then jointly is analyzed in terms of outage probability taking into account the IR and visible channel statistics established in the previous

License CC BY-NC-ND 3.0

chapters. The main blocking events are due to movements and mobility of the patient in the environment, the position of the communicating sensor and optical reflectivity property of the body.

Considering a data rate of 1 Mbps which is a classic requirement for a large category of health-related sensors, we discuss the results for OOK modulation with BER of 10^{-9} for both links. The required IR and VLC powers to satisfy a given quality of service are determined.

Then we also investigate the maximum data rates for the minimal required powers in order to conclude on the system potentialities for body-sensor monitoring.

The thesis document ends with a general conclusion about the work and the associated scientific publications. Different perspectives are also proposed.

License CC BY-NC-ND 3.0

CHAPTER I. INTRODUCTION TO OPTICAL WIRELESS COMMUNICATION

I.1. Background

The world of telecommunications is facing rapid growth in the use of mobile data, and anticipates even more in the future: many trends such as 5G and the Internet of Things (IoT) lead to the increasing use of the spectrum [1], [2]. As can be seen in Figure 1.1, in the year 2010, there were already more devices connecting to the internet than people on earth. It has been predicted that the number of connected devices will exceed 50 billion by 2020 only for indoor application [3]. Therefore, the available radio bandwidth is exhausted, wireless devices begin to interfere in this overloaded radio spectrum, and high capacity radio consumes a lot of power.

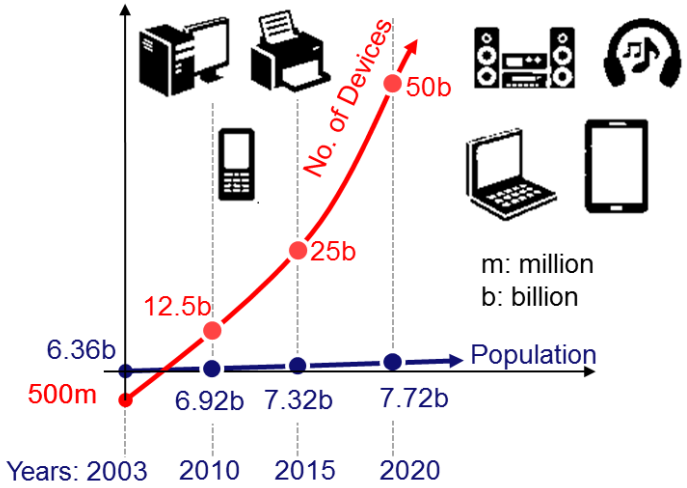

Figure 1.1. The exponential increase in the need for connected devices compared to population increase between the year 2003 and 2020 [3]

Thanks to the large bandwidth of its spectrum optics specifically in visible and infrared ranges could be an option that would help release the pressure on the radio spectrum currently used for communications [4].

The optical spectrum is much larger than the RF one as it covers the range from about 300 GHz to 790 THz (see Figure 1.2). Up to now, it is mostly unused for wireless data transmission. In addition, there is no electromagnetic interference with the systems operating in the radio spectrum. Another property of optical wireless links with several beneficial consequences is that the light waves do not penetrate through the surfaces. In indoor environments, this intrinsically defines a room as a communication cell. The same optical

License CC BY-NC-ND 3.0

frequencies can, therefore, be used in different rooms, increasing the network capacity. Another advantage over the radio related to confinement is better security against eavesdropping.

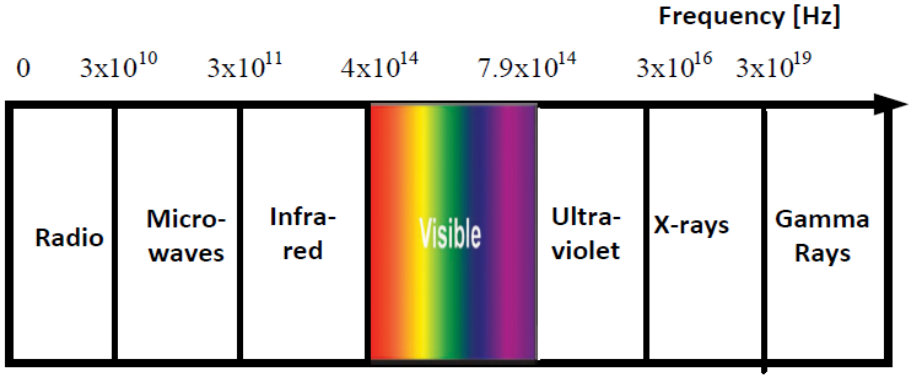

Figure 1.2. Electromagnetic spectrum [4]

The first optical wireless system has been invented by Alexander Graham Bell in 1880 [5]. His invention allowed to transmit the sound on a beam of light and named "photophone" over a distance more than 200 m. The idea of optical wireless communication (OWC) became then interesting again in the 20th century with the inventions of the laser [6], IR Light Emitting Diode (LED) and fiber optics [7], [8].

Infrared (IR) links uses transmission within the wavelength range (750-1600 nm) that is invisible to the human eye [9], [10]. For outdoor applications, infrared technology is called free-space optics (FSO), while the term OWC is usual for indoor.

Today, there is also more and more research in the field of visible light communication from 380 nm to 780 nm (VLC) [11]–[14]. This is related to the penetration of light emission diodes (LEDs) for lighting, which by their switching properties also makes it possible to use them for communication functions. As illumination devices are installed almost everywhere, VLC might be applied to various indoor and outdoor applications.

Finally, ultraviolet (UV) spectrum in UV-C band (100-280nm) can also be used as propagation media. UV technology allows high-data-rate non-line-of-sight (NLOS) and line-of sight (LOS) optical communication links [15].

There exist several literature reviews dealing with different aspects and classifications of optical technology for wireless communications [9]–[17].

In this chapter, we focus on optical technology according to the outdoor /indoor classification. The main advantages, challenges and applications are briefly presented for IR,

License CC BY-NC-ND 3.0

UV and visible ranges before concluding with regard to the motivations of the thesis concerning IR and visible use for indoor scenario and medical context.

I.2. Outdoor Optical Wireless Communication

I.2.1. Infrared FSO

The invention of the laser allowed the first developments of FSO in the 1970s [6]. The main applications were point-to-point with Line-Of-Sight (LOS) configurations because of laser narrow bandwidth. However, the progress of optical fiber systems in the next two decades made these preferable for long-distance optical transmission. Research around FSOs has slowed down except in the space and military domains, which permitted to continue technological progress in their fields.

Today, terrestrial FSO deployment offers a cheap and quick way to provide to customer high data rates up to 10Gbps over distances of several km (inter-buildings links as shown in Figure 1.3) and many commercial products are available [18]. This technology operates at wavelengths of 850 nm, 1300 nm and 1550 nm corresponding to the optical communications windows. In addition, to building a number of other outdoor scenarios are applied as the ground to vehicles and trains, vehicle to vehicle, or disaster recovery/temporary links [19]. In addition, to terrestrial applications, there is still a lot of activity around very long distance as in deep space transmissions, satellite networks, and ground to satellite [20].

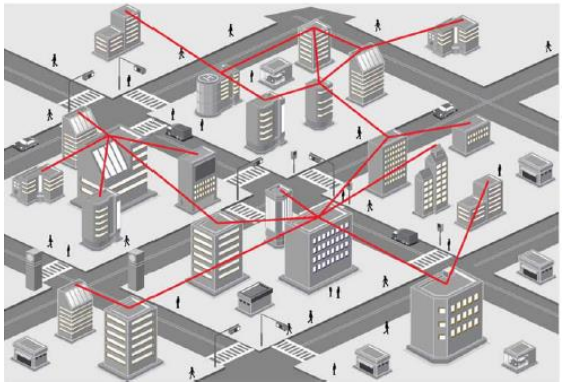

Figure 1.3. Inter-buildings connections, source: [18]

The major technical challenge of FSO is related to atmospheric channel as a propagating medium. FSO reliability suffers from atmospheric turbulence-induced fading and sensitivity to weather conditions. To improve performance, several methods and techniques derived from RF

License CC BY-NC-ND 3.0

such as Multiple-Input-Multiple-Output (MIMO) communication, cooperative diversity and channel coding are explored to design new systems in particular hybrid RF/FSO [18].

I.2.2. UV Communications

Studies on UV communications date from the 1960s mainly for outdoor naval applications. The main advantage of UV-based systems is that they are less sensitive than IR to solar and other background interference. UV-C (200~280 nm) band is solar blind at the ground level due to ozone absorption in the upper atmosphere [15].

Recent advances in semiconductor devices for UV range (LEDs sources and avalanche photodiodes) have led to renewed interest in this technology. In particular, UV systems can operate in NLOS configurations in the presence of strong molecular and aerosol scattering (see Figure 1.4).

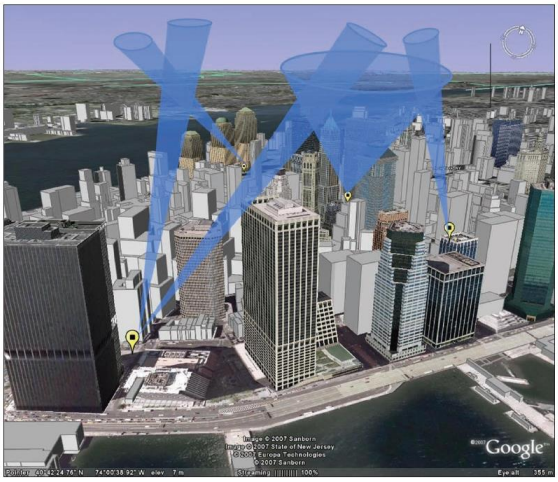

Figure 1.4. Example of NLOS UV communication, source: [15]

Because of these characteristics, they do not require pointing requirement and so offer broad coverage. Applications are now envisaged at short ranges for both civilian and military domains. However, it is still needed channel and system models suitable for practical application scenarios. In addition, to increase communication range it is necessary to develop joint modeling of turbulence and multiple scattering [16].

I.2.3. VLC

The advancements on LED technology since the 2000s has accelerated the replacement of traditional illumination devices. White LEDs have become a standard technology for indoor and outdoor lighting. Due to fast switching capabilities of LEDs much faster than the response time of the human eye, VLC has emerged and is an active research topic, based on dual use of

License CC BY-NC-ND 3.0

illumination and communication [13], [14]. This technology refers to transmissions using light spectrum over a range between 400 nm (750 THz) and 700 nm (430 THz).

Pioneer works on White LED used for illumination and communication began in the 2000s in Japan [21]. In 2003, the VLC Consortium (VLCC) was founded to promote and standardize VLC technology [22]. In addition, the IEEE 802.15.7 issued a standard for VLC in 2011 [23]. In this specification, depending on the applications and the required data rates, three physical layer (PHY) types are defined for short-range communications. PHY I is envisioned for outdoor low data rate applications. However, development of this standard has remained limited and there are now various standardization activities already under development in the VLC domain: IEEE802.11bb, IEEE802.15.7r1, IEEE802.15.13, and the ITU G.VLC.

VLC is mostly developed in indoor environments, as the dual use is not always true for the outdoor situation. For example in the middle of the day, the outdoor lighting function is not needed. Anyway, even in daylight, outdoor lightings can be exploited for communication purpose as for example traffic lights and traffic panels [24].

The most investigated outdoor VLC applications are in short and medium range for the smart city (use of street and park lights as access points [25]) and intelligent transportation systems, e.g. vehicle-to-vehicle (V2V), vehicle-to-infrastructure (V2I) [26], [27].

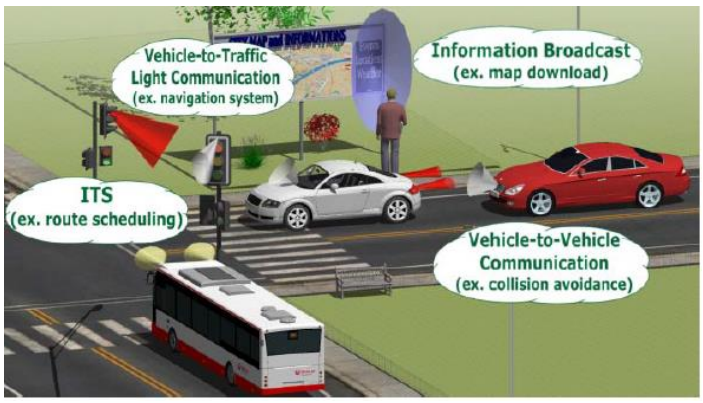

Figure 1.5. Example of outdoor VLC applications, source: [24]

Street lights can be used to communicate with cars or pedestrians. The coverage of such a system is between 50 and 100 meters. They can be used for broadband access or location. Other types of LEDs used for road signalization can communicate with cars. As these panels usually work continuously, applications are related to vehicle safety, traffic information, etc. For V2V applications, the headlights and rear lights of cars are used as VLC transmitters, reception is done by photodiode or image sensor. VLC technology may be also used to connect buildings in environments such as campuses, bank buildings and headquarters [28].

License CC BY-NC-ND 3.0

Ambient light interference due to background solar radiation and other light sources are one of the main challenges affecting VLC in the outdoor environment. In addition, propagation characteristics of VLC drastically change due to the communication environment, especially, regarding the effect of weather conditions. The received signal power fluctuates due to atmospheric obstacles such as rain or fog. Transmission range is also limited to the lighting one of the light source used and by mobility in the case of automotive applications. It is challenging to design a receiver that can provide robustness to device movements and misalignments.

Most of the VLC vehicular communication systems address these problems and present ways to mitigate the effects of ambient interference and mobility. As in the case of FSO, these issues can be overcome by employing for example hybrid VLC and RF radio links.

Another medium range application area of outdoor VLC is underwater communication that is an attractive alternative to traditional acoustic communications. The benefits are in terms of high speed, low latency, and reduced power consumption [29]. This technology uses the blue-green wavelength of the visible spectrum because it corresponds to a low attenuation window. This allows high bandwidth communication (in the MHz range) over moderate distances (10 to 100 m). The typical scenario is a point-to-point link, requiring pointing systems especially for mobile platforms.

However, the distance and range of the optical beam are affected by the type of water (from shallow water to Deep Ocean), absorption, and scattering and diffusion phenomena. In addition, fluctuations in the density, salinity, and temperature of the underwater environment lead to a phenomenon called scintillation that degrades the performance. Therefore, one of the challenges is channel modeling and characterization in order to well design underwater VLC system and apply digital communication techniques improving link reliability, throughput and/or coverage [30].

I.3. Indoor Optical Wireless Communications

I.3.1. Infrared (IR)

In indoor environments, the infrared communication technique conventionally uses wavelengths from 780 nm to 950 nm. This choice is related to the availability of low-cost optical sources and photodetectors with high sensitivity in this range. But, the eye is particularly sensitive in this region, so it is important to ensure eye-safe emission.

The first IR system was proposed by Gfeller and Bapst in 1979 and achieved 1 Mbps, based on a diffuse link operating at about 950 nm [31]. From this, the concept has been further

License CC BY-NC-ND 3.0

investigated for local area network (LAN), personal area network (PAN) and short-range applications [32], [33].

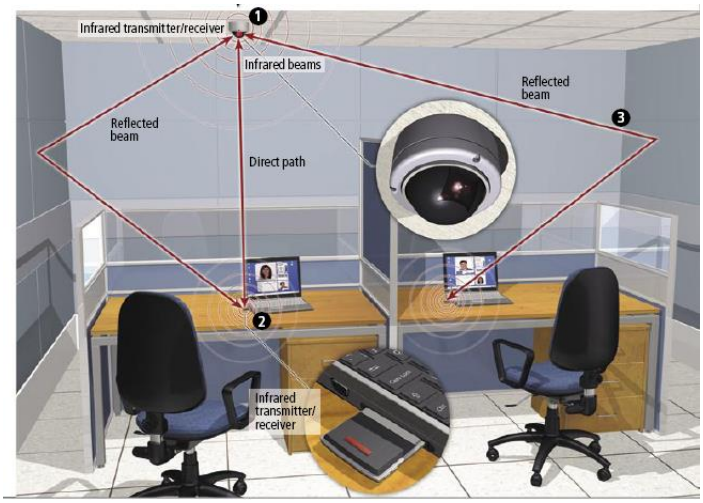

Figure 1.6. Example of indoor optical wireless network in "Broadband Room Service by Light," Scientific American Journal July 2007

One of the most successful implementations of IR technology for data communication is the Infrared Data Association (IrDA) founded in 1993 [34]. This association has produced standards focused on low-cost, short-range point-to-point links, primarily for domestic electrical equipment. Data rates increased with the development of the network and nowadays, 10Gbps communication is possible [35]. IEEE also included optical wireless standard (IR 802.11) but which has been discontinued since 1999 because of RF increased developments.

The major disadvantage of IrDA technology is the short operating distance and the need of directed LOS links with strong alignment. On the other hand, the diffuse infrared technology, exploiting the reflections in the indoor environment is more robust than LOS regarding shadowing or blockages. This allowed for terminal mobility without requiring pointing systems [31], [36]. The main drawback of diffuse transmission is the fact that the received signal is corrupted by multipath dispersion due to collected reflections at the receiver. The temporal spread of reflections results in inter-symbol interference at high data rates and limits the system bandwidth. Beside performance also depends on room properties (size, reflection coefficients of surfaces, etc.). The IrDA has defined standardization of diffuse optical wireless (OW) links at 4 Mb/s inside typical room sizes [37]. Experimentally, diffuse infrared OW links have been demonstrated at 50 Mb/s [38]. To combine the mobility of diffuse and the high-speed capability of LOS systems, approaches mainly based on beam-steering, diversity techniques and adaptive signal processing have been developed but with additional complexity [39]–[41].

License CC BY-NC-ND 3.0

IR based LAN did not achieve mass market but progress has nevertheless continued, for example, multi-gigabit indoor optical wireless networks have been recently proposed [42]. Furthermore, products are emerging based on optical wireless communications (OWC) [43], [44]. For example, this year Oledcomm [43] presented a new module, which provides high-speed internet (100Mbps in downlink and 40Mbps in uplink) through invisible light (IR).

Besides, new concepts such as Li-Fi [45] described in the following, which uses the infrared and visible light spectrum for high-speed data communication have brought growing research and new standardization activities in OWC [46].

I.3.2. Visible Light Communication (VLC)

In comparison to IR transmission, VLC does not require the installation of additional emitters as it can make use of the existing illumination installations. Deployment is thus rather easy [47]. The lighting devices are generally designed to provide uniform illumination within a room, thus performing good signal coverage [11]. Moreover, visible light sources can emit much larger intensities than IR ones, and consequently enable better performance compared to invisible IR transmitters which are subject to strict eye safety regulations. Moreover, visible light is not harmful to humans.

In addition, as illumination devices are installed almost everywhere, VLC might be applied to various short-range indoor scenarios such as homes, office rooms, conference and exhibition halls, airplanes and train cabins. Therefore, in the past decade, research works on VLC have gained high interest in many directions [27]. It is anticipated that the VLC market size reaches 75 Billion US$ by 2023 [48]. As a result, many start-ups [43], [44], [49], [50] have emerged and proposes VLC modems, illustrating the industry's interest in this technology.

Figure 1.7. Illustration of VLC luminaire [17]

One of the first applications concerns location-based services. Actually, RF global positioning systems (GPS) offers limited or no coverage in the indoor environment [51]. The

License CC BY-NC-ND 3.0

conventional methods of triangulation or trilateration associated with VLCs currently make it possible to obtain location accuracies of the order of a centimeter, whereas, for example, it is around a meter using Wi-Fi. Moreover, it is possible to easily establish signal tracking between different rooms through the continuity of installed lighting sources. However, the performance remains impacted by the fluctuations of the intensity of the light, for example in case of loss of intensity between two environments.

For navigation applications, the receiver is supposed to be mobile. It is usually a phone or a tablet worn by a user. The retail industry is particularly interested in this type of application. This allows, for example, to tell the customer where a product is and how to get there. We can mention the manufacturer Phillips who has been involved in the development of such a system in recent years. In addition, there are opportunities for robotics, which is a growing domain where communications play a critical role. As a result, applications combining positioning and mobility offer very promising prospects. However, many challenges remain, including those related to the consequences of the device mobility in a closed environment.

As said previously, from the first VLC standard approved in 2011 supporting up to 96 Mbps and currently in revision, most of the studies focus on data rate improvement. Many research works have been done to progress on this topic. For example, complex modulation such as OFDM has been proposed to overcome the challenge of inter-symbol-interference (ISI) [52], making it a suitable choice for high-speed indoor communications. Parallel communications (optical MIMO) have been also suggested to increase the data rate [53]. During the past years, data rates have been highly increased from a few Mbps to several Gbps recently [54], [55].

VLC is mainly used for point-to-point data communication. In contrast, Light Fidelity (Li-Fi) has been recently introduced to describe a complete VLC networking system supporting high-speed bi-directional multiuser communication and user mobility [56]. In Li-Fi systems, each LED lamp can be considered as a transmission point increasing the number of communication cell sites. Thanks to these ultra-small cells with radii less than 5 m, Li-Fi is now envisioned to be included in new VLC standards to complement RF standards (Wi-Fi) and to support future 5G and IoT concepts [45].

License CC BY-NC-ND 3.0

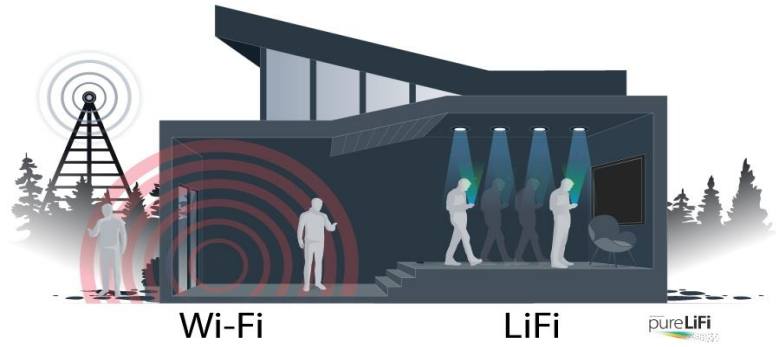

Figure 1.8. Illustration of Li-Fi concept [44]

However, several limitations of VLC technology can be identified.

Providing an efficient uplink scheme for VLC is one issue as visible uplink can be inconvenient and inefficient. Proposed solutions include RF, IR, near UV and retro-reflective transceivers [11]. But, IR seems to be the most viable solution for the VLC uplink.

The optical shot noise created by other natural and artificial light sources used in conjunction with VLC luminaires can introduce interference and saturation effects. One classical solution consists of using the blue filtering approach for phosphor-coated LED (PC-LED) VLC systems. Nevertheless, they are performing for narrow-angle operations. There are still investigations on filters suitable for wide-angle systems [57].

One of the main issues is related to mobility and shadowing. The majority of VLC studies consider only LOS links that are difficult to maintain when users are mobile. In order to integrate Li-Fi and VLC into mobile devices, such as smartphones and indeed tablets, further investigations are needed to overcome the effect of device orientation changes or body user impact [58], [59].

Indoor VLCs aim at combining lighting with communication. Therefore, an important issue is the performance of the transmission when the lights are off. One solution may be to use hybrid (RF or IR) systems. On the other hand, for VLC exclusively, some data transmissions can be realized making sure that the emitted light is sufficiently weak to be unnoticeable by the human eye. In this case, the compromise is on the transmission rates [60].

I.4. OWC applied to health monitoring

Unlike general applications, there are some areas where the benefits of OWC technology can address very specific needs where RF is not suited to provide a simple answer. This is the case, for example, in the medical domain.

There is currently a growing interest in developing smart-hospital concept allowing connectivity between all key stakeholders of the hospital, e.g., patients, health-care personnel,

License CC BY-NC-ND 3.0

equipment, data centers, other hospitals, IoT nodes, etc. [61]. Biotelemetry, in particular, is one of the key innovations of the future hospital. This includes collecting data through sensors to monitor vital signs throughout the day.

On the other hand, recent years have also been marked by growth in smartphone applications in the field of self-monitoring and self-quantification. Sensors allow users to monitor sleep, food intake, exercise, blood glucose, mood, and many other physiological states and behaviors [62].

These sensors are based on wearable technologies, such as smart watches and in most cases, wireless connected sensors are preferred for the many well-known benefits of wireless networks.

Radio-technology is the dominant approach to provide wireless connectivity. However, spectrum congestion, interference, security, privacy, and safety issues, energy efficiency, and others are still challenges of radio-based systems. As an example, the use of classical RF technologies can be limited in some environments because of potential interference [63] with sensitive devices and issues for hypersensitive persons. IEC 60601-1-2 standard [64] recommends a minimum separation distance between medical electrical equipment and RF communications gateways to avoid performance degradation.

OWC technology can be deployed as an alternative to ensure adequate performance, avoiding interference and also enhancing security and confidentiality by confining optical rays to the environment.

The use of OWC systems in the medical domain has been proposed for several years.

To replace cables between medical sensors and monitoring stations, IR links constitute a solution which is already adopted. International standards define communication services and protocols that are consistent with IrDA specifications and are optimized for portable devices in the vicinity of the patient such as bedside medical ones [65]. However, this is for static point-to-point communications.

Some works have considered IR transmissions between a mobile patient equipped with a connected sensor and an access point in the environment for both LOS and diffused systems [66]–[70]. In [66], [67], LOS configuration has been studied for a sensor on the top of the head which is quite limited regarding the practical case. It was shown that the misalignment of the transmitter and receiver can significantly increase the BER and complex tracking system was required. The diffuse scenario is investigated in [68] where the IR sensor is located at the belt

License CC BY-NC-ND 3.0

pointing toward the floor. A theoretical data rate of 1 Mbps was achieved with BER lower than 10^{-3}. The authors in [69] experimentally confirmed the potentialities of IR system based on the diffuse configuration for mobile patient monitoring. Besides, a custom-made wearable device is presented in [70], which allows OWC-based transmission of accelerometer data in the context of physical activity supervision of post-stroke patients in the hospital.

On the other hand [71], [72] have proposed multiple access schemes based on CDMA spreading codes. In [71] the access point is classically located on the ceiling whereas [72] considered that all IR nodes were on-body, exploiting only diffuse reflections over the patient environment to establish transmissions.

However, in all these works, the body carrying the sensors has not been taken into account to study IR channel behavior regarding both user movement and sensor location on the body.

With the development of new possibilities offered by visible domain, many studies also deal with the potentialities of VLC related to health monitoring [73]–[81].

The majority of works have proposed VLC uplink use to transmit health data from sensors [73], [76]–[80]. The studied configurations are generally static as in [74], [78], [79] and concern ECG and EEG data. In [76], [80] image sensor is used for the visible signal reception. The receiver is either located on the ceiling [76] or included in the smartphone [80]. In these cases, mobile monitoring is investigated but the performance is limited in terms of distance and data rates. Another limitation of VLC uplink is due to potential discomfort when a visible signal is emitted from sensors worn by a user.

VLC is more suitable for downlinks when illumination and communication are coupled. Experimental works are reported in [74], [75], [81] using visible LOS configurations to transmit health data. However VLC challenges related to mobility are not addressed.

I.5. Conclusion

In this chapter, we presented optical wireless technology according to the outdoor/indoor classification, by detailing the main advantages, challenges, and applications for infrared, UV and visible communications. One of the areas in which optical communications has a clear advantage over RF is in health-related applications. In this context, we presented a state of the art around the use of OWC for the monitoring of medical data.

In this thesis, we investigate both the use of IR and VLC technologies for sensor-based monitoring of a user moving within an indoor environment.

License CC BY-NC-ND 3.0

The studied scenario consists of using IR uplinks for transmission of health data and white light LED luminaires for VLC downlinks. To ensure IR coverage along with illumination and visible communication functions, our approach is to consider a unique lighting device including both LED and IR receivers. This is in contrast with the conventional spatial diversity method where the transceivers are distributed over the ceiling.

In this context, the data rate is not the main issue because the majority of health data from medical sensors requires a bit rate below the Mbps [82]. In contrast, the robustness of the transmission is very important for user security and this in addition to mobility constitutes the main challenge. Moreover, considering wearable devices, the impact of user body because of sensor location and energy consumption also constitute challenges.

Actually, body and movement can greatly affect both IR and visible channels. Published works have mainly addressed scenarios where optical devices are located on the upper body (e.g. ECG sensors). However, several use cases such as activity monitoring or rehabilitation applications need the sensor nodes to be positioned at the knee and/or ankle [83]. In this case, the effect of the human body on optical wireless transmission can be significant, so we need accurate and realistic models in order to explore performance.

The work presented in the thesis contributes to answering this problem by proposing an analysis of the IR channel behavior thanks to ray-tracing based simulation software named RaPSor, developed in the laboratory (A. Belhouli [84]). It allows taking into account the impacting elements that are the presence of the user body, the position of the sensor on the body, the random sensor orientation variations related to body movements. The goal is to determine the characteristics of transmitters and receivers in order to optimize performance. In addition, experiments have been performed to validate the conclusions on channel behavior.

The VLC channel has been investigated in a recent thesis (C. Le Bas [85]). We have made new simulations regarding the unique lighting device considered and concerning body impact. From analysis adapted to our context, the performance of all-optical sensor-based monitoring is explored, considering the data rate, quality of service, power.

In the next chapter, the basic technical principles of IR and VLC technologies are first introduced.

License CC BY-NC-ND 3.0

License CC BY-NC-ND 3.0

CHAPTER II. TECHNICAL CHARACTERISTICS OF INDOOR OPTICAL WIRELESS COMMUNICATION

II.1. Introduction

The aim of this chapter is to introduce fundamental technical principles and features of an indoor optical wireless communication system.

In OWC, simple low-cost intensity modulation and direct detection (IM/DD) techniques are employed, that is described in the first part. A presentation of the optical components for transceivers and building blocks related to IM/DD for both IR and visible domains is given in a second paragraph. We then describe the different optical link configurations for indoor IR and VLC scenarios. Various types of noise present in IR and VLC links are also discussed. Finally, the main digital modulation techniques used in OWC are introduced before concluding.

II.2. Intensity Modulation and Direct Detection (IM/DD)

In RF communications, baseband signals are frequency-shifted around an appropriate RF carrier, before transmission via antennas at the transmitter. The receiver generally uses one or more antennas, followed by a system comprising a local oscillator and a mixer, to return to baseband.

In optical wireless communications, the baseband electrical signal $X(t)$ is up-converted to optical carriers at the transmitter [38]. This electric-optic conversion does not rely on oscillators and mixers, but only on optical sources. After propagation over the channel, the optical signal is down-converted into baseband electric signal by a photodiode realizing the optical detection.

The simplest communication scheme, as described in Figure 2.1, is based on intensity modulation / direct detection (IM/DD). The basic principles of an IM/DD scheme are described hereafter.

At the emission, IM consists of modulating the amplitude of the electrical signal $X(t)$ according to the bits emitted from the source. The electrical signal is then transformed into a varying intensity optical power $X_i(t)$ by an incoherent optical source. The emitted signal remains always positive since the transmitted power can never physically be negative. In addition, before emission, the optical signal can be passed through an optical system for further shaping of the transmitted light beam. This can be a collimator, an optical amplifier lens, or a diffusor employed to narrow or broaden the light beam.

License CC BY-NC-ND 3.0

At the receiver side, DD consists of optical detection realized by an optical component for detection like a photodiode (PD) producing an electrical current $Y(t)$ proportional to the optical intensity. The received electric current is then amplified by the electronic circuit receiver (typically, a trans-impedance amplifier (TIA)) and digital signal processing is used for the demodulation of the information bits. In addition, before conversion, optic elements can be used, e.g. lenses and collimator to improve optical beam collection according to photo-detector's properties.

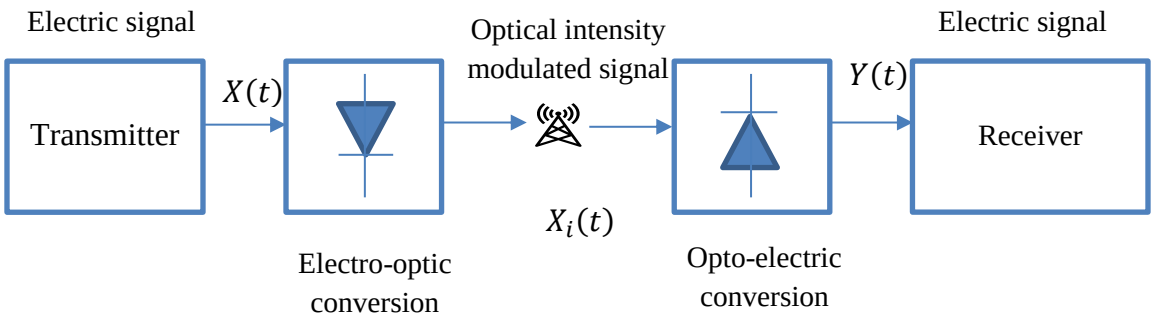

Figure 2.1. Block diagram of a typical IM/DD optical wireless system

From [38] the following relation describes a common baseband channel model for OWC:

$$Y(t) = R.X_i(t) \otimes h(t) + N(t) \qquad (2.1)$$

$h(t)$ is the OWC channel impulse response.

The symbol $\otimes$ denotes the convolution operator and the noise at the reception are supposed to be an additive white Gaussian noise (AWGN), represented by $N(t)$.

R (A/W) represents the responsivity of the photo-detector for optical power conversion into the current.

The instantaneous transmitted optical signal verifies:

$$X_i(t) \geq 0 \qquad (2.2)$$

In addition, because of eye safety requirement [86], [87], maximum optical transmitted power should not exceed a standardized limit in terms of maximum power value P_{Max}. The average optical power P_{avg} must verify:

$$P_{avg} = \lim_{T\to\infty} \frac{1}{2T} \int_{-T}^{T} X_i(t)dt \quad \leq P_{Max} \qquad (2.3)$$

In the next parts, we present the main optoelectronic components used in IR and VLC ranges and their characteristics.

License CC BY-NC-ND 3.0

II.3. Optical Components

II.3.1. Optical sources

For indoor IM/DD scenario, incoherent light sources usually accomplish the electro-optical conversion process. These are mostly LED because of easy use, low cost, and availability. Coherent light sources like laser can be employed but detection, in this case, is more complex, and performed using heterodyne or homodyne down-conversion.

In this thesis, we focus on LED for both IR and visible domains.

A LED consists of a semiconductor material doped with impurities to create a p-n junction. As in conventional diodes, current flows from the anode (p side) to the cathode (n side), but not in the opposite direction. When the diode is forward biased, electrons from the semiconductors conduction band recombine with holes from the valence band releasing sufficient energy to produce photons. The wavelength of the emitted light depends on the band gap energy of the materials forming the p-n junction.

II.3.1.1. IR LED

In 1907, the British scientist H.J. Round invented the first semiconductor light emitting diode [7]. The Russian scientist Oleg Vladimirovich Losev then developed the first LEDs but without any success for application. It was only in 1961 that two American scientists, Robert Biard and Gary Pittman, discovered and patented that Gallium Arsenide (GaAs) could emit infrared light.

Today, IR LEDs are of different materials mainly associated with GaAs. The peak wavelength depends on the semiconductor material chosen and the way it is processed. The emitted IR wavelengths are generally in 780-1000 nm optical band where there are many low cost optoelectronic components.

The principal characteristics of LEDs for communication can be listed below:

- The switching speed is expressed as rising and fall time t_{on}/t_{off}(ns) in most data sheets.
- The bandwidth *B* can be also evaluated from the rise time (when it is equal to fall time) as the time required for the signal to go from 10% to 90% of its maximum value:

$$B = \frac{\ln(9)}{2\pi t_{on}} \approx \frac{0{,}35}{t_{on}} \qquad (2.4)$$

License CC BY-NC-ND 3.0

- The peak emitter wavelength given in nm units is the wavelength at which the peak emission, or intensity, occurs. The intensity at higher or smaller wavelengths will fall off as they get farther away from the peak, depending on the directivity of the source.

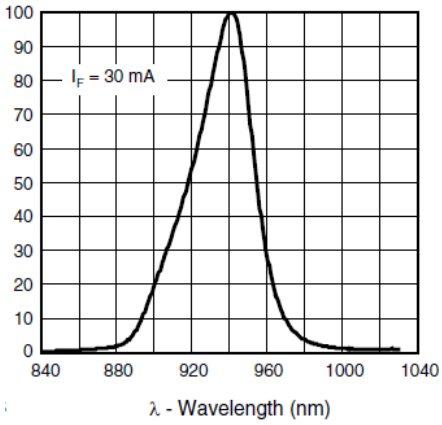

Figure 2.2. Relative radiant Power (%) vs. wavelength; LED TSAL6400 [88]

- There are three important concepts given in LED datasheets that are linked together: radiant intensity I, radiant flux Φ or power P_t, and the half-power angle $\Theta_{1/2}$.

  Radiant intensity is the power per unit solid angle, characterizing the optical property of electromagnetic radiation:

$$I = \frac{d\Phi}{d\Omega} \qquad \text{(W/sr)} \qquad (2.5)$$

  $d\Phi$ is the total radiation flux in a certain direction and $d\Omega$ is the corresponding solid angle in the steradian unit.

  Let us define the solid angle in the steradian unit.

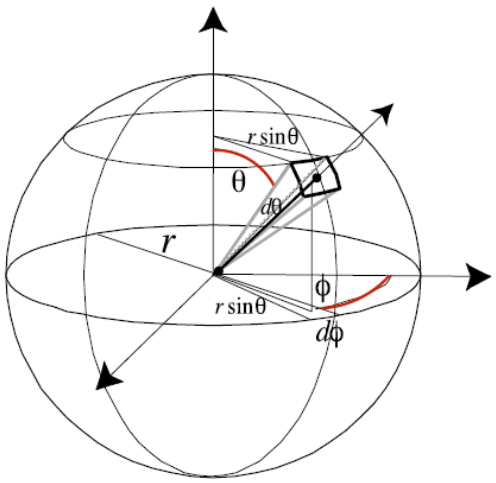

Figure 2.3. Illustration of differential solid angle

License CC BY-NC-ND 3.0

From Figure 2.3, the differential solid angle is expressed as:

$$d\Omega = sin\theta d\theta d\varphi \qquad (2.6)$$

So, the solid angle for the sphere is $\Omega = \int_0^{2\pi} \int_0^{\pi} sin\theta d\theta d\varphi = 4\pi$ (sr)

However, LEDs considered as point sources are not isotropic sources. Their main structures are planar and LEDs emit light from all surfaces. The radiated light is thus concentrated in a given beam. Generalized Lambertian law [31] classically models the angular distribution of radiant intensity of a LED:

$$I(\theta) = I_0 cos^m(\theta) \qquad (2.7)$$

$I_0 = I(\theta = 0°)$ is the maximal axial intensity (provided in data sheets generally in mW/sr):

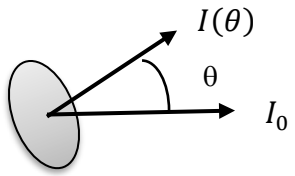

Figure 2.4. Central intensity I_0 and intensity $I(\theta)$

The parameter *m* in (2.7) is a measure of the LED directivity (m>0). It is related to the angle corresponding to the half of maximal intensity $(I_0/2)$ namely the half-power angle $\theta_{1/2}$:

$$m = -\frac{\ln(2)}{\ln(cos\theta_{1/2})} \qquad (2.8)$$

The LED is even more directional as *m* is high, that is the half-power angle $\theta_{1/2}$ is small and vice versa. Figure 2.5 shows an example of the Generalized Lambertian pattern of a point source with *m*=3.

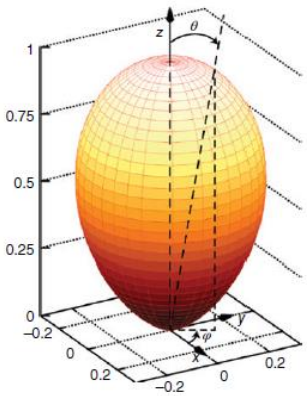

Figure 2.5. Generalized Lambertian pattern of a point source with *m*=3 [89]

License CC BY-NC-ND 3.0

A Lambertian source exhibits a trade-off between intensity and directivity. This is illustrated in Figure 2.6, for a normalized radiant intensity to 1W/sr and different m orders.

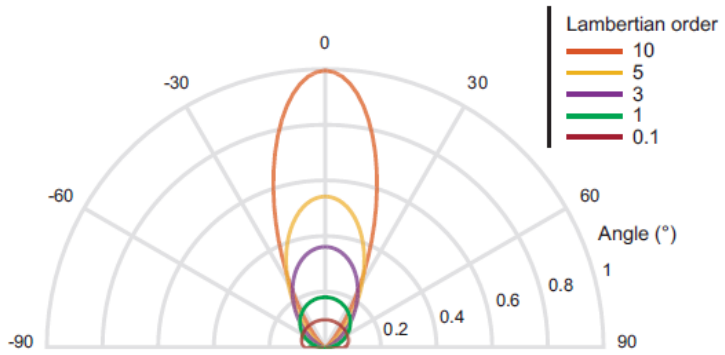

Figure 2.6. Normalized intensity vs Lambertian order m

From (2.5) and using (2.6) and (2.7), we can express the radiant flux or radiated power as:

$$\Phi = P_t = \int_0^{\Omega_{MAX}} I(\theta) d\Omega = \int_0^{\theta_{MAX}} 2\pi\, I_0 cos^m(\theta) sin\theta d\theta \qquad (2.9)$$

The value $\theta_{MAX} = \frac{\pi}{2}$, for all m.

Considering $u = cos\theta$, equation (2.9) leads to:

$$P_t = 2\pi I_0 \int_0^1 u^m\, du = \frac{2\pi}{(m+1)} I_0 \qquad \text{(W)} \qquad (2.10)$$

We note that a higher m implies higher I_0 for a given radiated power.

In addition, like conventional diodes, LED is a current-dependent device with its forward voltage drop V_F, depending on the semiconductor and on the forward biased current I_F. The amount of light generated varies proportionally with current I_F (see example in Figure 2.7):

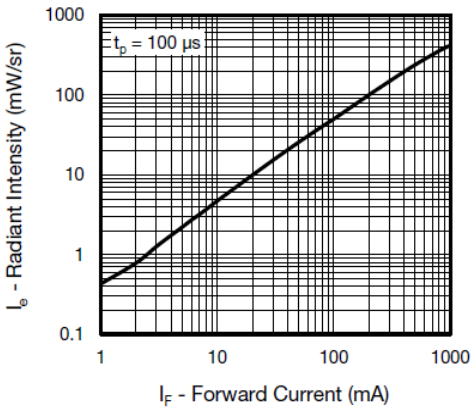

Figure 2.7. Radiant Intensity vs. Forward Current of LED TSAL6400 [31]

License CC BY-NC-ND 3.0

However, this behavior can also be non-linear because it is limited by turn-on voltage and saturation level.

- Datasheets provide another characteristic, the irradiance, which is the flux per unit area.

This also indicates the intensity emerging in front of the LED but in the projected area of solid angle, depending on the square of distance from the point source. The unit of irradiance is W/m². To convert *sr* to m², the distance *r* must be known.

The number of steradians in a given solid angle **Ω** can be determined by dividing the area *A* on the surface of the sphere lying within the intersection of the solid angle by the square of the radius of the sphere *r* ($\Omega = \frac{A}{r^2}$), as indicated in Figure 2.8.

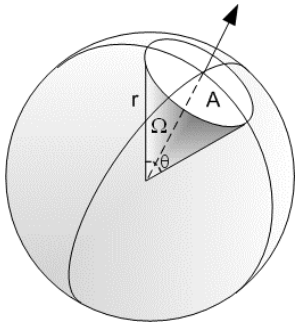

Figure 2.8. Illustration of surface swept out by a solid angle Ω

Considering the Lambertian pattern and from (2.6), the area *A* of the sphere lying within the intersection of the solid angle corresponding to half-power angle $\theta_{\frac{1}{2}}$ can be expressed as:

$$A = 2\pi r^2(1 - \cos\left(\theta_{\frac{1}{2}}\right)) \qquad (2.11)$$

As an example, for $\theta_{\frac{1}{2}} = 60°$, equation (2.11) indicates that, at a distance r=1m, the corresponding area is of 3.14 m². Consequently, if the radiant intensity is 10 mW/sr, this corresponds to an irradiance of about 3.18mW/m² or 31.8µW/cm².

For a higher directivity as $\theta_{\frac{1}{2}} = 15°$, at a distance r=1m, the corresponding area is of 0.214m². For the same radiant intensity, this leads to an irradiance of 46.72mW/m².

Finally, another quantity is also defined which is the radiant intensity per unit of projected area in the observation direction, called radiance in ($W.m^{-2}.sr^{-1}$) units. Radiance is independent of the distance.

License CC BY-NC-ND 3.0

$$\text{Radiance= Irradiance}/2\pi\left(1-\cos\left(\theta_{\frac{1}{2}}\right)\right) \qquad (2.12)$$

For ideal Lambertian LED (m=1, $\theta_{\frac{1}{2}} = 60°$), an irradiance of π W/cm² corresponds to a radiance of 1 $W.cm^{-2}.sr^{-1}$.

II.3.1.2. VLC LED

The first commercial visible LED (red) has been demonstrated in 1962 [8]. The efficiency was very small and the first use was mainly indicators for electronic devices. The efficiency improvement has been huge over the years so that it is now at a level that is competing with conventional lighting sources. Today, high-power LEDs have replaced conventional incandescent or fluorescent light sources in indoor environments. LEDs possess many advantages over conventional light sources, including efficiency, light/power density, reliability, and form factor.

The primary function is thus providing illumination. Consequently, the LED has to emit white light, which covers the whole visible light spectrum from 375 to 780 nm.

a) Types of White LEDs

It is the invention of the blue LEDs in the 2000s [47], which allowed the development of white light devices used also for communication. There are two main types of white LEDs.

In the first technique, the three primary colors (Red, Green and Blue) are mixed to produce white light. This type is named RGB LED [90].

These three primary colors can also produce other renderings, adjusting each color independently. An example of an emission spectrum is shown in Figure 2.9:

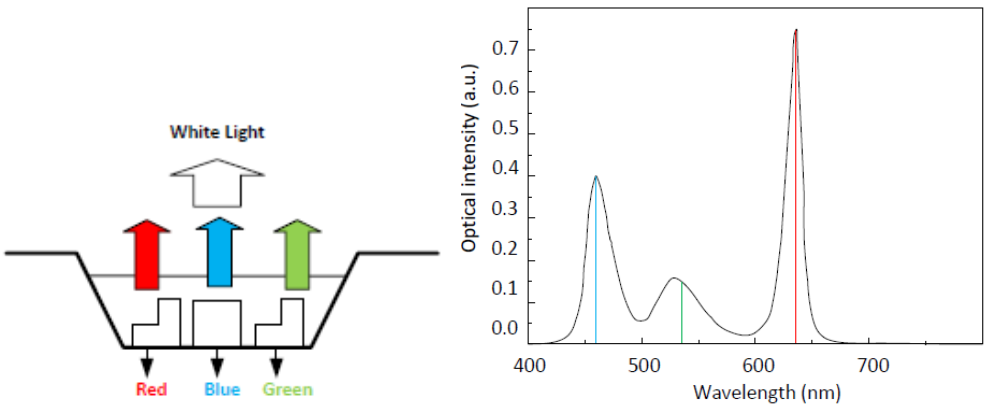

Figure 2.9. Trichromatic white LED with associated emission spectrum [91]

License CC BY-NC-ND 3.0

The other approach uses a phosphor material illuminated by blue light (Figure 2.10). Part of the blue light is then converted to yellow. The remaining blue light, when mixed with the yellow light, produces a white light [92]. This is the most common type of LED, called Phosphor-Converted (PC) LED.

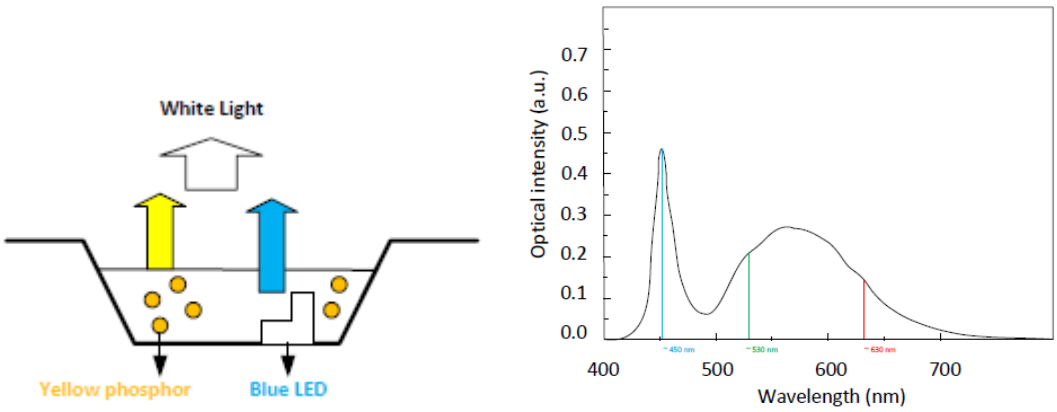

Figure 2.10. PC white LED with associated emission spectrum [91]

R-G-B LED has relative high modulation bandwidth (20MHz) and can support wavelength division multiplexing (WDM), but the cost is relatively high. Commercial PC LEDs are cheaper but have limited bandwidth, which is typically (2-3) MHz. This is due to the slow response time of phosphor. However, the bandwidth can be increased to about 20 MHz by using a blue filter [11].

Recently, Organic LEDs (OLED) have been developed for lighting and displays. OLED is made from carbon-based organic materials that emit light when electricity is applied. These devices can also be adapted for lighting and data communication [93]. However, they offer much lower bandwidth than inorganic LEDs.

In this thesis, we will suppose that the communicating luminaire is constituted of PC LEDs.

b) Photometric parameters

For communication purpose, the main characteristics of a visible LED are the same as for IR: radiant flux or power (W), radiant intensity (W/sr), irradiance (W/m^2), radiance ($W.m^{-2}.sr^{-1}$). These parameters called radiometric quantities are related to the physical properties of the optical wave but do not take into account the specific sensitivity of the human eye when considering illumination.

License CC BY-NC-ND 3.0

On the other hand, photometry involves quantities that are visible to the human eye. Thus, the corresponding parameters are: luminous flux (Lumen lm), luminous intensity (candela (cd) or lm/sr), illuminance (l/m² or lux) and luminance (lm/m²sr or cd/m²; generally used to measure brightness). Also, visible sources are characterized by the efficacy in lm/W traducing the performance of the source for illumination.

The human eye sensitivity has been standardized by the CIE (International Commission on Illumination) [94]. The curves of eye sensitivity function $V(\lambda)$ and luminous efficiency for photopic vision are shown in Figure 2.11.

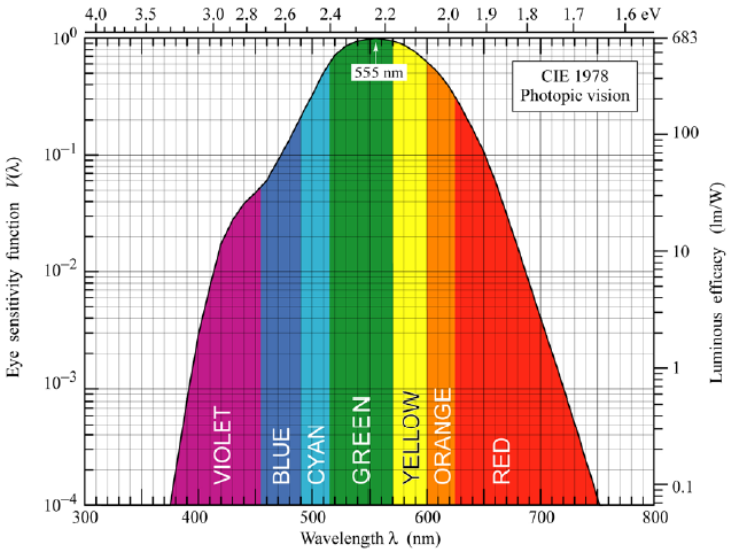

Figure 2.11. Eye sensitivity function and luminous efficacy for photonic vision [95]

The photonic eye sensitivity function $V(\lambda)$ has maximum sensitivity in the green spectral range at 555 nm for which its value is normalized to 1.

The maximum luminous efficacy is obtained for a monochromatic source at 555 nm and is equal to 683 lm/W. For this wavelength, 1W is equivalent to 683 lumens. The relationship between radiant flux (W) and luminous flux (lm) is expressed as:

Luminous flux (lm) = Radiant flux (W) x 683 x $V(\lambda)$ (2.12)

A white LED has a distributed power spectrum $\Phi(\lambda)$ over the visible range (see Figures 2.9 and 2.10). In this case, the radiant flux respectively the luminous flux are given by:

$$\Phi_r = \int_{380nm}^{780nm} \Phi(\lambda) d\lambda \qquad (2.13)$$

$$\Phi_L = 683 \int_{380nm}^{780nm} \Phi(\lambda) V(\lambda) d\lambda \qquad (2.14)$$

Note that with the same approach, the illuminance for a given irradiance is:

License CC BY-NC-ND 3.0

Illuminance (lux) = Irradiance (W/m²) x 683 x $V(\lambda)$ (2.15)

Thus, the irradiance required to produce an illuminance of 1 lux at 555nm is around 1.464 mW/m^2.

As an example, typical indoor light fixtures provide illumination levels of more than 400 lux in office room [85] that is an irradiance around 0.6 W/m².

II.3.1.3. Safety considerations

Different parts of the human eye are susceptible to damage at a given wavelength. Therefore, this can be an issue for optical system design.

The cornea and lens focus the light on the retina at the visible and near IR (up to 1400 nm). This is the retinal thermal hazard. The eye protects itself from visible light by closing the iris down, but not from near-IR. So, IR radiation is particularly dangerous.

In addition, visible light (380 nm to 780 nm) can damage the eye by photochemical effects (blue light hazard). The effects of light penetration according to wavelength are illustrated in Figure 2.12.

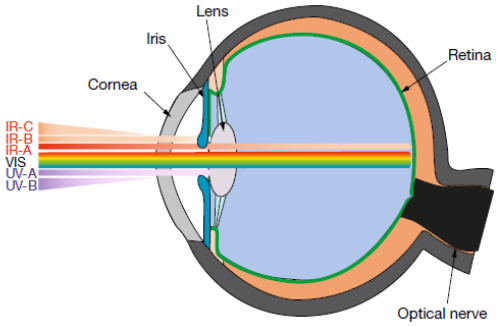

Figure 2.12. Penetration of optical radiation into the eye [96]

Human skin can also be very damaged (burn risks). However, the skin is much less sensitive than the eye. Therefore, if a system is eye safe it will also be safe for human body skin.

Before 2008, most LEDs were labeled in accordance with the IEC/EN 60825 laser safety standard [86]. However, this standard was not considered appropriate for most LEDs designed to be non-coherent light sources. Further, the IEC/EN 60825 standard does not define risk groups for LED luminaires. As a result, a newer standard, IEC 62471-2006 [87] was adopted for lamps and conventional LEDs. Note that this is ANSI/IESNA RP-27 [97] for the USA.

License CC BY-NC-ND 3.0

The different biologic effects taken into consideration by the standards are summarized in Figure 2.13.

Bioeffect				
Hazard	Wavelength Range (nm)	Quantity	Eye	Skin
Actinic UV skin and eye	200-400 (weighted)	Irradiance	*Cornea* – photokeratitis *Conjunctiva* – conjunctivitis *Lens* – cataractogenesis	Erythema Elastosis
UVA eye	315-400	Irradiance	*Lens* – cataractogenesis	—
Retinal blue light	300-700 (weighted)	Radiance	*Retina* – photoretinitis	—
Reginal blue light small source	300-700 (weighted)	Irradiance	*Retina* – photoretinitis	—
Retinal thermal	380-1400 (weighted)	Radiance	*Retina* – retinal burn	—
Retinal thermal-weak visual stimulus	780-1400 (weighted)	Radiance	*Retina* – retinal burn	—
Infrared radiation eye	780-3000	Irradiance	*Cornea* – corneal burn *Lens* – cataractogenesis	—
Thermal skin	380-3000	Irradiance	—	Skin burn

Figure 2.13. Biological hazards considered with the standard IEC/EN 62471 [87]

The standard defines four different Risk Groups (RG) for LEDs as well as lamps (see Figure 2.14)

Risk Group	Philosophical Basis
Exempt	No photobiological hazard
GROUP 1 (Low Risk)	No photobiological hazard under normal behavioral limitations
GROUP 2 (Moderate Risk)	Does not pose a hazard due to aversion response to bright light or thermal discomfort
GROUP 3 (High Risk)	Hazardous even for momentary exposure

Figure 2.14. Risk Groups of the standard IEC/EN 62471 [87]

Two key radiometric parameters are used to assess the level of harmful radiation: irradiance and radiance. Irradiance evaluates the risk of hazards to the skin and to the front of the eye. Radiance evaluates the risk of hazards to the retina of the eye. Another significant factor is the exposure period varying for each group: the higher the RG, the shorter the time basis to be applied.

For example, the IEC-62471 standard for IR-A (near IR) between 760 and 1400 nm radiation imposes:

- Infrared radiation hazard exposure limits for the eye cornea: the maximal irradiance is 100W/m² within 1000s. This limit is imposed at 0.2m and so corresponds to the maximal radiant intensity of 4W/sr. Commercial IR LEDs generally respect this limitation.

License CC BY-NC-ND 3.0

- The thermal hazard exposure limit for skin: the maximum irradiance limit is slightly higher than for the cornea. Therefore, the cornea limit can be taken for worst-case considerations.

- Retinal thermal hazard exposure limit: for Risk Group 0 which is the most constrained, the radiance $\leq 6000/\alpha$ ($W.m^{-2}.sr^{-1}$) within 1000s with a distance d=0.2 m; α is the angular subtended of the light source (between 0.011rad and 0.1rad).

II.3.2. Optical receivers

The most classical device used to detect light and convert it into an electric signal is a photodiode.

This is a semiconductor with p-n junction as LED. When a reverse voltage is applied (photoconductive mode), photons are absorbed, resulting in free carriers that become current through the junction. This current is quite linearly proportional to the intensity of light that radiates on the active detection area.

Note that the photodetector area is much longer than the optical wavelength (IR and visible) so the multipath fading can be averaged that is an advantage of optical systems compared to RF.

The two popular photodiodes are positive-intrinsic-negative (PIN) and avalanche (APD) [98]. Compared to PIN, the ADP provides an inherent gain in current through a repeated electronic ionization process resulting in increased sensitivity but with additional noise due to the multiplication process. Semiconductor material determines the operation wavelength range. For example, the silicon PIN and APD have operating wavelength between 300 and 1100 nm including both visible and IR domains.

The most important properties are [10]:

- The responsivity R (A/W), related to the quantum efficiency, is dependent on the wavelength and on the semi-conductor material. This is the ratio of the incident power to the output current. The responsivity of a PIN photodetector is always less than unity whereas it is much higher for APD but the compromise is multiplication of noise.
- The physical active area A_r is the light-sensitive area. Increasing the area increases the amount of collected power so the current. However, this can lead to the high capacitance that limits the bandwidth. In addition, a large area can also collect more ambient light contributing to the noise.

License CC BY-NC-ND 3.0

- The Field-Of-View (FOV) corresponds to the direction exposed to 50% of the maximum received intensity (Figure 2.15). Thus, the value of the effective surface collection of the receiver is given by:

$$A_{eff} = \begin{cases} A_r cos\psi & 0 \le \psi \le FOV \\ 0 & \psi > FOV \end{cases} \quad (2.16)$$

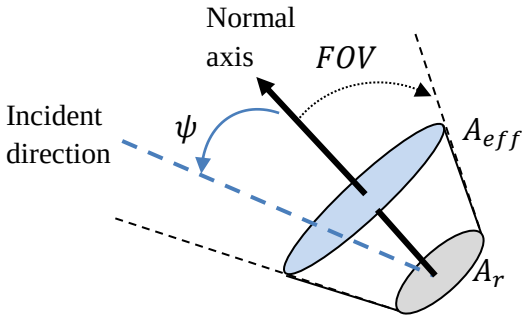

Figure 2.15. Illustration of FOV receiver

One suitable method to improve the collected incident radiation amount for a small area photodiode is to use optical concentrators. The most classical device is the hemispherical lens, which is non-imaging concentrator [99], [100]. For an ideal concentrator with an index of refraction *n*, this increases the effective area as:

$$A_{eff} = \begin{cases} g(\psi) A_r cos\psi & 0 \le \psi \le FOV \\ 0 & \psi > FOV \end{cases} \quad (2.17)$$

$$\text{With } g(\psi) = \begin{cases} \frac{n^2}{sin^2(FOV)} & 0 \le \psi \le FOV \\ 0 & \psi > FOV \end{cases} \quad (2.18)$$

We can see from (2.18) that the concentrator gain increases as the FOV diminishes, reducing the system coverage. So, there is a compromise.

An optical filter can be also associated with the concentrator, in order to reject undesirable wavelength and ambient light [36]. Therefore, the filter transfer function $T(\psi)$ depending on the incidence angle has also to be considered in (2.17).

In the thesis, we do not take into account optic elements and so we set $g(\psi)$ and $T(\psi)$ to unity whatever the incidence angle.

License CC BY-NC-ND 3.0

- The dark current *Id* present in the absence of light imposes limitation for low levels because a received signal must produce more current than the dark current in order to be detected. It is also a source of noise for the communication system. Therefore, the dark current must be minimized to maximize the sensitivity of the device.
- Junction capacitance is an important parameter of a photodiode as this can have an impact on the bandwidth. Using photodiode in reverse bias mode reduces the junction capacitance and increases the response speed.
- The bandwidth, related to the rise and fall time can be influenced by the capacitance introduced by the detection area. As for LED, if the rise and fall times are equal, the 3-dB bandwidth can be estimated from (2.4).

After the photodiode, it is needed to convert the current into a voltage. Front-end circuits as trans-impedance amplifiers (TIA) achieve this operation. A basic TIA structure is shown in Figure 2.16 where the output voltage is simply obtained from the detected current.

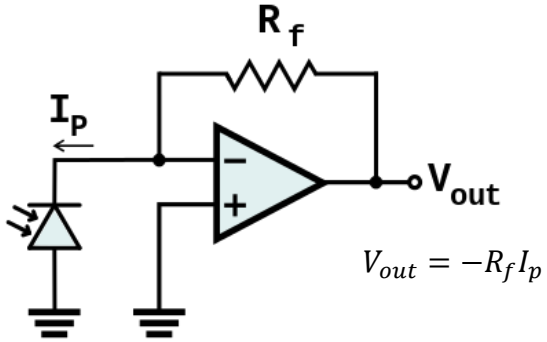

Figure 2.16. Basic scheme of TIA

The TIA design is generally challenging to meet the requirements in both gain and bandwidth. This is discussed in [14] for more details.

Others devices can also be used instead of photodiodes, especially in visible domain. Image sensors included in phone devices today are the basic receivers for optical camera communications [101]. The performance limitation, in this case, is linked to the frame rate of image sensors. Besides, there is a growing interest in organic solar cells constituting a power source and allowing data collection [102]. This can increase the potentialities of wearable devices, but this is not yet mature for commercial products.

In the thesis, we focus on classical photodiodes for both IR and visible links.

License CC BY-NC-ND 3.0

II.4. Optical propagation

II.4.1. Types of OWC links

Based on the light propagation path radiated by LED and detected by the photodiode, the different link configurations are generally classified, relying on the existence of Line of Sight (LOS) and the degree of directivity of the source and receiver (directed, hybrid and non-directed) [36]. In the directed link, both transmitter and receiver have narrow angles. On the other hand, in non-directed links, both the transmitter and receiver have wide angles. Hybrid link is the combination of the directed link and non-directed link where transmitters and receivers have different directivity.

If the LOS path is present in directed configuration then this link topology is defined as directed-LOS illustrated Figure 2.17 (a). Directed LOS is the best option for very high speed and low error rate communications. However, this type of link is likely to be blocked, especially in indoor and therefore not suitable for mobile communication scenarios.

At the opposite, when there is no LOS path in non-directed configuration the propagation is diffuse. The link is established by the collection of reflective beams over the environment (Figure 2.17 (c)). A diffuse link offers greater robustness compared to mobility but at the expense of lower performance compared to the LOS link.

Hybrid links are useful when a system requires a trade-off between transmission rate and mobility.

Figure 2.17(b) presents a non-directed LOS link, which is the one investigated in the thesis as we consider a connected luminaire installed on the room ceiling and a user carrying optical transceivers. In this case, in addition to the LOS link, there are also signal reflections from the walls and objects of the room that is non-LOS (NLOS) links.

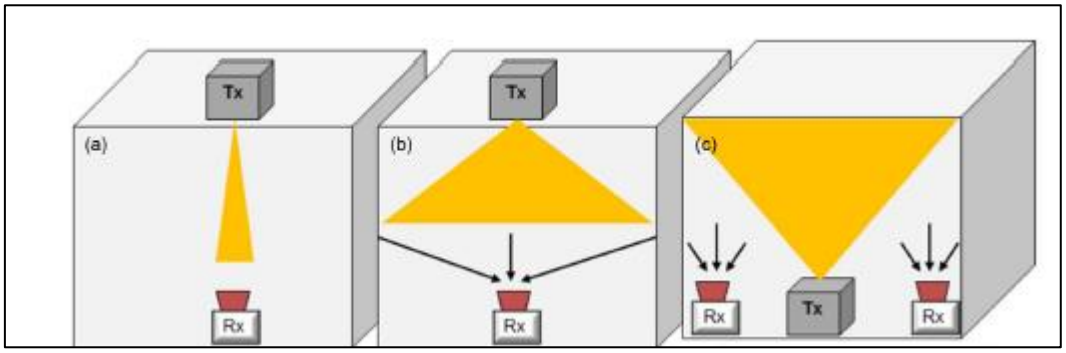

Figure 2.17. OWC link configurations: (a) directed LOS (b) non-directed LOS (c) diffuse [16]

License CC BY-NC-ND 3.0

To characterize the link, the parameters that are classically obtained from the impulse response of the link $h(t)$ are DC gain H_0, root mean square (RMS) delay spread τ_{RMS} and mean excess delay τ_0 [10].

They are defined as the following:

$$H_0 = H(0) = \int_{-\infty}^{+\infty} h(t)dt \qquad (2.19)$$

$$\tau_{RMS} = \sqrt{\frac{\int_0^{+\infty}(t-\tau_0)^2 h^2(t)dt}{\int_0^{+\infty} h^2(t)dt}} \qquad (2.20)$$

$$\text{With } \tau_0 = \frac{\int_0^{+\infty} t h^2(t)dt}{\int_0^{+\infty} h^2(t)dt} \qquad (2.21)$$

To avoid multipath dispersion, the delay spread should be significantly shorter than the symbol period.

The contributions related to LOS and reflections arriving at the receiver are described in the next paragraphs.

II.4.2. LOS links

The geometry of the LOS link is presented in Figure 2.18, where *d* is the distance between the optical transmitter with a half-power angle $\varphi_{1/2}$ and receiver characterized by FOV.

In LOS links, the impulse response is a Dirac-like signal expressed as:

$$h_{LOS}(t) = \begin{cases} H_{0LOS}\delta\left(t - \frac{d}{c}\right) & 0 \leq \psi \leq FOV \\ 0 & \psi > FOV \end{cases} \qquad (2.22)$$

License CC BY-NC-ND 3.0

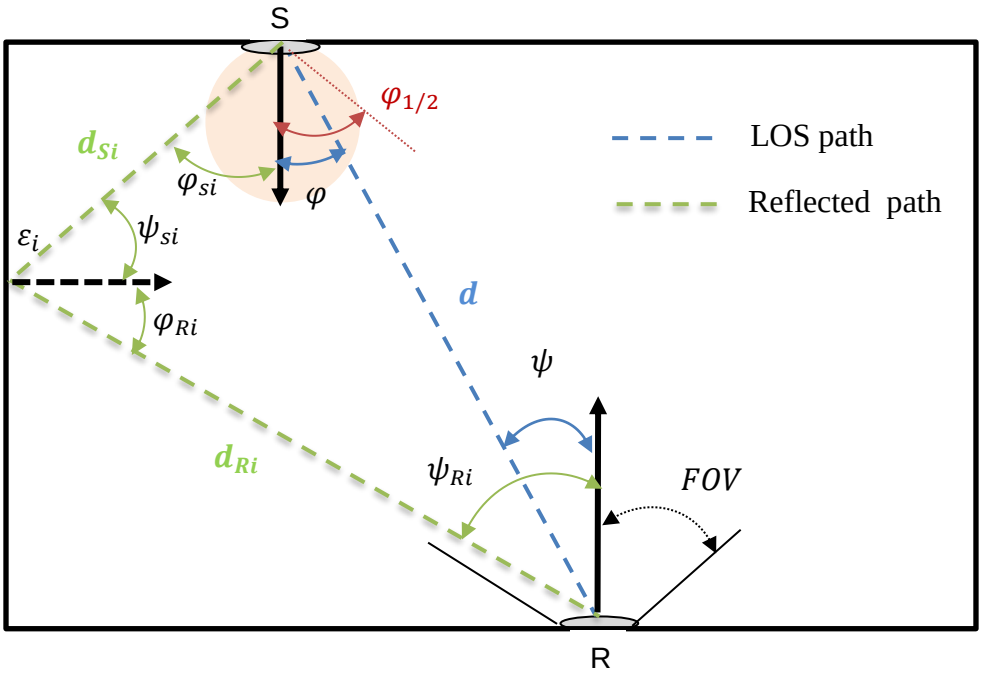

Figure 2.18. LOS link and reflected path geometry

with c is the speed of light, $\delta(.)$ is Dirac function. $\frac{d}{c}$ represents the delay of propagation

H_{0LOS} is DC gain, the most important features of LOS link as it represents the ratio between the received power P_r and the emitted one P_t:

$$H_{0LOS} = \frac{P_r}{P_t} = \begin{cases} \frac{A_r(m+1)}{2\pi d^2} cos^m(\varphi)\cos(\psi) & 0 \le \psi \le FOV \\ 0 & \psi > FOV \end{cases} \quad (2.23)$$

II.4.3. NLOS link

The diffuse part of the impulse response is given as an infinite sum of multipath components propagating within a room. It is a function of the room geometry, the spectral reflectance of surfaces and obstructing objects. The reflected paths arrive at the photo-receiver at a slightly delayed time compared to the LOS component while further attenuated. This attenuation depends on the transmission wavelength, the surface materials and angle of incidence.

Figure (2.18) illustrates a first-order reflective path associated with an elementary area ΔA of room surface element ε_i. This surface element can be seen like a detector and an emitter that re-transmits the incident signal as a point source taking into account ρ_i that is the reflection

License CC BY-NC-ND 3.0

coefficient. Typically, the reflecting surfaces are assumed to be ideal Lambertian that is with m=1.

As an example, the impulse response of all contributions from the first reflection over all elements ε_i in Figure 2.18 is:

$$h_{0NLOS}^{(1)}(t,S,R) = \begin{cases} \sum_{\varepsilon_i} \frac{\Delta A \rho_i (m+1)}{2\pi^2 d_{Si}^2 d_{Ri}^2} cos^m(\varphi) \cos(\varphi_i) \cos(\psi_i) \cos(\psi) \delta(t - \frac{d_{Si}+d_{Ri}}{c}) & 0 \leq \psi \leq FOV \\ 0 & \psi > FOV \end{cases} \quad (2.24)$$

The impulse response considering that signals from transmitter S experience k reflections before arriving at receiver R is:

$$h_{NLOS}(t,S,R) = \sum_{k=0}^{\infty} h_{NLOS}^{(k)}(t,S,R) \quad (2.25)$$

Channel impulse response with k reflections $h_{NLOS}^{(k)}(t,S,R)$ can be calculated by the responses of (k-1) reflections. This iterative approach has been first developed in [33] for first-order reflections. A more accurate impulse response analysis was presented in [103] by considering higher order of reflections. However, for high-order reflections and complex scenes with various objects, a recursive method is expensive in terms of system memory requirements and computation time. Note that it has been shown by several works that the number of reflections can be limited to 3 without a high loss of accuracy.

To simplify, closed form expression can be used but for particular scenarios in an empty room as the well-known ceiling-bounce model [104].

Approaches based on Ray-Tracing first proposed in [105] associated with Monte-Carlo method allow the evaluation of impulse response in the case of complex scenes even considering a large number of reflections. It consists in launching a given number of rays in random directions over the scene, based on a given statistical distribution. Each ray is tracked until it reaches the detector. An advantage is that it is not necessary with this method to assume a Lambertian reflection for the surface elements. This is today the most reliable modeling approach for indoor OWC channel.

We will use this approach in the thesis for both IR and visible channel modeling, thanks to a software tool developed in the laboratory named RaPSor [84]. It offers the use of two simulation algorithms: Ray-Shooting (RS) and Ray-Gathering (RG). They are each based on formulations resolved by the method of MC and incorporate optimization techniques to reduce computing time. In the case of the RS method, the rays are launched from the transmitter while the RG method consists in generating rays from the receiver. [84], [106] showed that the two

License CC BY-NC-ND 3.0

methods RG and RS gave the same results. However, the RG algorithm has much lower computation times because it requires a smaller number of rays to converge.

An important parameter in the modeling is the reflectivity of surface materials within the indoor environment. Reflectance values for some typical materials are presented in Figure 2.19 for both studied domains IR and visible [107], [108].

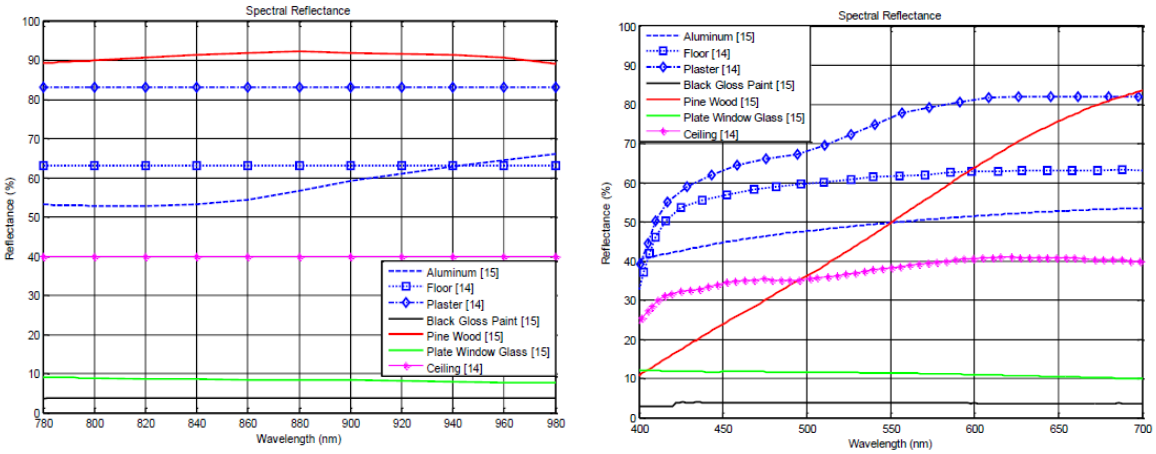

(a) (b)

Figure 2.19. Material reflectivity for (a) IR and (b) visible domains [85]

As observed, the reflectance of most materials can be assumed to be a constant in IR band for most practical purposes while the wavelength dependency needs to be taken into account for the visible band.

II.5. Noise

Both the channel and the receiver mainly introduce the noise that limits the communication system performance. Therefore, the noise sources include ambient light noise, photodetector induced noise and electronics noise.

II.5.1. Ambient light noise

The ambient light contains visible and IR radiation from various natural and artificial sources, such as the background sunlight through windows, emitted light from incandescent, and fluorescent lamps or other IR devices present in the environment [109], [110].

License CC BY-NC-ND 3.0

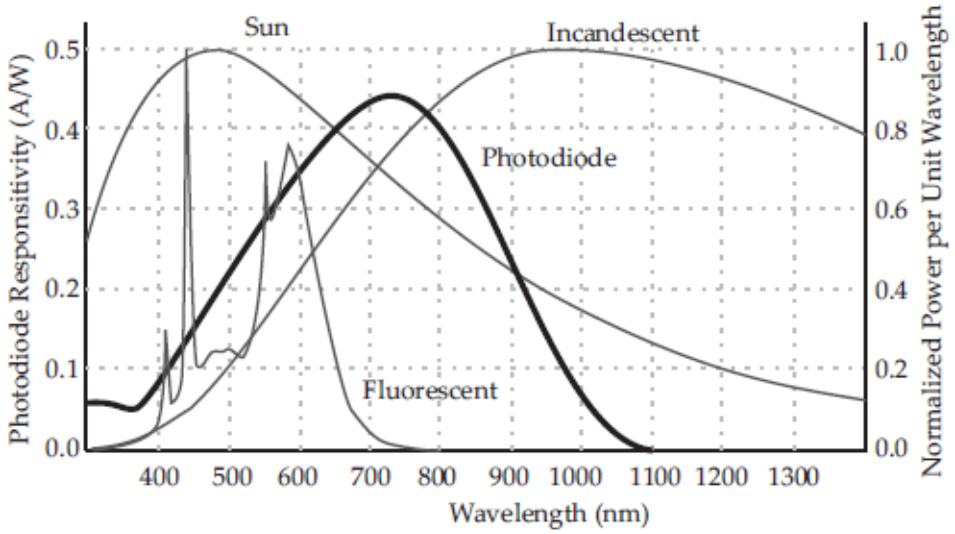

Figure 2.20. Spectral ambient light source impact on photodiode [111]

The ambient lighting induces a DC current I_B on the photo-detector called background current. Even when optical filtering is used to reject some of the ambient light [112], this resulting current gives rise to shot noise. Shot noise can be modeled as zero-mean additive white Gaussian noise (AWGN) which is independent of the signal. Considering PIN photodiode, the noise power can be expressed as [10]:

$$\sigma^2_{shot-ambient} = 2qI_B B \qquad (2.26)$$

Where q the electron charge, and B is is the bandwidth related to the data rate.

VLC and IR systems are both impacted but the effects are more severe in VLC since it shares the same spectrum as lighting sources such as LED or sunlight (see Figure 2.20). Values of I_B are reported from measurements in [110] for several typical ambient light conditions. The highest value of I_B is around 5100µA corresponding to direct sunlight without the optical filter.

In the thesis, because VLC is more impacted than IR we will consider two different values of background current according wavelength ranges: $I_{BIR} = 200\mu A$ and $I_{BVLC} = 5100\mu A$.

II.5.2. Photo-detector noise

The ability of a photo-detector to detect incident signal is limited by shot noise resulting from the statistical nature of the photon-to-electron conversion process. This type of noise is named quantum noise. For an APD, in addition to this primary source of shot noise, there is an excess noise generated by the random avalanche process.

License CC BY-NC-ND 3.0

Another type of noise involved in the detection of optical radiation is dark current noise which is the current present even if there is no incident optical radiation on the photo-detector.

For indoor communications, it is classically assumed that the ambient light effects high-intensity shot noise, which is dominant compared to the photo-detection induced noises [10].

II.5.3. Receiver thermal noise

The noise at the receiver is independent of the received signal intensity and is usually induced by the front-end electronics [113]. The most typical front-end associated with photodiode is a trans-impedance amplifier TIA as illustrated in Figure 2.16 constituted by an operational amplifier and feedback resistance R_f [114].

This thermal noise is considered as a zero-mean additive Gaussian random process. The noise variance is mainly related to the feedback resistance expressed as:

$$\sigma_{thermal}^2 = \frac{4K_bT}{R_f}B \qquad (2.27)$$

where $K_b = 1{,}381.10^{-23}JK^{-1}$ is the Boltzmann constant, T (°K) is the ambient room temperature, B is the bandwidth.

The noise N (t) in equation (2.1) is assumed to be the sum of thermal noise and shot noise due to intense ambient light. Consequently, it can be modeled as AWGN with zero mean and variance:

$$\sigma^2 = \sigma_{shot-ambient}^2 + \sigma_{thermal}^2 \qquad (2.28)$$

In the following, we suppose that $\sigma_{shot-ambient}^2 \gg \sigma_{thermal}^2$.

II.6. Digital modulation techniques

In OWC, information is carried by the intensity (power) of the light in infrared as in visible. As a result, the information-carrying signal has to be real valued and strictly positive. Consequently, RF modulation/demodulation techniques cannot be directly applied to OWC schemes. In addition, for VLC, other issues related to illumination function such as dimming support and flickering have to be taken into account when designing modulation schemes.

There is a number of methods, which can be used to modulate the data over the optical spectrum.

For IR and VLC we can distinguish single-carrier and multicarrier modulations, which are briefly presented in the following.

License CC BY-NC-ND 3.0

In the visible range, there is another specific modulation which is Color-Shift Keying (CSK). CSK modulates the signal using the intensity of the three colors of RGB LEDs as defined in IEEE802.15.7 standard [23].

II.6.1. Single-carrier modulations

Single carrier modulation schemes can be adapted to OWC from RF without major modification.

The most common schemes include On-Off keying (OOK), pulse position modulation (PPM), pulse width modulation (PWM) and unipolar pulse amplitude modulation (PAM) [10].

- OOK is the simplest optical modulation technique. It is a binary modulation, which is based on the emission of two levels of intensity of the optical signal according to the data to be transmitted. Thus, a bit "1" is simply represented by an optical pulse that occupies the entire or part of the bit duration while a bit "0" is represented by the absence of an optical pulse.

  Depending on the duty cycle, OOK can be either return-to-zero (RZ) or non-return-to zero (NRZ). In OOK-NRZ, a pulse occupies a full bit duration and in OOK-RZ, a pulse occupies a specified part of the bit duration and the rest of the bit duration is represented by a zero intensity. There is also an inverted version of OOK-RZ called, return-to-zero-inverted (RZI) signalling, used on some commercial applications such as the IrDA serial infrared link [34].

  Due to its simplicity, OOK enables low-complex and low-cost transceiver implementations. The counterpart is low spectral efficiency.

- In PPM, information is represented by the position of the pulses within the symbol duration. In comparison to OOK, PPM has the advantage of containing the same amount of optical energy within each symbol. In addition, PPM needs less electrical or optical power than OOK for achieving the same BER but M-PPM bandwidth efficiency is $\log_2(M)/M$, which is lower than OOK (1bit/s/Hz). For this reason, PPM is usually used in power sensitive systems where bandwidth is not a major concern. However, PPM imposes more system complexity compared to OOK since both slot- and symbol-level synchronizations, critical to system performance, are required at the receiver. Besides, in the presence of multipath, PPM does not perform well due to the need to find the correct pulse position.

License CC BY-NC-ND 3.0

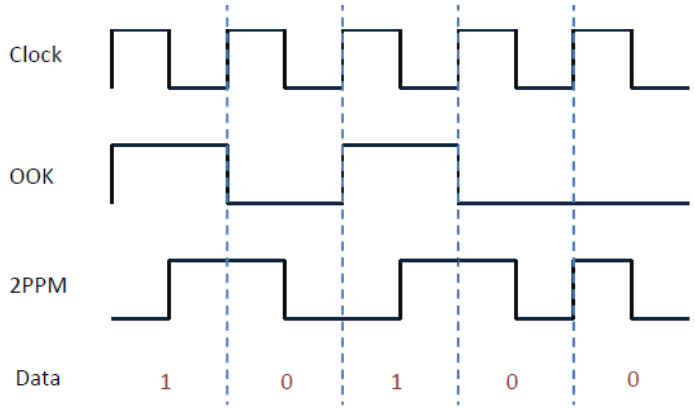

Figure 2.21. Example of OOK-NRZ and 2-PPM signals

- PWM is a modulation for which the pulse width in a time interval is varying. Variable PPM (VPPM) combines PPM with PWM and is compatible with a dimming control for VLC [23]. Bits "1" and "0" in VPPM are distinguished by the position of a pulse, whereas the width of the pulse is determined by the dimming ratio positions.

- In contrast to binary intensity modulations such as OOK and PPM, Pulse Amplitude Modulation (PAM) is a multilevel intensity modulation scheme. To provide non-negative optical signals, unipolar M-level is used. The bandwidth efficiency of M-PAM is $\log_2(M)$ bit/s/Hz, therefore, it could provide a higher bandwidth efficiency than OOK and PPM but at the expense of reduced power efficiency.

Single carrier modulation techniques are simple to implement and of low complexity for relatively low data rates.

At high data rates, the signal can be affected by inter-symbol interference (ISI) because of multipath propagation or when the components used have limited bandwidth. To mitigate ISI one can use techniques of equalization but which are complex to implement when using single-carrier modulations.

Multiple carrier modulations are a suitable solution in this case.

II.6.2. Multiple-carrier modulations

Multiple carrier modulations generally include discrete multi-tone (DMT) and orthogonal frequency division multiplexing (OFDM) [115]–[118]. Based on multiple frequencies of orthogonal subcarriers, a broadband channel is subdivided into a number of narrow-band sub-channels. Each sub-channel can be considered as a non-frequency-selective one, which enables a low-complex channel equalization. Another inherent advantage of OFDM is supporting multiuser communication systems where each user could be allocated to certain subcarriers.

License CC BY-NC-ND 3.0

OFDM has attracted a lot of attention for OWC in particular for VLC and Li-Fi application requiring very high-data rates. Since OWC uses IM/DD, the way of generating OFDM signals need to be modified compared to RF. Actually, the signals have to be real and positive.

To produce real signals, Hermitian symmetry is required in the block of symbols before inverse fast Fourier transform (IFFT).

To satisfy the unipolarity condition, the proposed methods are various. The main one is adding a DC bias (DC-biased optical OFDM (DCO-OFDM)) [115]. However, OFDM signals have a high Peak-to-Average Power Ratio (PAPR) that leads to the transmitter LED working in the non-linear region, introducing distortion to the transmitted OFDM symbol. Other techniques of unipolar OFDM have been studied as an alternative to DCO-OFDM. These include methods based on clipping at zero and transmitting only the positive parts of the signal (asymmetrically clipped optical OFDM (ACO-OFDM)) [116] and PAM-DMT [117] using real-valued PAM symbols to modulate the sub-carriers instead of complex ones. A review of the different OFDM techniques for Li-Fi application is provided in [119].

II.7. Conclusion

We have introduced in this chapter fundamental concepts for IR and visible link design. These include the IM/DD channel, the characteristic of transmitter and receiver front-end elements, the noise sources, the classification of OWC links (both LOS and NLOS), and the main digital modulation techniques.

With these concepts and considering the context and objectives of the thesis, we will consider non-directed NLOS channels for both IR uplink and visible downlink.

Concerning IR uplink, we do not study the IR receiver front-end characteristics but focus on two parameters of IR source: half-power angle and emitted power. On the other hand, we study the positions and orientations of sources and receivers of non-directed NLOS link by taking into account objects such as the body.

For VLC downlink we assume an ideal Lambertian LED (m=1) and investigate the non-directed NLOS VLC channel related to the optical properties of the environment and of the body carrying a typical VLC receiver.

The analysis of IR and visible channels are developed in the two following chapters.

The performance of the monitoring scenario based on IR uplink and visible downlink are evaluated in Chapter V for an OOK modulation since the targeted bit data rates for medical monitoring are not high enough to justify the use of more complex modulations.

License CC BY-NC-ND 3.0

License CC BY-NC-ND 3.0

CHAPTER III. MOBILE IR CHANNEL BEHAVIOR

III.1. Introduction

In this chapter, we study the theoretical behavior of the infrared channel corresponding to scenarios of uplink transmission between a sensor carried by a mobile user and various receivers on the ceiling.

The theoretical approach by simulation as well as the associated tool, which is the software RaPSor developed in the team, are presented in the first part.

We define the simulated scene and the transceiver key parameters to be optimized regarding user mobility within the whole environment. Because of random behavior, the analysis relies on the probability density function (PDF) and cumulative density function (CDF) of the channel gain.

Single-Input Single-Output (SISO) configuration for an empty room is first considered as a basic simulation. Then, the two scenarios envisaged in Single-Input Multiple-Output (SIMO) configuration are defined, in particular, the scenario of interest for the thesis called scenario (b) where the multiple receivers are included in a single lighting module, in the center of the environment. The statistical analysis of the channel according to the transceiver parameters is first done by considering an empty room. Then we detail the modeling adopted to take into account the presence of the body in the scenario (b) and study the impact of the body on the behavior of the channel.

The main conclusions of the theoretical simulation study are validated by the experimental results presented in the last part of the chapter.

III.2. Channel simulation tools

The study of the behavior of the optical propagation channel, including the impact of mobility and obstacles (furniture, people, etc.) is necessary to implement an OWC system. However, characterization of the channel in a complex environment requires long and complex measurements.

Another approach is to simulate the behavior of the optical channel in realistic environments by calculating its impulse response. Such calculation is based on the integral of Light Transport Equation (LTE), which reflects the distribution of optical energy in a scene. To

License CC BY-NC-ND 3.0

determine this equation, several numerical methods have been proposed as introduced in Chapter 2. The methods, which offer today the best performance in terms of precision and computing time, rely on ray tracing and on Monte Carlo integration (Monte Carlo Ray-Tracing (MCRT) methods).

We focus here on a software tool using MCRT based algorithms for optical wireless communication, named RaPSor [120].

III.2.1 Monte-Carlo Ray Tracing methods

In the context of the OWC channel the first MCRT method, called MCA "Monte Carlo Algorithm", was proposed by Lopez -Hernandez and. al in 1998, [121]. This method involves discretizing the surfaces of the room (walls, floors, and ceiling) into small cells, generating the rays based on a given statistical distribution, and then tracking each ray until it reaches the detector to calculate the power value and associated delay.

One limitation of MCA is linked to the fact that the probability the rays reach the receiver is not high, and so a very large number of rays is needed. Therefore, this method has been improved by developing a modified algorithm taking into account this issue (Modified MCA - MMCA) [122]. There are also hybrid approaches using the accuracy of recursive methods in addition to the speed of MC analysis [123]. Thanks to the deterministic part of the method, performance is improved compared to classical MC in particular for Multiple Inputs Single Output (MISO) cases.

A new formalism to enhance the performance with MC techniques has been recently proposed in [124] applied to indoor optical propagation scenario. A new Monte Carlo Shooting algorithm (MCS) especially efficient for Single Input Multiple Outputs (SIMO) links has been developed. A second one is Monte Carlo Gathering algorithm (MCG) reversing the direction of the optical waves propagation and calculating the power contributions of all sources in a single computation step. In addition, two other algorithms based on the principle of Markov Chain associated with the Monte Carlo method (MCMC) have been also implemented showing great efficiency for very complex environments [125].

We use in the thesis MCRT software tool named RaPSor developed from the works of [84,124] and present it in the following paragraphs.

III.2.2 Introduction about RaPSor

RaPSor is the acronym for Ray Propagation Simulator. It is an open and extensible tool, based on the NetBeans platform developed in XLIM laboratory for more than 10 years [120].

License CC BY-NC-ND 3.0

We use here RaPSor version 2.3 to model and simulate 3D environments including optical transmitter and receivers in order to study OWC scenarios performance. The different steps using RaPSor for channel simulation are illustrated in Figure 3.1.

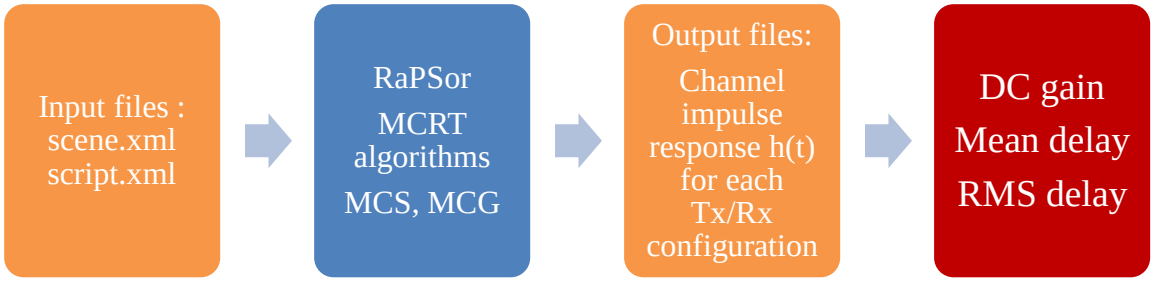

Figure 3.1. Description of RaPSor steps for channel simulation

RaPSor needs a simulation file coded in XML language (in the thesis we named it *scene.xml*) defining all the needed parameters. It is also possible to define another file in order to run several simulations in the queue to traduce for example object movement (*script.xml*). They are briefly presented in the following paragraphs.

The RaPSor output file is also an XML file that contains the impulse response discretized in time for the configuration of the transceiver link studied. From the impulse response, we can extract the results and calculate channel gain and delays.

III.2.2.1 Simulation scene file

The simulation scene file includes various parameters related to the environment and transmitters/receivers (see Figure 3.2). To create this file, we use Matlab© (detailed in the appendix from 01 to 05).

License CC BY-NC-ND 3.0

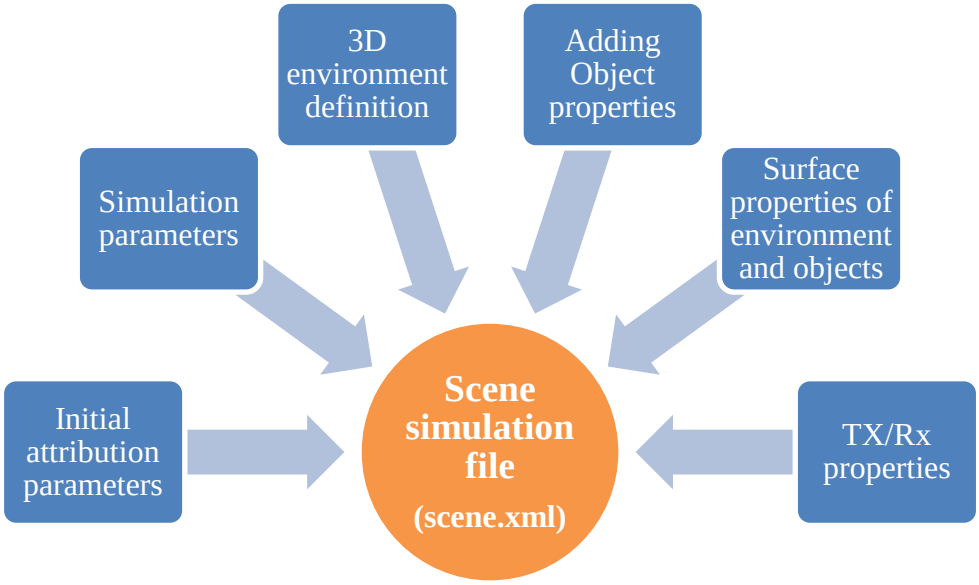

Figure 3.2. Parameters for scene simulation file

One of the first steps is the description of the 3D scene by defining the plane surfaces of the environment. For example, to model an empty cubic room, six flat surfaces need to be defined.

The coordinates [XYZ] (m) of the four points corresponding to the edges describe each surface. It is illustrated in Figure 3.3 for an example where we have reported the associated XML code.

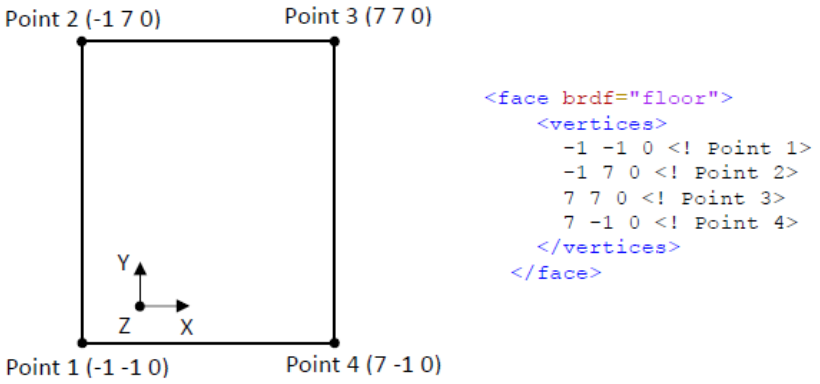

Figure 3.3. Example of surface definition and associated XML code

Each surface is named (in Figure 3.3 the surface is named “floor”). This name will be used to define the reflectivity property of the light on this surface (Bidirectional Reflectance Distribution Function BRDF). In the thesis, we consider ideal Lambertian surfaces.

In addition to surfaces, we have to define transmitters (Tx), receivers (Rx) and objects in the scene. Table 3.1 presents the requested parameters of Tx and Rx.

License CC BY-NC-ND 3.0

An object corresponds to an association of surfaces and/or transmitters and/or receivers. It possesses its own coordinate system. Figure 3.4 gives an example of an object composed of one surface and one transmitter. Their positions are defined according to [X'Y'Z'] coordinate system, meaning that to move all the components of the object, we just have to move its origin considering the [XYZ] system.

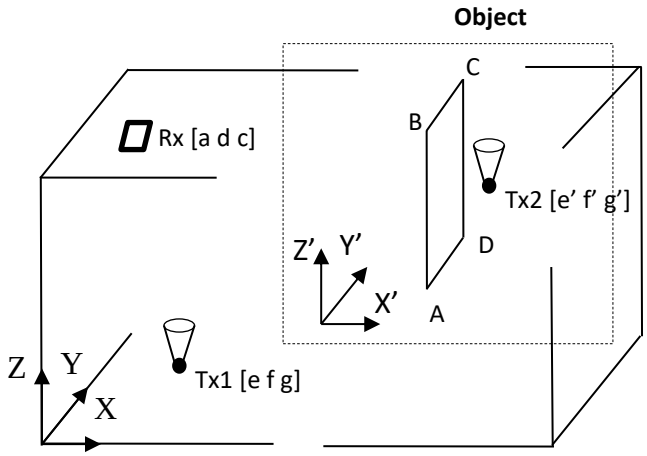

Figure 3.4. Illustration of Transmitter, Receiver and object 3D definition.

Among the initial attribution properties, the main important ones are the simulation mode, the number of rays used for the simulation, the step for the impulse response and the duration of the observation in seconds.

Currently, RaPSor version 2.3 contains 3 simulations modes that are Single-Input Single-Output (SISO), Multiple-Input Single-Output (MISO) and Single-Input Multiple-Output (SIMO). In addition, you can choose between 4 algorithms: MCS (Shooting), MCG (Gathering), MCMCS and MCMCG.

For SISO and MISO simulations, it is better to use the Gathering mode with at least 40000 rays in order to obtain accurate impulse response. For SIMO simulation, the Shooting mode is more suitable with at least 1500000 rays.

As we have said, RaPSor allows the creation of scripts. A script permits to launch several simulation files consecutively or to use moving objects in a simulation.

License CC BY-NC-ND 3.0

III.2.2.2 Run RaPSor

There are two ways to run RaPSor: use the rapsor.exe file (Windows) or run a script by using terminal command. As an example, Figure 3.5 shows the interface of the simulation launched from windows. It displays a 2D scene with 10000 random positions of transmitter Tx.

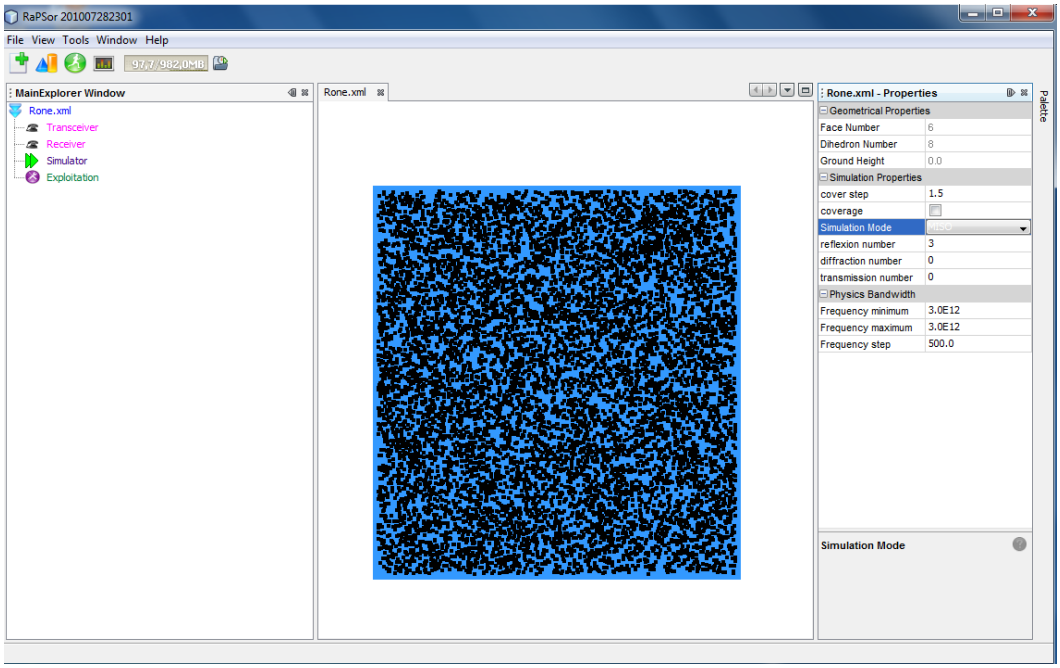

Figure 3.5. Example of 2D interface of RaPSor

The RaPSor simulation result file (.xml) contains the impulse response for each configuration (Tx/Rx) defined. The file gives us the full impulse response and the impulse response for different numbers of optical reflection separately.

We have developed Matlab© (detailed in appendix 06) programs to exploit the results.

III.3. Simulation of the IR channel

In this paragraph, after the definition of the environment and assumptions used we introduce the simulation results of a basic empty room and SISO configuration, illustrating our approach to analyze IR channel behavior.

The two main SIMO scenarios investigated are then presented. The first one corresponds to a classical case considering spatial diversity at the reception to ensure coverage. The method is to distribute the IR receivers uniformly over the room ceiling. This is a scenario already studied but considering only one location of the transmitter on the upper part of the patient body

License CC BY-NC-ND 3.0

[85]. We deepen here the channel study considering others locations in particular below patient knees. For this purpose, a 3D body model is proposed.

The new approach of spatial diversity in the second scenario is to consider that all IR receivers are included in a unique lighting device located at the room center. This is the scenario corresponding to the thesis objectives.

III.3.1. Definitions

We define a room where the IR transmitter Tx is placed at a given distance H_T from the floor. The Tx orientation regarding its normal axis is defined by the angle β (see Figure 3.6). This angle can randomly vary to simulate user movements. Moreover, to model the fact that the user carrying Tx is mobile, we consider that the 2D Tx coordinates [X Y] are randomly and uniformly distributed.

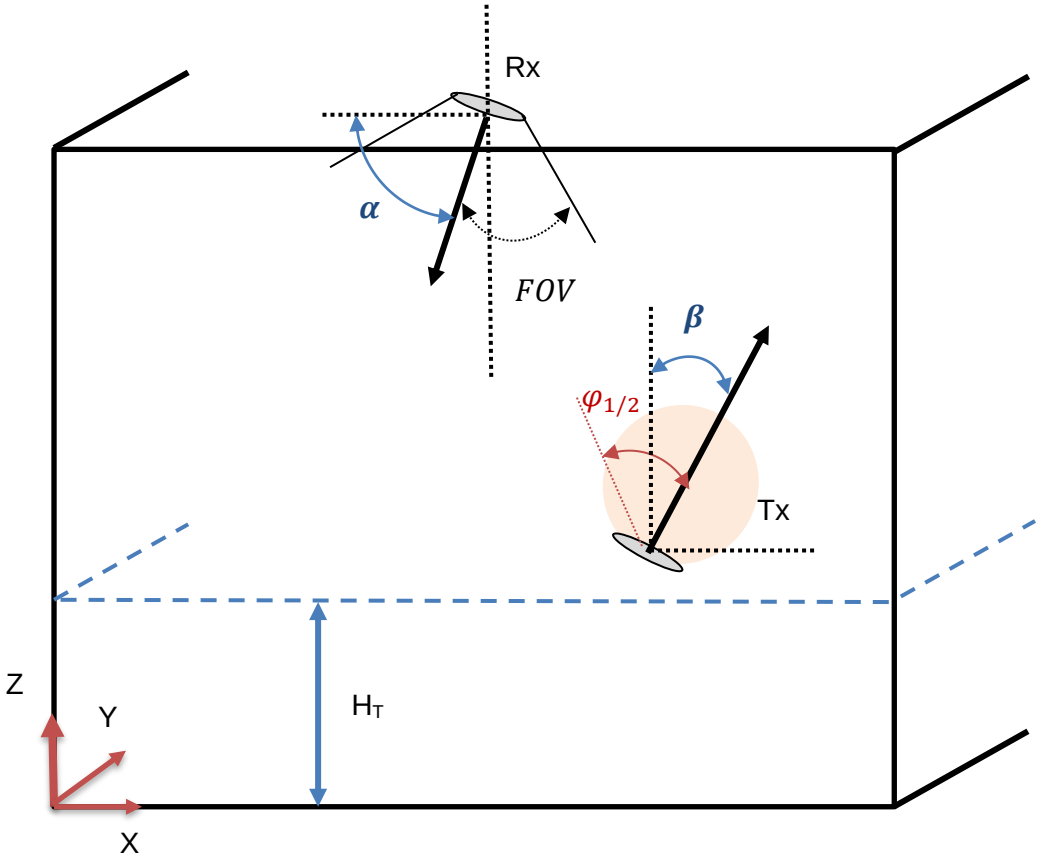

Figure 3.6. Scene geometry definition

The receiver Rx is located at a given position on the ceiling, its orientation defined by the angle α. There is no tracking system between Tx and Rx. The received optical power is thus due to the power from LOS and NLOS paths, i.e. reflected paths over the room surfaces. In the thesis, we suppose that all indoor surfaces and objects present in the room are ideal Lambertian

License CC BY-NC-ND 3.0

surfaces so the reflections are purely diffuse.

For a given environment, RaPSor provides the impulse response $h(t)$ for one configuration of (Tx, Rx) depending on their geometrical parameters (Tx coordinates [X Y H_T], Rx coordinates, angles α and β) and physical parameters of Tx and Rx (half-power angles $\varphi_{1/2}$ and FOV, Rx physical active area A_r).

From $h(t)$ and according (2.19) we can determine the DC gain H_0 which is one of the most important features of the IR channel. As we suppose different link configurations related to movements and mobility of Tx, our approach is thus to consider a random variable H_{0-IR} taking a value among a set $\{H_0\}$ with a given probability $p(H_{0-IR} = H_0)$.

In the following, we will analyze the channel behavior from the distribution of the probabilities $p(H_{0-IR} = H_0)$ for the different H_0 values. This is the probability density function $PDF(H_0)$. We will also determine the cumulative density function $CDF(H_0)$ defined as:

$$CDF(H_0) = \int_{-\infty}^{H_0} p(H_{0-IR}) dH_{0-IR} \quad (3.1)$$

The CDF allows evaluating the IR link reliability. Indeed, DC gain impacts link performance. The higher the gain in dB, the higher the power received and therefore the performance of the link. Consequently, from CDF analysis, the goal is to reach the highest possible DC gain values with the lowest CDF.

Moreover, time dispersion parameters defined by equations (2.20) and (2.21), related to impulse responses length and mean delay spreading, can be obtained from simulation results.

In the next parts, we first consider basic scenarios with an empty room.

III.3.2. Single-Input Single-Output (SISO) configuration in an empty room

The studied environment is a rectangular room of dimensions (XYZ) = (6.7×6.6×3) m^3. This corresponds to the room for experiments presented at the end of the Chapter.

In this part, we assume that the room is empty and that all the surface reflectivity coefficients are equal to ρ=0.8.

First, we setup a receiver on the room ceiling at a central position (see Table 3.1). This receiver Rx is slightly shifted from the ceiling (5cm) and oriented toward the floor (α=90°). It

License CC BY-NC-ND 3.0

receives signals from a transmitter Tx randomly positioned in a 2D plane at the height H_T= 1.5m from the floor. The Tx orientation is fixed perpendicular to the 2D plane so β=0°.

All the other parameters are shown in Table 3.1.

Table 3.1. SISO configuration –empty room

Parameter	Values
Transmitter Tx	
Number of transmitters	1
Tx Position number	[10, 10000]
Tx orientation angle β (°)	0
Tx Lambertian order m	2
Distance from the floor H_T (m)	1.5
Receiver Rx	
Rx coordinates [XYZ] (m)	[3.35 3.3 2.95]
Rx orientation angle α (°)	90
physical active area A_r (m²)	0.0000345
Field of View FOV (°)	45
Number of receivers	1
Responsivity (A/W)	1
Environment	
Dimensions	6.7*6.6*3 m
Number of optical reflections *k*	3
Reflectivity coefficient of surfaces	0.8
Objects inside the room	Empty

For one position of the Tx in the room, RaPSor provides the impulse response as shown in Figure 3.7 as an example. We have plotted two impulses responses corresponding respectively to an emitter close to the room center (Figure 3.7 (a)) and another one in the corner. (Figure 3.7 (b)).

License CC BY-NC-ND 3.0

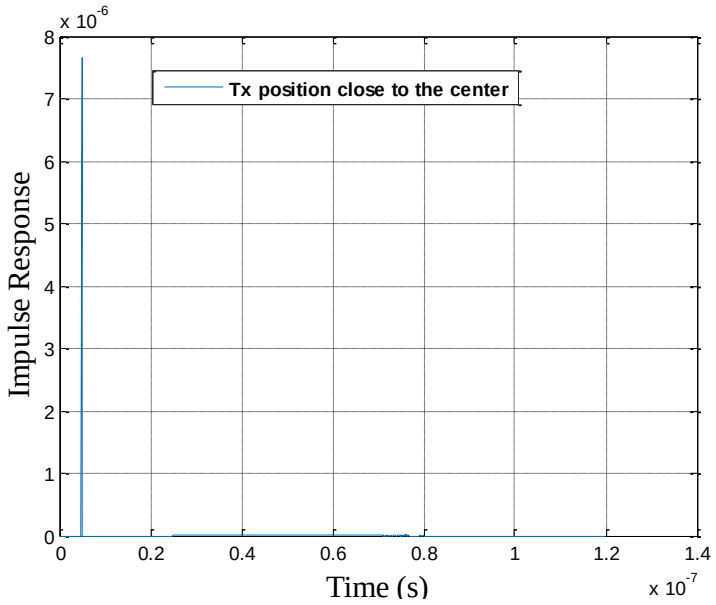

Figure 3.7.(a). Example of impulse response for Tx close to room center

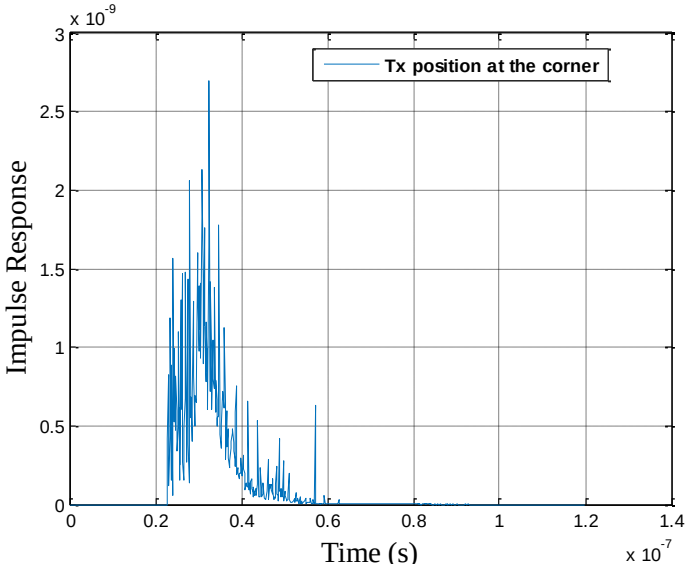

Figure 3.7.(b). Example of impulse response for Tx at the room corner

As expected, we remark that for the position close to the center, the LOS path dominates and the reflective parts are negligible. On the other hand, at the corner of the room, there is no LOS contribution and the receiver collects only reflective beams.

To study delay parameters, we have considered 50 positions of Tx on the room diagonal. From RaPSor results, we have evaluated the mean excess delay and the RMS delay spread τ_{RMS} as a function of the distance between Tx and Rx, which are reported in Figures 3.8 (a) and (b).

License CC BY-NC-ND 3.0

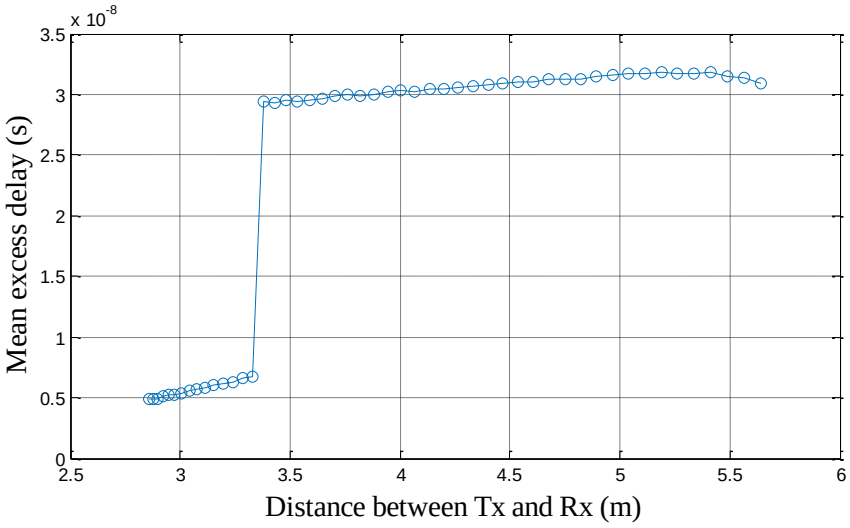

Figure 3.8.(a). Mean excess delay for 50 Tx positions

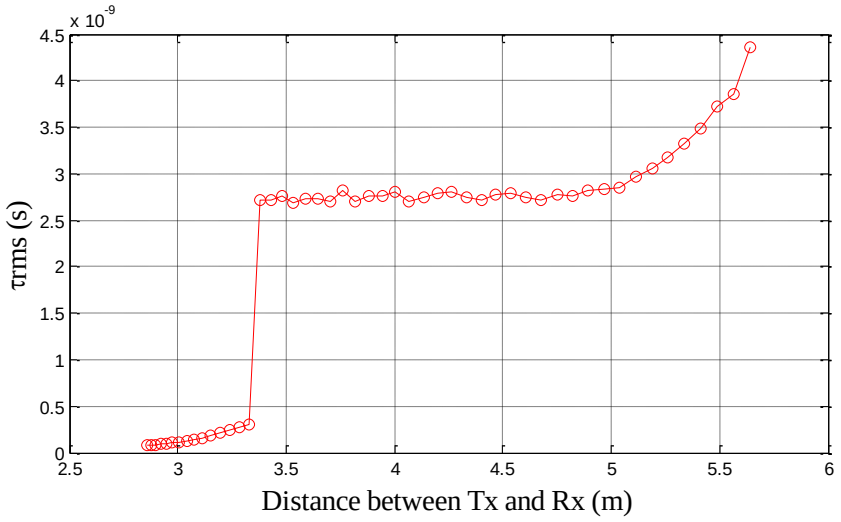

Figure 3.8.(b). RMS delay spread for 50 Tx positions

As expected, we can verify in Figure 3.8 that the mean excess delay and the delay spread τ_{RMS} increase with the distance. To avoid multipath dispersion, the delay spread should be significantly shorter than the symbol period that is $\tau_{RMS} \ll T_s$. This implies a maximal symbol rate R_s allowing neglecting ISI:

$$R_s \leq \frac{1}{10\tau_{RMS}} \qquad (3.2)$$

Thus, taking into account the values of τ_{RMS} we can verify that the maximal symbol rate is always lower than hundreds of Mbps. Therefore, in our context where the data rates are not very high [82], classically lower than 10Mbps, we can neglect multipath propagation impact and thus focus on the DC gain for channel analysis.

License CC BY-NC-ND 3.0

To accurately analyze the statistical distribution of DC gain, we have to consider a minimal number of Tx positions. Figure 3.9 shows $PDF(H_0)$ for the studied configuration, for different numbers of Tx coordinates on the 2D plane.

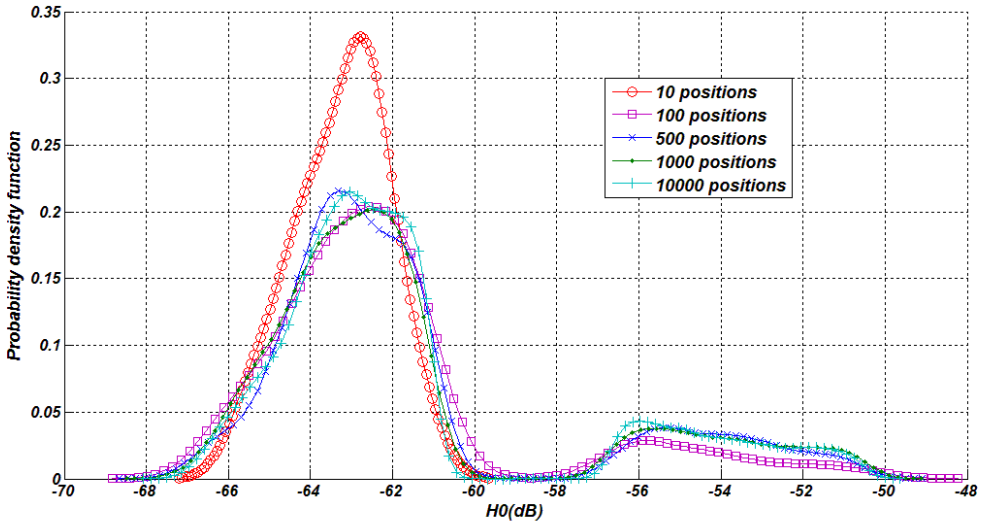

Figure 3.9. $PDF(H_0)$ as a function of number of transmitter's position

We notice that the curves are identical from 100 points. To confirm this, we have plotted $CDF(H_0)$ for the same Tx position numbers. The results are reported in Figure 3.10 and lead to the same conclusions. In the following, we consider 1000 random Tx positions to have good result convergence.

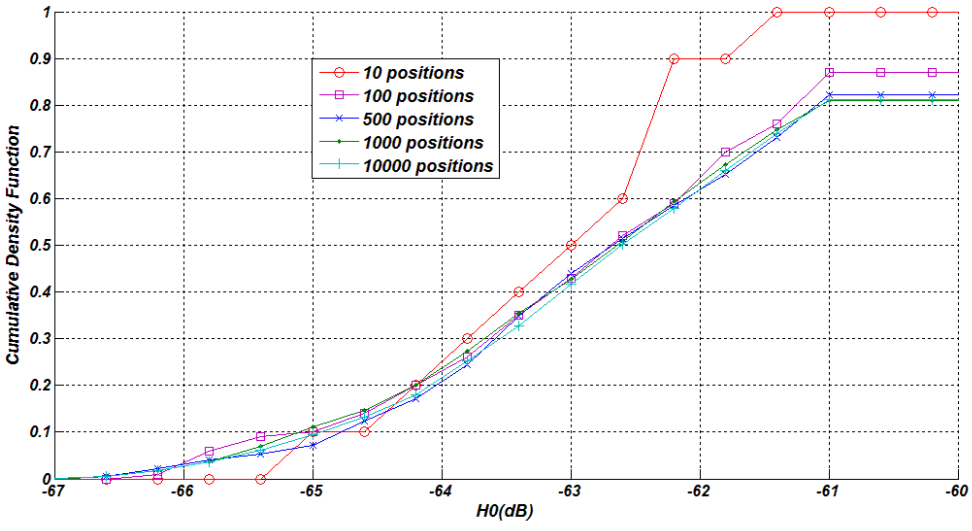

Figure 3.10. The CDF as a function of number of transmitter's position

License CC BY-NC-ND 3.0

To complete, the computation time using RaPSor in SISO mode with MCG algorithm (on a computer with CPU ES 2609v3 (1.9 GHz) RAM 32GB 64bit) is around 5mn for 1000 transmitters/receiver configurations.

III.3.3. Single-Input Multiple-Output (SIMO) in an empty room

Due to their potential, multiple transmitter-receiver techniques are already widely used in several RF communication systems. For FSO transmission, the effects of MIMO schemes have been already studied. It has been shown that MIMO can mitigate the fading effect caused by the atmospheric channel impairments [124]. For indoor communications, Optical MIMO technologies have been investigated for VLC to improve data rate and coverage [125].

In our context, we consider spatial diversity only at the reception (SIMO). The idea of using several spatially separated photodetectors is used to increase the chance to collect the signal emitted by the transmitter moving in the room. Associated to linear combining techniques this increases performance.

There are various combining techniques at the reception [126] such as selection combining (SC), where only the signal with the largest Signal to Noise Ratio (SNR) is processed. All other signals are neglected. Hence, SC can also be considered as an antenna selection scheme. In contrast to SC, maximum ratio combining (MRC) weights the received signals according to their individual SNR and combines all of them for further processing. As a result, MRC maximizes the SNR at the combiner output. A simplified version of MRC is equal gain combining (EGC) which equally weights all signals before they are combined.

To ensure coverage, the most conventional approach is to distribute the IR receivers uniformly over the ceiling with perpendicular orientation, so that they are oriented towards the floor. This has been previously studied in [85,127] where four receivers are deployed and SC technique used for combining. Considering emitters most of the time oriented toward the ceiling, this configuration allows for more LOS links, which are the best performing ones. We will name this configuration **scenario (a)** in the following.

However, depending on the environment configuration is not always possible to distribute the receivers over the ceiling. One solution is to position them with the luminaires dedicated to the VLC downlink. As the positions of the luminaires are not necessarily optimized to ensure the infrared uplink coverage, it is thus important to study IR receiver's orientation making it possible to obtain the targeted performance.

License CC BY-NC-ND 3.0

We propose here to investigate this approach considering four IR receivers included in a unique luminaire at the center of the studied environment. We assume that the lighting system is a panel that is classically installed in the ceiling of public environments e.g. hospitals, or schools (see Figure 3.11). Therefore, the receivers are supposed to be set off 20 cm from the ceiling. This is named **scenario (b)**. The two scenarios (a) and (b) investigated are illustrated in Figure 3.12.

Figure 3.11. LED panel examples [131]

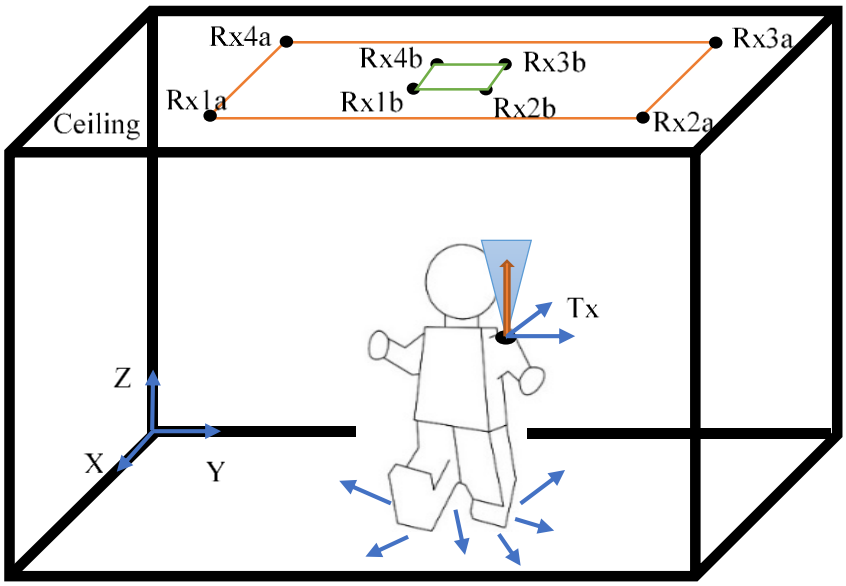

Figure 3.12. Illustration of scenarios (a) and (b) for IR channel

License CC BY-NC-ND 3.0

We use for both scenarios the same diversity technique that is SC. As the SNR depends on the value of received power, we consider the signal with the lower attenuation i.e. the highest value of the DC gain in dB.

For each scenario and for a transmitter characterized by its geometrical parameters (position and orientation), each receiver Rxj (with j=1 to 4) receives a signal with a given attenuation, so it corresponds to an optical gain H_j.

We define H_{0-IR} corresponding to the best DC gain considering four receivers:

$$H_{0-IR} = \text{Max}[H_1, H_2, H_3, H_4] \qquad (3.3)$$

As the emitter position is random, H_{0-IR} follows a statistical distribution $p(H_{0-IR})$. The CDF of the gain can be thus expressed using equation (3.1) as previously.

III.3.3.1. Study of scenario (a)

The configuration parameters for scenario (a) are described in Table 3.2. The Tx orientation angle β=0° because we are still considering an empty room. As we do not take into account the presence of the person carrying the emitter, it is not interesting to vary the angle β because this would be not realistic.

We first consider the same configuration as in [85] with our room dimensions. The transmitter is at H_T =1.5m from the floor and we consider 1000 random Tx positions in the 2D plane. Our objective is to verify that the optimal value of the Tx half-power angle $\varphi_{1/2}$ is the same as in [85] i.e. $\varphi_{1/2} = 45°$ corresponding to Lambertian order $m = 2$. This result is in accordance with published ones [129]. Therefore, we have plotted in Figures 3.13 and 3.14, the $PDF(H_0)$ and $CDF(H_0)$ as a function of *m*.

Using (2.8) table 3.3 reports the different half-power angles $\varphi_{1/2}$ values as a function of *m*.

Table 3.2. SIMO configuration scenario (a) – empty room

Parameter	Values
Transmitter Tx	
Number of transmitters	1
Tx Position number	1000
Tx orientation angle β (°)	0
Tx Lambertian order m	Variable : to be optimized

License CC BY-NC-ND 3.0

Distance from the floor H_T (m)	[0.2; 1.5]
Receivers Rx	
Rx coordinates [XYZ] (m)	[1.65 5.025 2.95] [4.95 1.675 2.95] [1.65 1.675 2.95] [4.95 5.025 2.95]
Rx orientation angle α (°)	90
Physical active area A_r (m²)	0.0000345
Field of View FOV (°)	45
Number of receivers	4
Responsivity (A/W)	1
Environment	
Dimensions	6.7*6.6*3 m
Number of optical reflections *k*	3
Reflectivity coefficient of surfaces	0.8
Objects inside the room	Empty

Table 3.3. Relation between half power angle and *m* value

$\varphi_{1/2}$ (°)	60	45	40	30	25	20	10
m	1	2	3	5	7	11	45

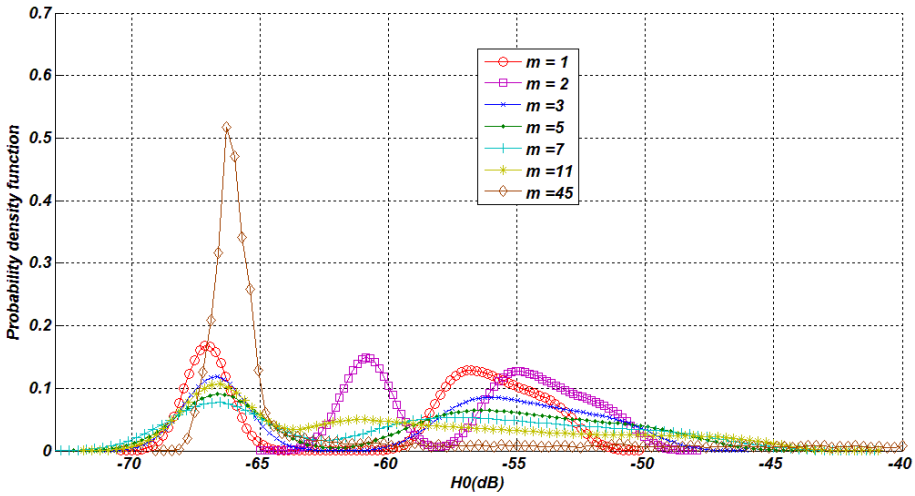

Figure 3.13. $PDF(H_0)$ for scenario (a) as a function of *m* values; H_T=1.5m; α = 90°

License CC BY-NC-ND 3.0

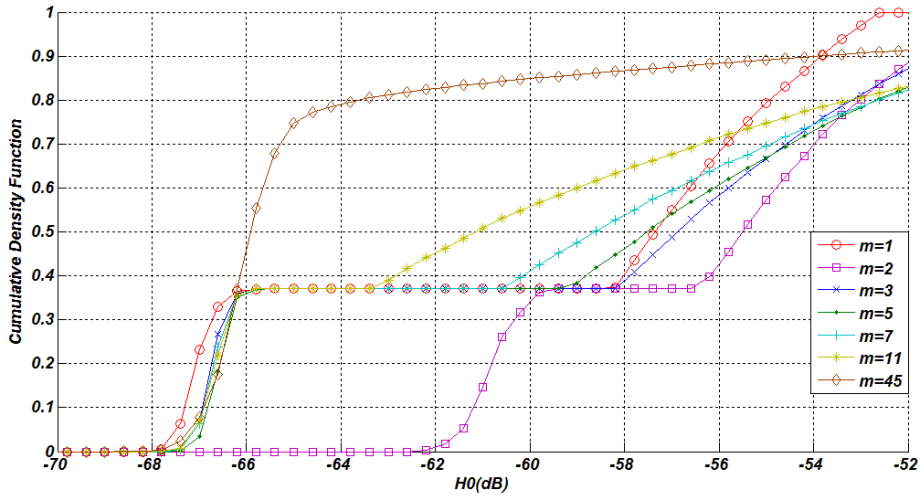

Figure 3.14. $CDF(H_0)$ for scenario (a) as a function of *m* values; H_T=1.5 m; $\alpha = 90°$

First, we verify in Figure 3.13 that for an IR source with *m* = 45, the probability of having a LOS path collected by a receiver is the lowest compared to that corresponding to the NLOS. But, as expected, the highest values of DC gain (around -40dB) are obtained for *m* = 45 because it corresponds to the most directive source. This behavior changes when *m* decreases and we observe a tradeoff between LOS and NLOS in Figure 3.13. The best compromise is for *m*=2.

Figure 3.14 confirms this result, showing that the highest value of DC gain (-62dB) obtained with the lowest CDF value corresponds to a source with *m*=2.

To verify the conclusion whatever Tx height, we now consider that the transmitter is at an extreme position that is H_T =0.2m from the floor. The corresponding $CDF(H_0)$ is plotted as a function of *m* in Figure 3.15. This shows that the value of *m* corresponding to the minimal CDF for the highest gain value (here around -58dB) is always *m*=2.

License CC BY-NC-ND 3.0

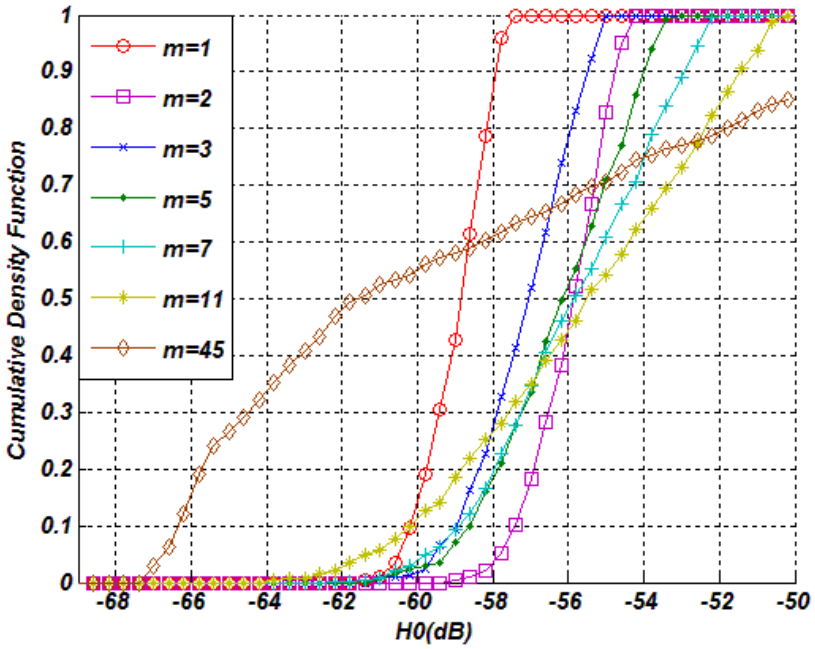

Figure 3.15. $CDF(H_0)$ for scenario (a) as a function of *m* values; H_T=0.2m

Finally, for the optimal value of *m*=2, we have reported in Figure 3.16, the $CDF(H_0)$ for different values of height H_T. As expected, the highest gain values are obtained when the transmitter is at the highest height (H_T=1.7m), i.e. for the smallest distance between transmitter and receivers. However, since the Tx position is random, the probability of achieving these values is low. On the other hand, when the transmitter is closer to the ground, it is possible to benefit from the collection of more reflected rays. Hence, there is a tradeoff and the smallest CDF value is obtained for $H_T \leq$0.5m.

This behavior with respect to the height will not necessarily be identical when taking into account the presence of the body, in particular for the positions close to the ground.

License CC BY-NC-ND 3.0

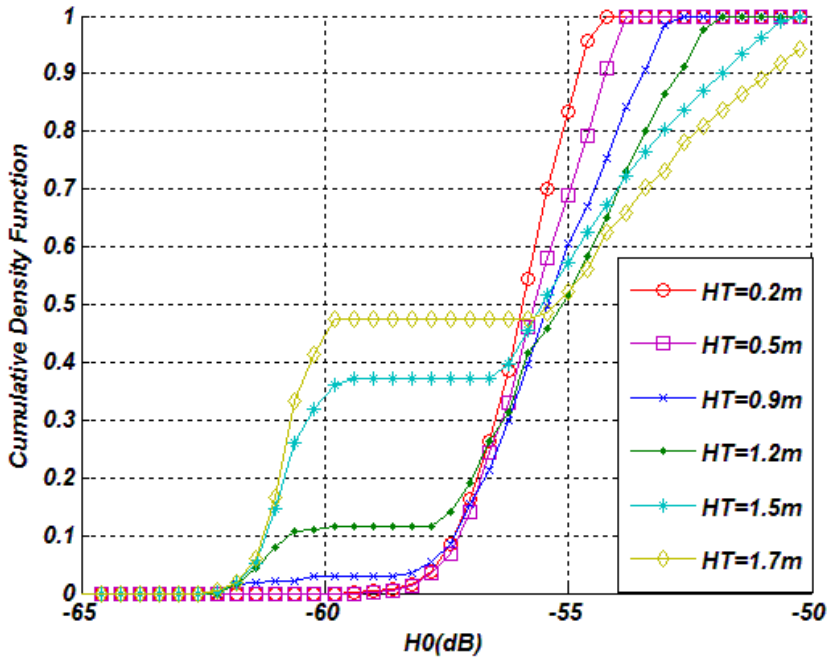

Figure 3.16. $CDF(H_0)$ for scenario (a) as a function of H_T values; m=2

III.3.3.2. Study of scenario (b)

The four IR receivers are now included at the corners of a unique flat panel at the center of the studied environment. They are set off 20 cm from the ceiling.

Our objective here is to study how to orient the four receivers to ensure the same coverage as in scenario (a). Actually, in scenario (a) the receivers were perpendicular to the ceiling. Now we want to determine the best angle value α as defined in Figure 3.6.

In addition, we will determine the optimal value of Tx Lambertian order *m*.

The configuration parameters of the scenario (b) are presented in Table 3.4.

Table 3.4. SIMO configuration scenario (b) – empty room

Parameter	Values
Transmitter Tx	
Number of transmitters	1
Tx Position number	1000
Tx orientation angle β (°)	0
Tx Lambertian order m	Variable : to be optimized
Distance from the floor H_T (m)	[0.2; 1.5]
Receivers Rx	
Rx coordinates [XYZ] (m)	[3.0 3.05 2.8]

License CC BY-NC-ND 3.0

	[3.6 3.05 2.8] [3.0 3.65 2.8] [3.6 3.65 2.8]
Rx orientation angle α (°)	Variable : to be optimized
physical active area A_r (m²)	0.0000345
Field of View FOV (°)	45
Number of receivers	4
Responsivity (A/W)	1
Environment	
Dimensions	6.7*6.6*3 m
Number of optical reflections *k*	3
Reflectivity coefficient of surfaces	0.8
Objects inside the room	Empty

First, the transmitter is located in a 2D plane at H_T=1.5m from the floor and we set *m*=2. The $CDF(H_0)$ as a function of angle α is reported in Figure 3.17. The best result is obtained for two angle values that are α=45° and α=60°.

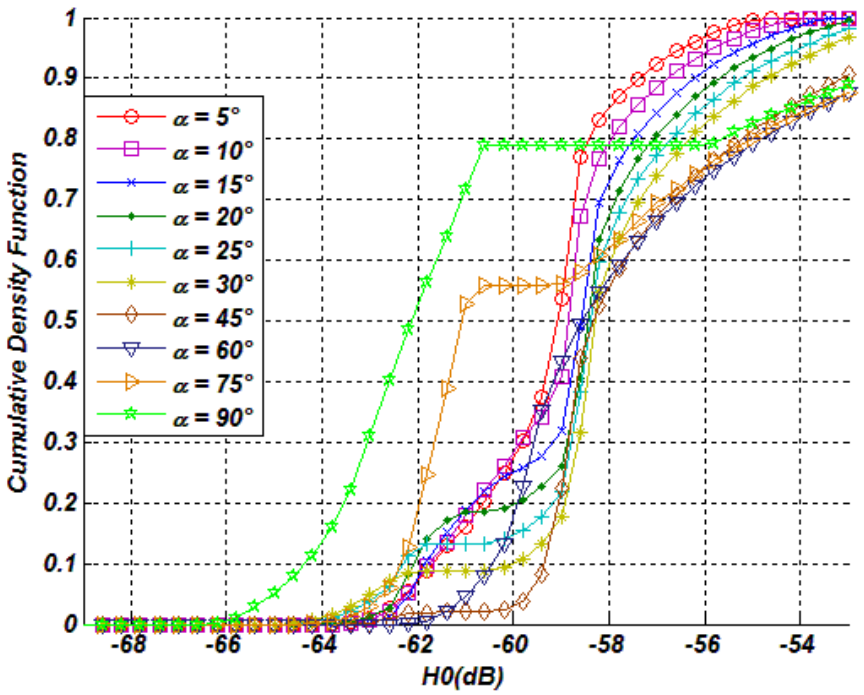

Figure 3.17. $CDF(H_0)$ for scenario (b) as a function of Rx orientation angle α, H_T=1.5m, *m*=2

License CC BY-NC-ND 3.0

For these two angle values, we have verified that the optimal Lambertian value is still m=2. As an example, we present in Figure 3.18 the $CDF(H_0)$ as a function of m, for α=45° and H_T=1.5m.

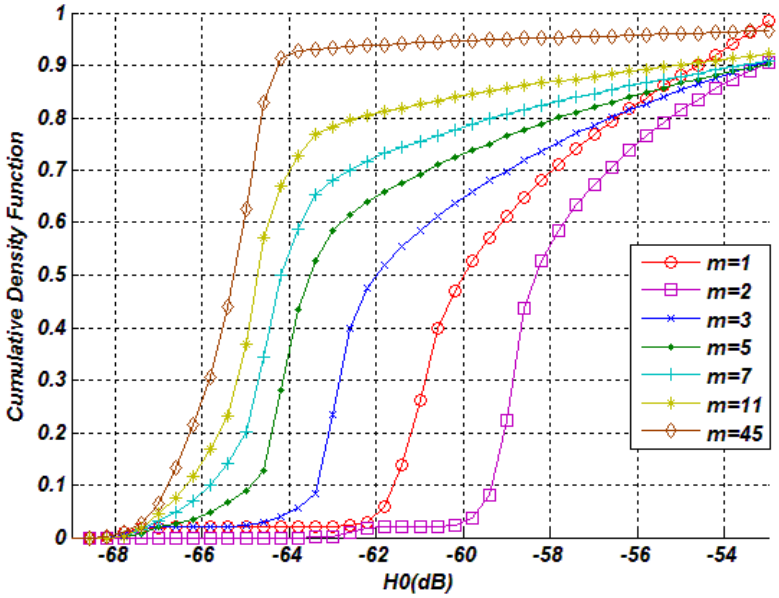

Figure 3.18. $CDF(H_0)$ for scenario (b) as a function of m; α=45°, H_T=1.5m

These results concerning optimal angle α and optimal m values are still valid when the transmitter is closer to the floor. Therefore; we finally present in Figures 3.19 (i) and (ii) the $CDF(H_0)$ as a function of H_T for α=45° respectively α=60°.

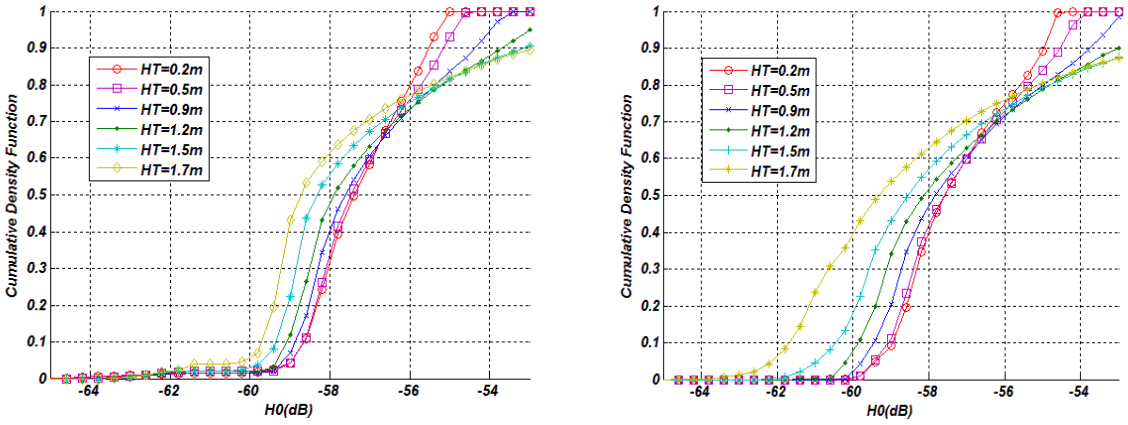

(i) (ii)

Figure 3.19. $CDF(H_0)$ for scenario (b) as a function of H_T ; m=2; (i): α=45°; (ii): α=60°

The conclusions are the same as for scenario (a). The highest gain values are obtained when the transmitter is close to the ceiling but the probability of achieving these values is low.

License CC BY-NC-ND 3.0

The smallest CDF values are obtained for $H_T \leq 0.5$m. We can notice that the corresponding DC gain values are close to the ones obtained for scenario (a).

In order to compare, Figure 3.20 shows the CDFs for the two scenarios with *m*=2 and for two H_T values: 0.2m and 1.5m. The optimal angles α, i.e. 45° and 60°, are considered for scenario (b).

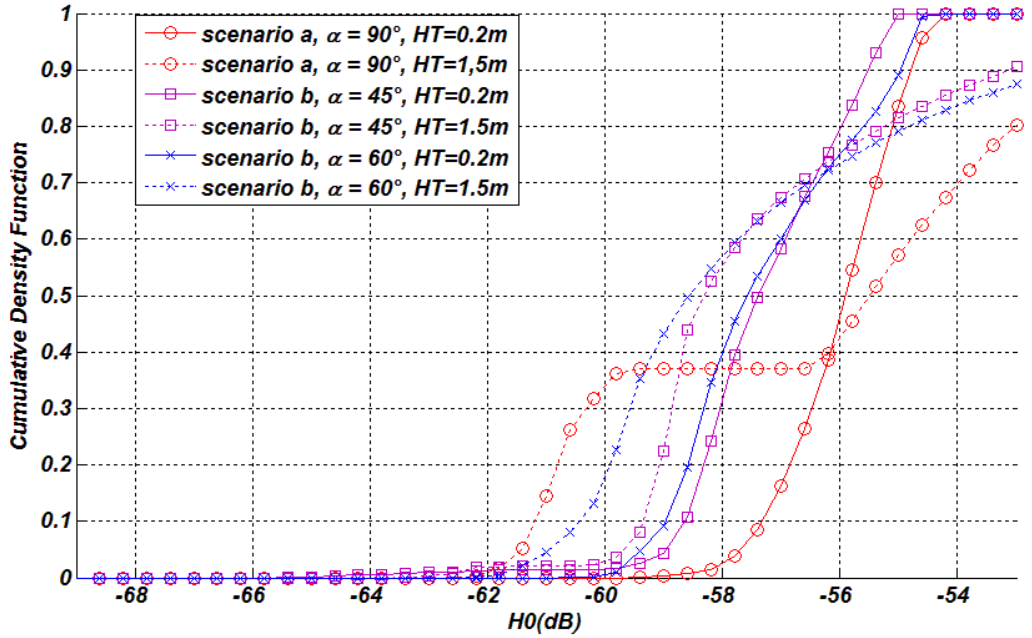

Figure 3.20. Comparison of $CDF(H_0)$ for scenario (a) and (b) H_T=0.2m; 1.5m; *m*=2; α=45°; α=60°, nobody presence.

We can conclude that the scenario (a) in an empty room corresponds to the best configuration when the transmitter is close to the ground (H_T=0.2m). On the other hand, when H_T=1.5m, this is the scenario (b) which allows the minimal CDF value for the highest gain (around -60dB).

However, a person carries the transmitter, it is thus important to study the shadowing effect because of body presence.

In the next part, we introduce the body model and study its impact on channel behavior.

III.3.4 Single-Input Multiple-Output (SIMO) with body presence

III.3.4.1 Body model

To study the impact of the human body on an optical channel, we have to model its geometry and its reflectance properties.

License CC BY-NC-ND 3.0

There are very few works on this subject regarding the IR channel. As an example, in [85] the human body has been modeled by a 2D rectangular surface. In this work, the sensor position was on the shoulder so that the IR channel behavior was not highly affected by the body presence. With the development of visible technology, other body geometries have been investigated because shadowing impact is more penalizing. For instance, the authors in [130] modeled the body as a column of 0.3m diameter and height 1m65. Moreover, for the future IEEE802.11bb, reference channels have been proposed on the basis of the 3D model of the human body with a height of 1.8m [131].

On the other hand, it has been shown that the level of detail is not so important for evaluating channel DC gain, especially when considering low data rates [84, 85].

In the thesis, we have defined an object in 3D, which can model the geometry of a human body of height 1.7m, width 40cm and thickness 20cm, but without details such as hand or foot. The model is illustrated in Figure 3.21.

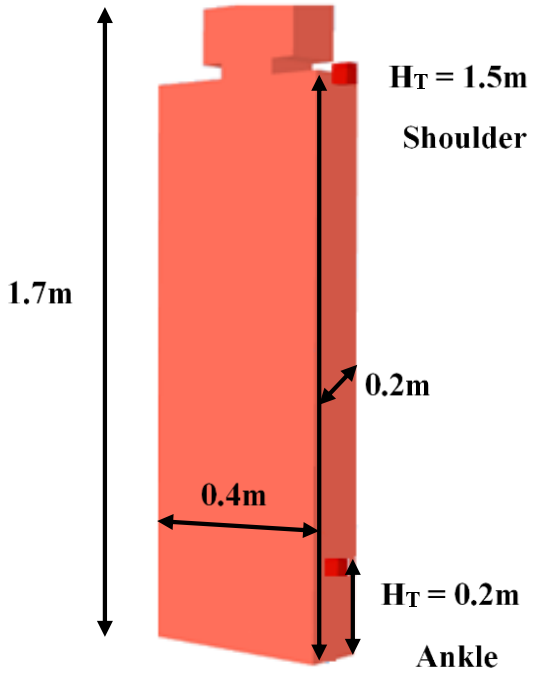

Figure 3.21. Model of human body in 3D dimension

An important question concerns the reflectance properties of the body. We suppose that an ideal Lambertian BRDF (a purely diffuse model) characterizes each surface composing the body (2D or 3D). Each surface is defined by a single parameter ρ, corresponding to the reflectivity at normal incidence. The value of ρ varies from 0 to 1. A weak value represents very absorbing surfaces, while a high value is associated with very shiny materials.

License CC BY-NC-ND 3.0

The surface of a human body exposed to light propagation is composed of two main parts, the skin and the clothes, and their ρ values vary accordingly the light wavelength [132]. As there is a large range of possible values for ρ, we will investigate for both IR and visible channels the importance of a precise value of ρ and consider in the following a range [0.1 - 0.9].

We have first compared the two scenarios (a) and (b), considering this 3D object as highly absorbing i.e. the reflectivity coefficient has been set to ρ=0.1. The results are shown in Figure 3.22, for a transmitter located at a height H_T of 0.2m respectively 1.5m.

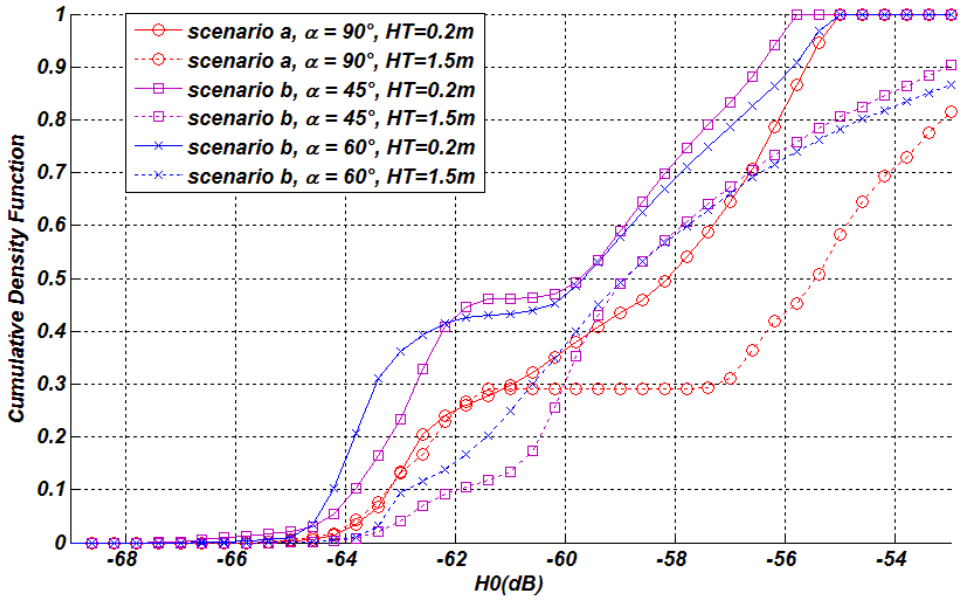

Figure 3.22. Comparison of $CDF(H_0)$ for scenario (a) and (b) with 3D body (ρ=0.1); H_T=0.2m; 1.5m; *m*=2; α=45°; α=60°

First, as expected, we notice that the DC gain values are lower than when considering scenarios without the body (Figure 3.19).

In addition, contrary to the case without a body, we verify that the results are worst when the transmitter is close to the ground, attached on the body at H_T=0.2m compared to the case where it is at the shoulder (H_T=1.5m). As previously indicated, the channel behavior is modified when the presence of the body is taken into account. Therefore, it is important to model the body for a more realistic simulation.

Besides, the minimal CDF value corresponds to a gain of about -65dB whatever the scenario or the Tx location. Thus, in the following, we focus on the scenario (b).

License CC BY-NC-ND 3.0

To illustrate the interest of 3D object to model the human body, we have compared the results with the ones obtained considering a 2D surface as in [85]. The reflectivity coefficient has been set to ρ=0.1. This is reported in Figure 3.23 for α=45° and H_T=0.2m; 1.5m.

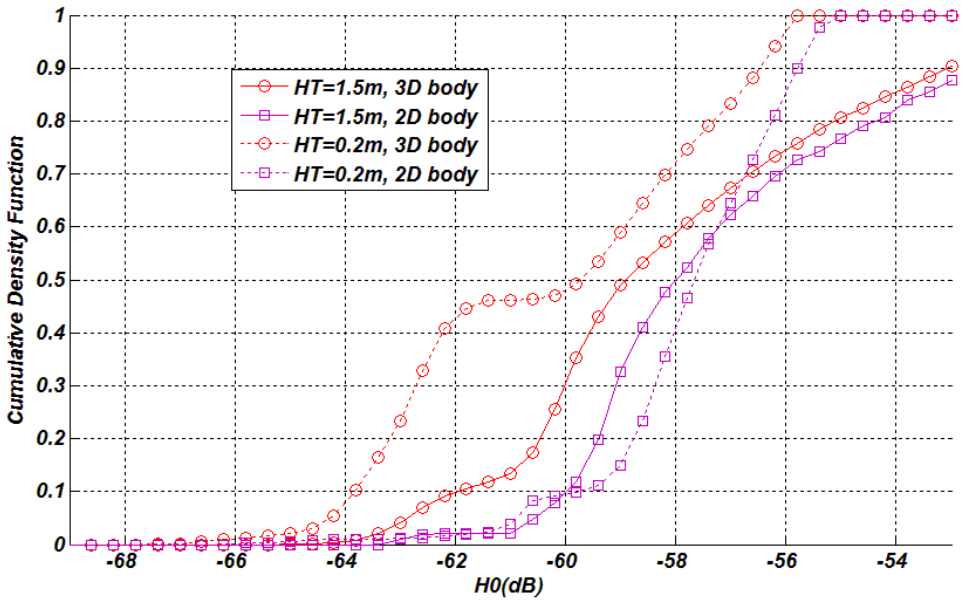

Figure 3.23. Comparison of $CDF(H_0)$ for scenario (b) with 2D and 3D body (ρ=0.1); H_T=0.2m; 1.5m; *m*=2; α=45°

For H_T=0.2m, the results in Figure 3.23 shows that modeling the 3D body leads to degraded gain values compared to the case of the 2D model. Even for a Tx position at the shoulder (H_T=1.5m), the results are impacted by the presence of the body volume, that can represent the head of the user for this position.

Consequently, the choice of 3D shape allows taking into account the blocking effects according to the location of the transmitter on the body. The different Tx positions on the body that we investigate could correspond to the connected sensor at the ankle (0.2m), knee (0.5m), twist (0.9m), belt (1.2m), shoulder (1.5m) and head (1.7m).

Besides we have tested the influence of body reflectivity value as shown in Figure 3.24 with two positions of transmitter on the body H_T= 0.2m and 1.5m.

License CC BY-NC-ND 3.0

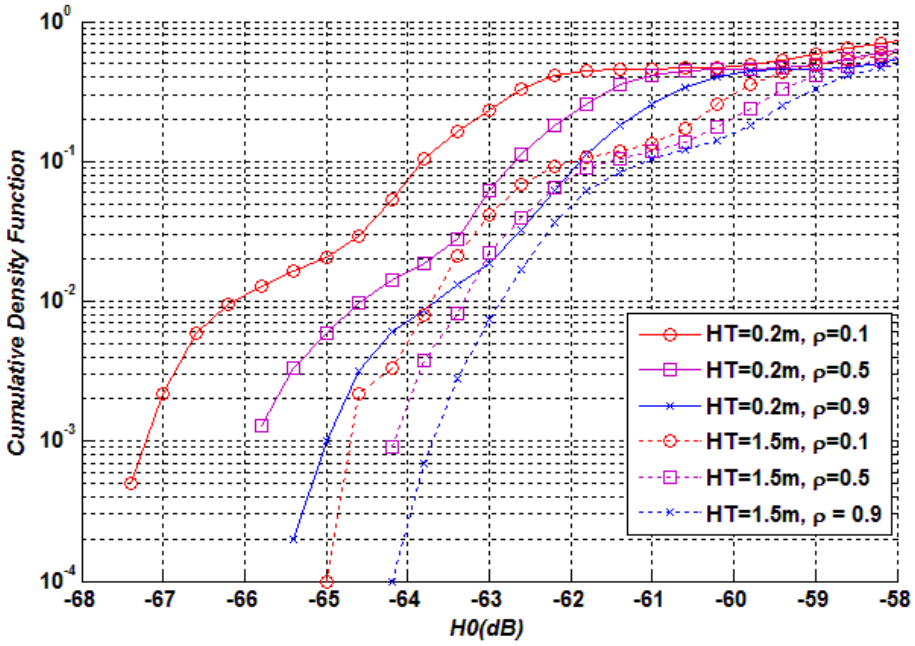

Figure 3.24. $CDF(H_0)$ scenario (b) as a function of body reflectivity ρ, H_T=0.2m and 1.5m, m=2; α=45°

As expected, we note that the more the ρ parameter decreases and the more the results are degraded. However, it is especially true for a position close to the floor (H_T=0.2m), which confirms that the presence of the body is impacting and that one must know its properties.

In the following, we deepen the analysis of body impact on the scenario (b) in particular regarding the parameter ρ.

In all the previous simulations, the Tx orientation was supposed fixed, perpendicular to the [XY] plane (β=0°). However, as the user is mobile, its movements can induce orientation changes. We study in the next part this effect considering body user presence.

III.3.4.2. Transmitter orientation

The Tx orientation regarding its normal axis is defined by the polar and azimuthal angles β and φ (see Figure 3.25). To model orientation changes of Tx, we have taken into account random variations of these angles. In addition to the case where Tx is perpendicular (β=0°) we consider that β can be tilted up to 60°: $\beta \in \left[\frac{\pi}{6};\frac{\pi}{3}\right]$ and that $\varphi \in [0;\pi]$ with a step of $\frac{\pi}{6}$ .This scenario corresponds to 13 pairs $(\varphi;\beta)$ of possible angle values.

We compare in Figure 3.26 the results obtained by considering either fixed orientation or random one for two values of Tx height on the body H_T=0.2m and 1.5m.

We observe quasi no impact on the $CDF(H_0)$ whatever the height.

License CC BY-NC-ND 3.0

To complete, we have verified this observation with α=60° and different values of body reflectivity. This allows us to simplify the IR channel simulations in the following by considering only one orientation of Tx (β=0°) to analyze channel behavior.

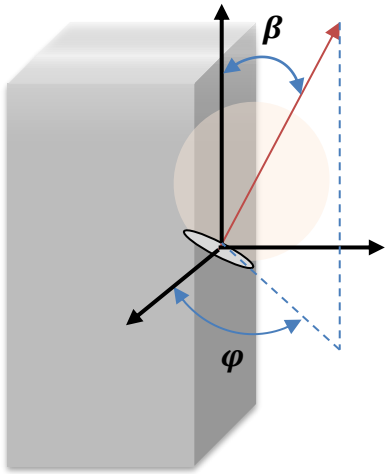

Figure 3.25. Orientation angles of Tx

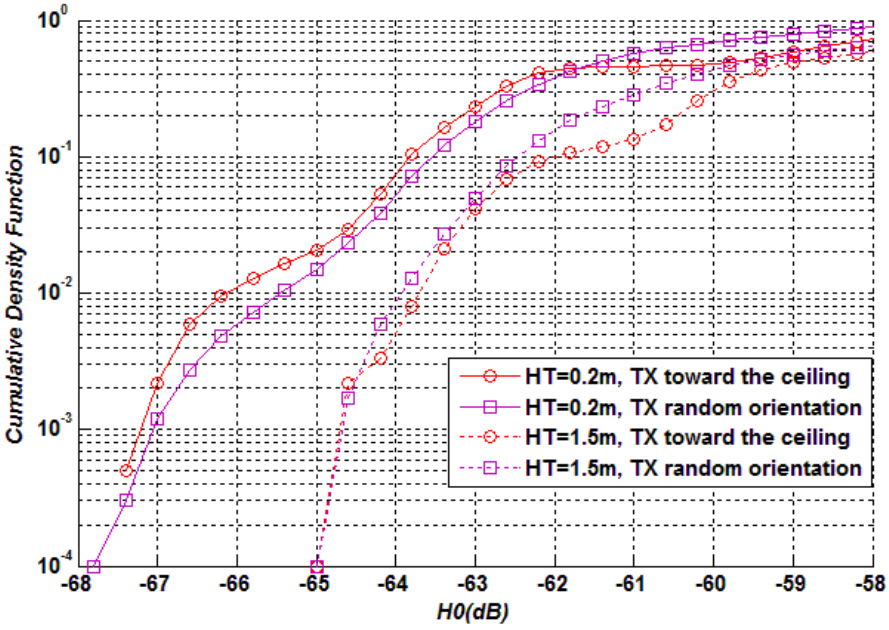

Figure 3.26. $CDF(H_0)$ scenario (b) as a function of Tx orientation; 3D body with ρ=0.1, H_T=0.2m and 1.5m, *m*=2; α=45°

III.3.4.3. Tx half-power angle

Another parameter that can be impacted by the presence of the body is the half-power angle of the source. Indeed, it is questionable whether the optimal value of *m* depends on the presence of the body and in particular its optical properties. In other words, depending on

License CC BY-NC-ND 3.0

whether the body is rather blocking or reflective, we should choose a source with a different directivity.

We have thus studied the $CDF(H_0)$ as a function of Lambertian order *m* associated with the half-power angle, regarding different values of the ρ parameter.

Figure 3.27 (a), (b), (c) show the CDFs for H_T=0.2m and α=45° and respectively ρ=0.1, 0.5 and 0.9.

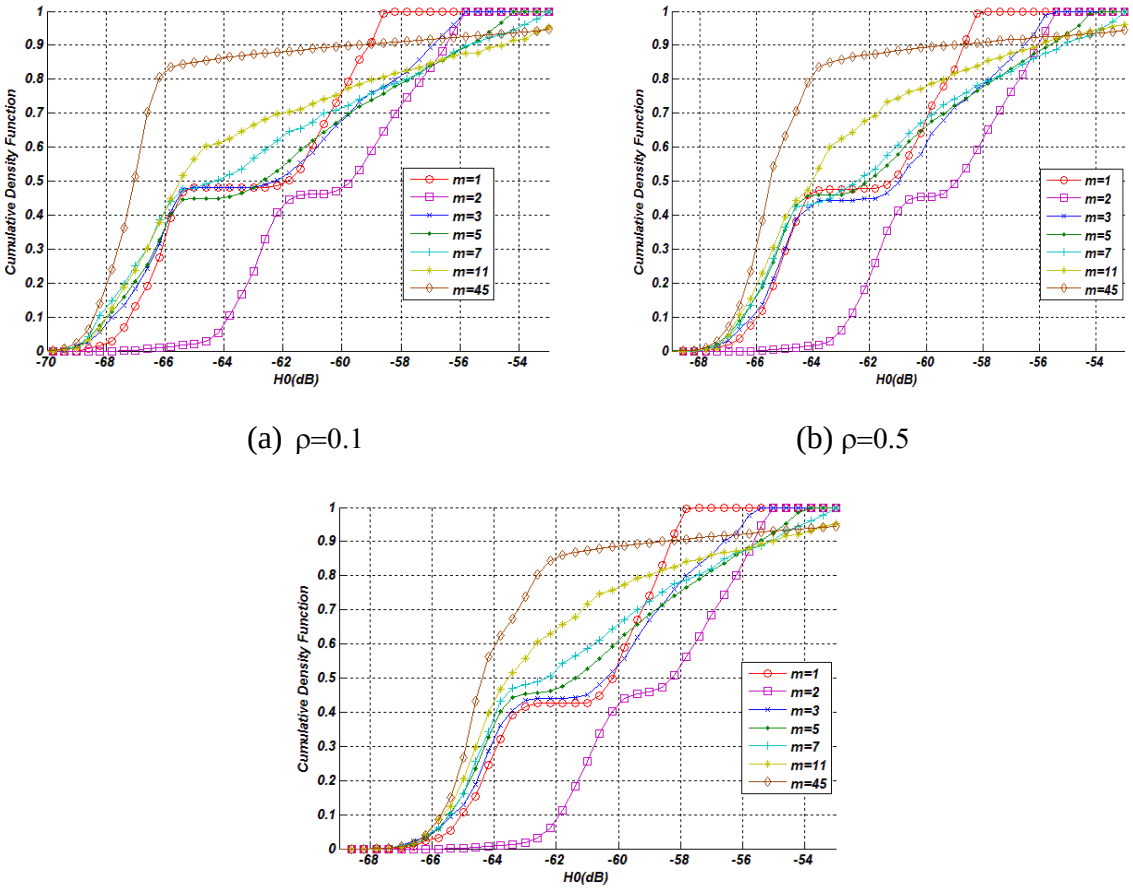

(a) ρ=0.1 (b) ρ=0.5

(c) ρ=0.9

Figure 3.27. $CDF(H_0)$ scenario (b) as a function of *m*; 3D body with (a) ρ=0.1;(b) ρ=0.5 ; (c) ρ=0.9, H_T=0.2m; α=45°

We can conclude that the best value of *m* always equals to 2 whatever the value of ρ. This has been verified whatever the locations of the transmitter and for the angle value α=60°.

III.3.4.4. Rx orientation

Previously, we determined two optimal angles for the orientation of the four receivers at the corners of the LED panel in the studied scenario. These angles were obtained for an empty room.

License CC BY-NC-ND 3.0

In this part, we check if the presence of the body could modify the results.

First, the figures 3.28 (a) and (b) present the CDFs according to the orientations of the receivers (angle α varying between 5° and 90°), in the presence of a body with properties in the average (ρ = 0.5) for two heights of emitters respectively H_T=0.2m and 1.5m.

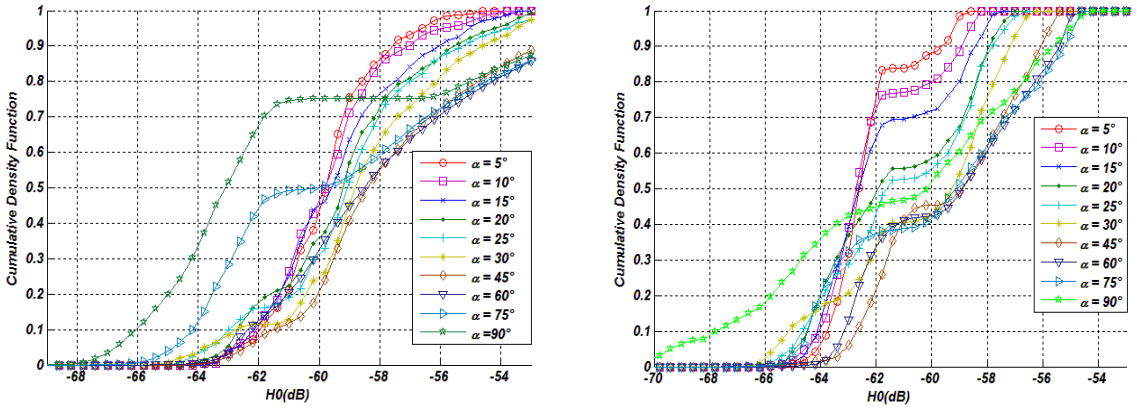

(a) H_T= 1.5m (b) H_T= 0.2m

Figure 3.28. $CDF(H_0)$ scenario (b) as a function of α; 3D body with ρ=0.5; (a): H_T= 1.5m; (b): H_T= 0.2m; *m*=2

We conclude that body presence doesn't modify the conclusion on the optimal angles α. To complete, we have also verified that it is still the same whatever the parameter ρ.

III.3.4.5. Tx Height on the body (H_T)

Following the first results presented in Figure 3.24, we can deduce that the value of ρ has little effect on performance when the sensor is on the shoulder. In contrast, for a position on the ankle, it is necessary to estimate the values of body reflectivity coefficients as precisely as possible.

Here, the study of the channel behavior according to the position of the transmitter on the body is extended by considering the different heights between 0.2m and 1.5m.

We observe in Figure 3.29 that performance deteriorates as the height H_T is small for a body with ρ=0.1. The results show that the presence of the body has a significant impact especially if the transmitter is located at a height less than 1.5m. This seems logical since above 1.5m there is only the head that can cause blockages.

This has been verified whatever the ρ value.

License CC BY-NC-ND 3.0

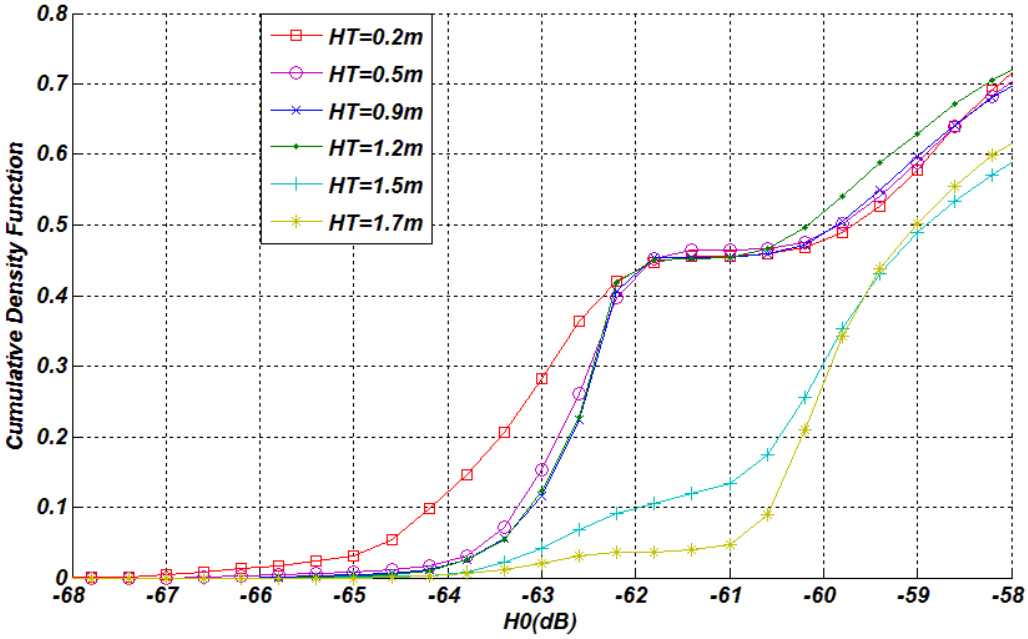

Figure 3.29. $CDF(H_0)$ scenario (b) as a function of H_T; 3D body with ρ=0.1; *m*=2; α=45°

III.3.5. Conclusion on IR Channel

We have proposed an analysis of the IR channel behavior in a context of body sensor thanks to ray-tracing based simulation software named RaPSor. This behavior was studied with regard to the channel gain variations when a patient moving within the environment wears an IR emitter.

We have investigated a link configuration based on spatial diversity (named scenario (b)), where the receivers are included in a unique lighting device like a LED panel, whereas classical approaches consider IR receivers uniformly distributed over the room ceiling (scenario (a)). Our objective was to determine optimal physical and geometrical parameters related to emitters and receivers to ensure the best performance. In addition, thanks to the simulation approach, we have studied the effect of the human body carrying the emitter. A 3D shape has been used to model the body.

The main conclusions are as follows:

- The four receivers included at the corners of the central LED panel have to be oriented with 45° or 60° angles.
- Concerning the transmitter, we have found that the best half-power angle of the source is $\boldsymbol{\varphi_{1/2} = 45°}$ (corresponding to Lambertian order *m*=2). We have verified that

License CC BY-NC-ND 3.0

performance depends on the position of the transmitter on the body, but whatever the position, it is not necessary to take into account variations in emitter orientation angles, so that we consider a perpendicular transmitter. In addition, it is essential to model the body with a reflectivity coefficient value that is as accurate as possible, particularly when the transmitter is close to the floor.

In the following part, we present experiments illustrating the IR channel behavior for the studied scenario.

III.4. Experimental validation

III.4.1. Introduction

In order to validate the theoretical conclusions and investigate the performance of the system, we report experimental results obtained with devices based on low-cost off-the-shelf components and rapid prototyping systems.

First experiments have been realized using systems previously, developed [85,127] based on various IR LEDs and a commercial photodetector including PIN, preamplifier and automatic gain control. In the previous works, the receivers were positioned on the ceiling as in scenario (a). We have developed a new set-up corresponding to the positions of scenario (b), as described in the following paragraph.

In addition, in previous works, the packet error rate (PER) is evaluated from the tag number of each received packet compared to the previous one. However, with this methodology, for a long time of blocked transmission, packet loss is under-evaluated. A new PER evaluation based on time of arrival is described in the following.

Moreover, since we are using integrated off-the-shelf photo-detection modules requiring a 38 kHz sub-carrier for frame detection, this limits the raw data rate range. In order to increase the raw data rates, other photo-detection modules have been investigated, using higher speed components and experimental results are also presented at the end of this part.

III.4.2. Experimental setup description

III.4.2.1. Emitter / receiver hardware description

The basic system transmission is the one developed in previous works [127]. It is designed based on receivers, which are integrated photo-detection modules (TSOP 34338), composed of PIN photo-detector and preamplifier. They are able to detect data frames when the signal is modulated following a subcarrier of 38 kHz with a minimum of 6 cycles per burst.

License CC BY-NC-ND 3.0

The peak wavelength detection is around 940nm. Besides, the receiver has a Field Of View (FOV) of 45° and a typical minimal irradiance of 100µW/m² depending on the ambient noise level, which allows detecting very low power signal. The physical surface of the PIN photodiode is 34.5mm².

The output signal after the photo-detection module is directly connected to a serial input of a microcontroller in order to decode data and analyze it on a computer. This is for evaluating the packet error rate (PER) and plotting the raw data. The serial transmission baud rate is chosen among normalized serial baud rates and must satisfy the fact that we must have at least 6 periods of the modulated signal at 38 kHz inside one useful digit. Consequently, the serial data rate is chosen at 4.8 kbps, which is the maximal one considering the 38 kHz sub-carrier.

With these considerations, the emitter is designed with a microcontroller generating two output signals, one with a PWM signal at 38 kHz, the other one from the serial output at 4.8kbps. The outputs are linked to an electronic circuit making logical operation and driving an infrared LED source around 940 nm. We use two LEDs with different half-power angles 30° and 10° respectively corresponding to m=5 and m=45 (TSAL7600 and TSAL5100). The IR LED is thus modulated with On-Off-Keying (OOK). Taking into account the sub-carrier at 38 kHz imposed by the receiving module, the data rate of the infrared transmission is 76 kbps while the raw data rate is 4.8 kbps.

Finally, in order to be able to decode data at the receiver side and to count errors and lost packets, the frames have to follow a given format, with frame delimiters, packet numbering and redundant information [127]. The chosen format is a 10-byte frame, transmitted each 0.1s. We illustrate the results with 3-axis accelerometer data but any other type of data could be transmitted.

Considering the maximal forward current of the LED with the ratio of transmission time and periodicity of transmission, we designed the circuit to emit an instantaneous optical power of 90mW. Considering the emitting time ratio of 16.7%, and the hypothesis of equiprobable data emission with the OOK modulation, the average IR transmitted power is much lower, around 3.75mW.

III.4.2.2. Scenario description

We have conducted experimental measurements in the room described at the beginning of this chapter as shown in Figure 3.12, with the 4 receivers placed at the corners of a central

License CC BY-NC-ND 3.0

panel (scenario (b)). The receivers can be oriented according to two angles: 45° and 60° thanks to printed pieces as shown in Figure 3.30. The receivers spatially distributed and oriented towards the floor (scenario (a)) are also installed as in previous studies [85,127].

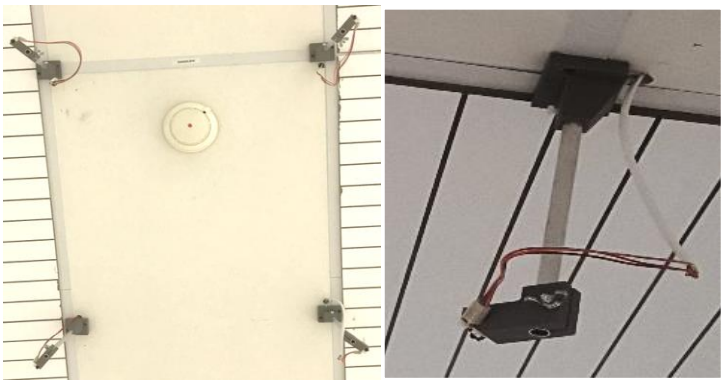

Figure 3.30. Receivers at the central panel, example of printed pieces to fix orientation

Finally, we have 8 receivers (4 for each scenario) placed in the ceiling, each one connected to a Power over Ethernet (PoE) microcontroller. Microcontroller modules are linked to a switch so that we can connect a computer to receive and combine all information.

Figure 3.31 shows the connection between the switch and the Ethernet socket on the wall and a scheme representing the different positions in the studied room regarding the door position. The numbering 30, 31, 32, 33 corresponds to the different positions in the ceiling. The upper connections correspond to the scenario (a) whereas the lower connections (with red markers on the cables) correspond to scenario (b).

This setup permits evaluating performance for various numbers of active receivers by simply connecting to the switch the desired ones. Results with only 2 receivers are obtained for diagonally opposed receivers, i.e. number 30 and 32, or number 31 and 33.

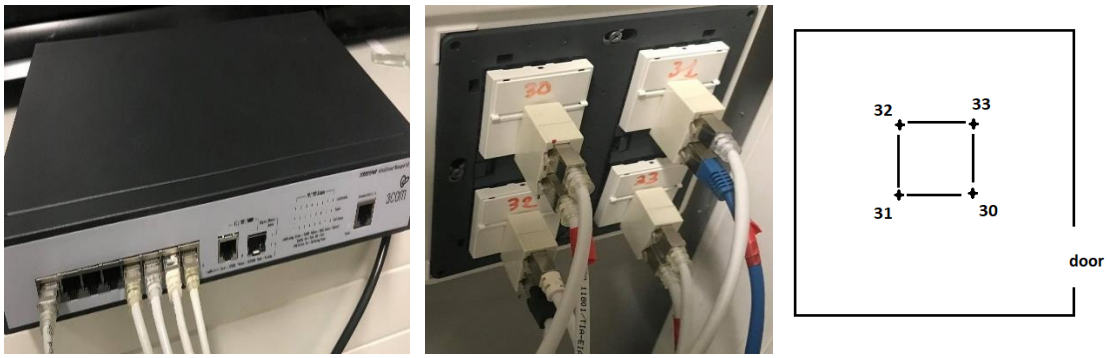

Figure 3.31. Switch connection and positions of receivers in the room with their numbering

License CC BY-NC-ND 3.0

In order to investigate emitter height and body presence impact, we have set up two schemes: one with the transmitter worn by a person (at the ankle or at the arm), another with the transmitter carried by a robotic platform at quite the same height than the ankle position, i.e. 0.2m (illustrated in Figure 3.32).

(a) (b)

Figure 3.32. Experimental setup, (a): sensor attached on the body (b): sensor attached on robotic platform

III.4.2.3. PER determination

PER evaluation is done by a computer receiving all data information from the switch. The algorithm decodes frames of each received signal and detects from the redundant information whether it is correctly decoded or not. The packet number identifying each packet permits treating only once when it is well received by several detectors. Then, the transmission reliability in terms of the percentage of packet loss is experimentally determined:

$$PER = \frac{n_{blost}}{N} \qquad (3.4)$$

n_{blost} is the number of lost packets and N is the total number of emitted packets.

For both scenario (a) and (b), we can evaluate PER with this technique, already implemented in Qt program launched on a computer connected to the switch as in previous works [127]. However, the packet number is counting from 0 to 7. Consequently, if more than 8 consecutive packets are lost, the decoding technique is not able to count them.

For this reason, a new method evaluating errors from time of arrival has been implemented. In this setup, the receivers are connected to a FTDI converter sending by USB the data to a computer where a Python program saves raw data and counts the number of errors.

License CC BY-NC-ND 3.0

For this setup, we don't use the structure presented in Figure 3.30, because we need to modify the Rx connections. Therefore, we have placed four receivers on the top of a structure, oriented with the same pieces as in the first configuration of the central panel as shown in Figure 3.33.

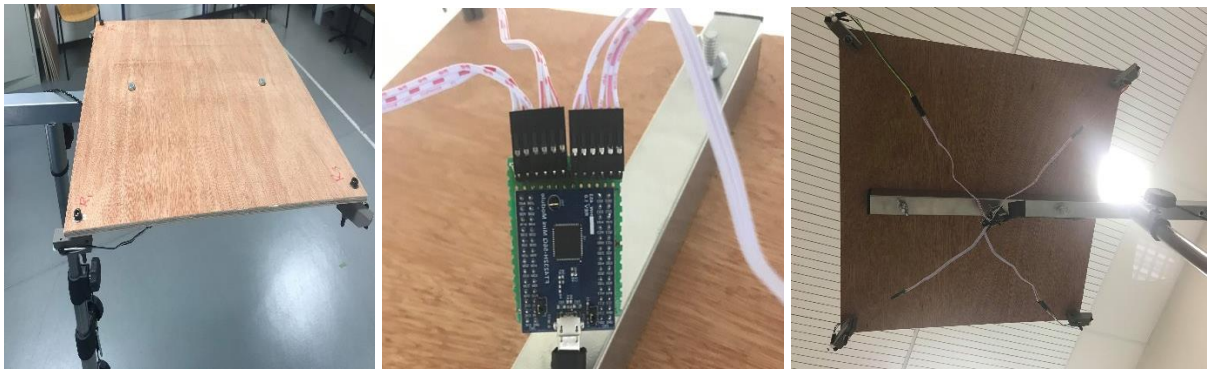

Figure 3.33. Experimental setup with the portable structure with FTDI receiver and Python program

First, the program does the same process of selective combining as in first calculation, i.e. decides from redundant information whether there is an error in received data or if at least one of the receivers correctly received the packet. Then, from the correctly received packets only, the program takes into account the time that has passed between the previous correct packet and the correct one just received. The transmission time of one packet T_T (s) is fixed by the following equation:

$$T_T = \frac{Data\ (bits)}{Baudrate} + T_{delay} \qquad (3.5)$$

With T_{delay} (s) the delay after sending packet information, *Data* corresponds to the number of bits per packet and *Baud rate* is the serial data rate (bps). The T_T value is known at the receiver, used for the counting error process.

Thus, at each received packet number *i*, the following quantity is determined:

$$nb_{lost}^{i} = \frac{(T_{pr}^{(i)} - T_{pr}^{(i-1)} - T_T)}{T_T} \qquad (3.6)$$

Where $T_{pr}^{(i)}$ is the time of arrival of correctly received packet and $T_{pr}^{(i-1)}$the time of arrival of the previous one. Obviously, there are no error when $T_{pr}^{(i)} - T_{pr}^{(i-1)} = T_T$.

License CC BY-NC-ND 3.0

If nb_{lost}^{i} is not null, then it corresponds to the number of errors at this time of arrival. This is done for each received packet. The PER for a transmission with *n* received packets and nb_{lost} packets is expressed as:

$$PER = \frac{n_{blost}}{N} = \frac{n_{blost}}{n+n_{blost}} \qquad (3.7)$$

where $n_{blost} = \sum_{i=1}^{n} nb_{lost}^{i}$ is determined using (3.6).

Results with this method are presented in the last part of following paragraphs.

III.4.3. Results with robotic platform

We present in this section, experimental results without the impact of the user body using a mobile platform of height 0.2m where the transmitter is attached oriented towards the ceiling. The studied configuration is the scenario (b).

Our objective is to validate the results established in III.3.3.2 paragraph when H_T=0.2m, concerning Rx orientation angle at the panel corners and Tx half-power angle.

III.4.3.1. Impact of Rx orientation – m =45

First experiments have been done using a transmitter with a fixed half-power angle of 10° (*m*=45). PER values are plotted in Figure 3.34 as a function of the number of active Rx with different orientation of Rx: 45°, 60°, and 90°.

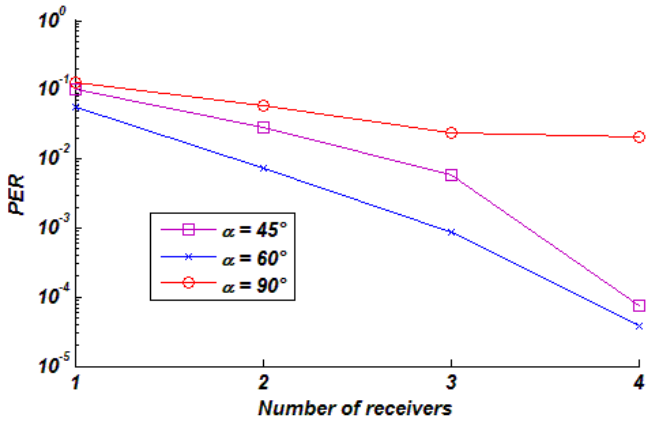

Figure 3.34. Experimental results with different values of Rx orientations, *m*=45; HT=0.2m

From these curves, we verify theoretical behavior obtained from the simulation in the case of the orientation of receivers, i.e. the fact that 45° and 60° are better orientation angles than 90° for scenario (b). In particular, we can observe that the PER results are quasi identical for these two angles when considering 4 receivers.

License CC BY-NC-ND 3.0

III.4.3.2. Impact of Tx half power angle

Here, we have performed experiments for two different Tx half-power angles corresponding to *m*=5 and *m*=45 and with the Rx orientation of 45° and 60°. Results are presented in Figure 3.35 for the different number of active receivers.

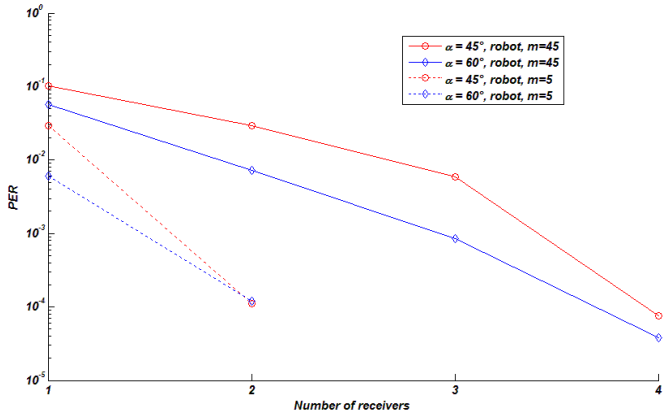

Figure 3.35. Experimental results with different half-power angles *m*=5 and *m*=45, H_T=0.2m

We can note that results with *m*=5 are much better and PER is too small in practice for 3 and 4 receivers to be evaluated (no errors after 10^4 packets sent), so we don't have placed points in the corresponding curve. This result is in accordance with theoretical ones. Having a larger half-power angle without considering body blockages permits lowering errors for a small Tx height.

III.4.4. Results with the human body

In this part, we present results of scenario (b) with the Tx transmitter attached on the body in order to experimentally determine human body impact and verify theoretical conclusions established in III.3.4 section.

III.4.4.1. Impact of Tx half-power angle and height H_T – fixed R_X orientation 45°

We have first made experiments with a person carrying the transmitter. Different locations of the transmitter (at the arm near the shoulder H_T=1.5m and at the ankle H_T=0.2m) have been tested for the two previous half-power angle values m=5 and m=45 with a fixed receivers' orientation of 45°. Results are presented in Figure 3.36.

License CC BY-NC-ND 3.0

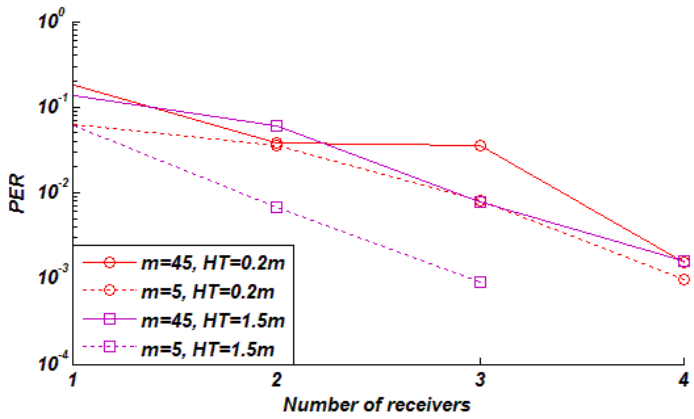

Figure 3.36. Experimental results with human body, different values of H_T, different half-power angles m=5 and m=45, Rx orientation 45°

We remark that for the height of 0.2m, performance is not dependent on half power angle. This illustrates that blockages are important and the signal is strongly attenuated whatever the half-power angle.

Moreover, from this figure, we can verify the theoretical conclusion concerning the fact that channel performance is better when the Tx position is high on the body, with the highest value of the half-power angle (case H_T=1.5m with *m*=5).

III.4.4.2 Impact of the body – comparison with the robotic platform

In order to evaluate the impact of the body, we have plotted in the same figures the results obtained for the case of Tx worn at the ankle (height of 0.2m) and when it is placed on the robotic platform, for the two investigated Rx orientations 45° and 60°. Results are plotted in Figure 3.37 for a Tx half-power angle corresponding to m=45 and in Figure 3.38 for m=5.

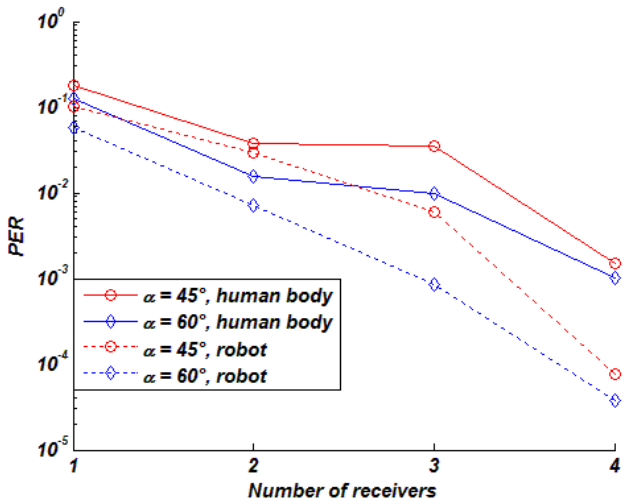

Figure 3.37. Experimental results with Tx worn by a human and the robotic platform, H_T=0.2m, *m*=45

License CC BY-NC-ND 3.0

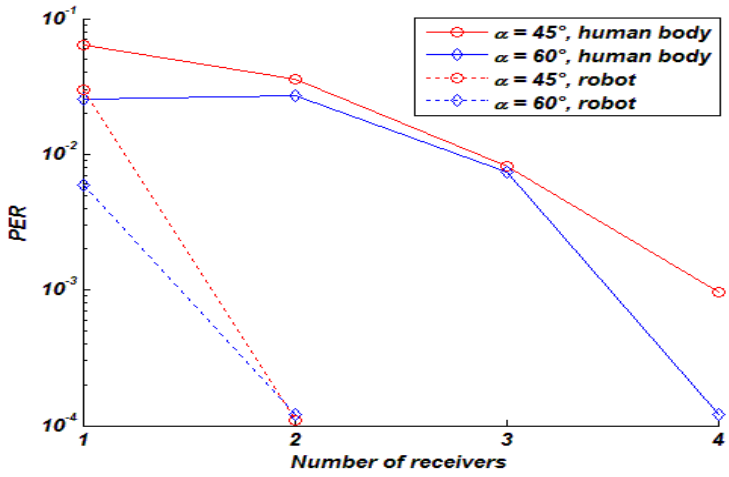

Figure 3.38. Experimental results with Tx worn by a human and the robotic platform, H_T=0.2m, *m*=5

It can be first verified that from 2 active receivers and whatever *m* is, the PER obtained when the transmitter is carried by the platform is lower than when it is placed at the ankle of a person, and thus whatever the receiver orientation angle. Moreover, comparing the differences between the two cases (body and robotic platform), we can point out that the impact of the body is much more important for *m*=5 than in the case *m*=45. This confirms that the body has a strong impact on performance. Therefore, body modeling can be useful when designing the system.

On the other hand, the performance considering body presence is better for *m*=5 than for *m*=45 with 4 Rx. This is in accordance with the theoretical conclusions of paragraph III.3.4.3. Actually, we can note in Figure 3.38 that PER reaches a value near 10^{-4} for *m* = 5 and with 60° orientation for 4 active receivers.

III.4.5. Comparison with scenario (a)

In order to compare both scenarios, we present in the following the results obtained with a mobile transmitter at H_T =1.5m from the floor for receivers orientation 45° and 90° compared to the scenario (a) where the Rx are perpendicular to the ceiling. Figure 3.39 and Figure 3.40 show the results as a function of the number of active receivers, for sources with different half-power angles, respectively m=45 and m=5.

License CC BY-NC-ND 3.0

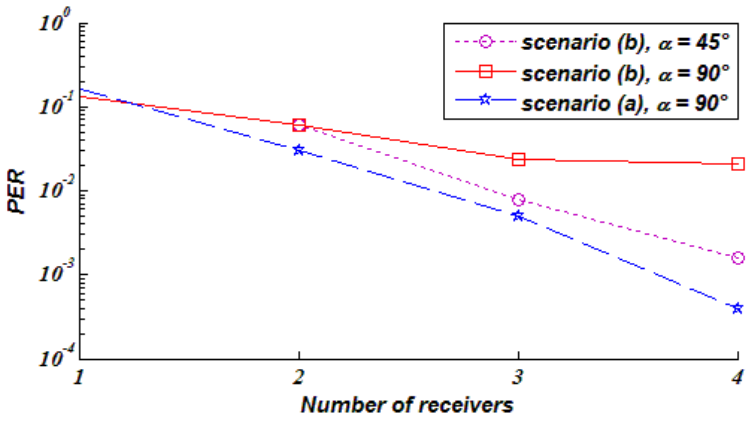

Figure 3.39. Experimental PER for scenario (b) with Rx orientations of 45° and 90° and for scenario (a) with perpendicular receivers; optical source m=45 ($\varphi_{1/2}$=10°).

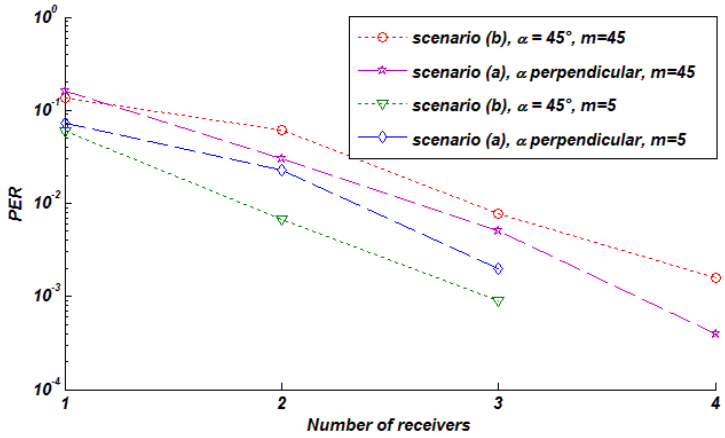

Figure 3.40. Experimental PER for scenario (b) with Rx orientations of 45° and for scenario (a) with perpendicular receivers; optical source m=5 and m=45.

For a directive source (*m*=45) we can note from Figure 3.39 that in scenario (a) where receivers are distributed over the ceiling, PER decreases as the number of receivers increases. More precisely, it is around 10^{-1} for 1 receiver and it is reduced to 4.10^{-4} for 4 receivers. This is obvious due to spatial diversity and in accordance with previous studies [127].

When the receivers are located at the corners of the LED panel (scenario (b)), with an orientation towards the floor (90°), we verify as in the theoretical analysis, that there is no much improvement with the increase of the number of receivers. This is linked to the fact that in this case spatial diversity is not fully exploited.

However, when the orientation is changed to 45°, there is a significant improvement and PER variations are similar to the one of scenario (a). Actually, in this case, we take benefit of the angular diversity.

License CC BY-NC-ND 3.0

From Figure 3.40 as expected, we observe that PER is enhanced when the source is less directive (m=5, $\varphi_{1/2}$ =30°), which confirms the theoretical behavior. For both scenario (a) and (b), the experiments for 4 receivers with *m*=5 result in a PER lower than 10^{-4} (no measured packet loss after 10^4 packets received), so the value is not reported.

Moreover, we notice that PER results are slightly better with scenario (b) compared to scenario (a) for m = 5. This highlights the interest of using a unique and optimized device including 4 Rx in the center of room ceiling (scenario (b)) instead of covering uniformly the ceiling as in the scenario (a).

Finally, these experimental results confirm the previous theoretical conclusions on the choice of the orientation angle of the receivers and on the directivity of the transmitter.

III.4.6. PER evaluation using time of arrival

As explained in part III.4.2.3, PER evaluation is underestimated for long blockage events, more precisely, when at least 8 successive packets are lost. Another method for evaluating PER taking into account both good redundant information and time of arrival have been developed as detailed previously.

For the experiments, a new device has been done (see Figure 3.41), following the same scheme of packet emission as the previous one but allowing modularity, especially, working at higher data rates as explained in the next paragraph. With this device, we are using a fast commutating LED, SFH4346 having a half-power angle of 20° (m=11).

Results are obtained for this device worn at the shoulder, H_T=1.5m and with 45° receiver orientation angle.

We have obtained a PER of 4.2e-4 for 4 receivers and 1.6e-3 for 2 receivers. It is not possible to directly compare with the previous results since they were obtained for m=5 and m=45, but the behavior is coherent. Actually, we can note that for 4 receivers in the same configuration (b), the PER was null for m=5 and near 2e-3 for m=45 (see Figure 3.40) and the result obtained here for m=11 is between these two values. In addition, the behavior with 2 receivers follows the same as previously since the PER is one decade higher, as it was the case with others m values.

License CC BY-NC-ND 3.0

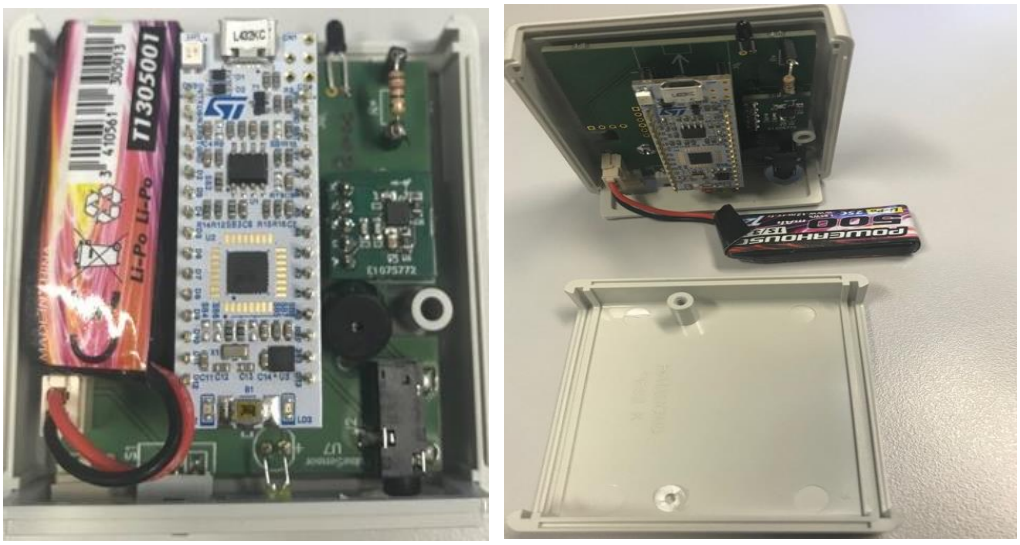

Figure 3.41. New sensor to do the experiment

III.4.7. Results at higher baud rates

As said previously, the new device is able to work at higher data rates, thanks to the fast commutating LED and logical gate having a lower response time. In addition, we have changed the microcontroller unit in order to have a good precision on the clock of the PWM for higher rates than 38 kHz.

We have made experiments with another TSOP receiver (TSOP 7000) working in the same manner as the previous one but with a subcarrier of 455 kHz instead of 38 kHz. In this case, it is possible to increase the raw data rate of transmitted data and to use baud rates from 4.8kbps to 38.4 kbps.

However, the photodiode of this device is not centered in the same wavelength as the previous one, but the sensitivity at 940 nm is 0.8. In addition, one limitation of using this device is the minimal irradiance able to be detected, which is 10 times higher. Therefore, experiments have been conducted with mobility in a smaller area inside the room, with radius 1.78m from the center of the panel.

Results are reported for 4 receivers orientation of 45°, for the device worn at the shoulder, H_T=1.5m in table 3.5 below.

Table 3.5. Experimental PER results versus baud rate

Baud rate (kbps)	4.8	9.6	19.2	38.4
PER	0.17	0.25	0.34	0.47

License CC BY-NC-ND 3.0

We can first note that the PER at the same baud rate of 4.8kbps as previously is significantly increased. This is mainly due to the minimal irradiance to be detected by this receiver which is much higher than the previous one. In addition, PER increases when the baud rate (thus the raw data rate) increases, which is consistent.

Finally, even if the PER obtained here are not satisfying, this experiment is the first experimental approach showing that it is possible to use higher data rates. Results could be enhanced if the receiver is designed with a correct photodiode, amplifier and gain control circuit.

III.5. Conclusion

In this chapter, we have studied the IR uplink channel between a transmitter carried by a moving person and receivers located on the ceiling of the environment.

We first presented the simulation approach and tool for modeling the behavior of the channel. It is software developed by our research team named RaPSor based on MCRT method. We explained how to make a simulation using this software, as well as how to extract the results.

A SISO configuration has been first considered as a basic scenario in the studied environment. This allowed defining simulation parameters, introducing statistical channel analysis based on PDF and CDF of channel gain.

Then we defined two SIMO scenarios that differ according to the distribution of the receivers. The first one (scenario (a)) already explored uses 4 receivers uniformly distributed on the ceiling. In the second (scenario (b)), corresponding to the objective of the thesis, the four receivers are at the corners of a lighting panel in the center of the ceiling. The key parameters to be optimized regarding user mobility are the half-power angle, the height of the transmitter and receiver orientation.

The two scenarios have been first investigated without taking into account the body carrying the transmitter. For both scenarios, the optimal half-power angle of the source is m=2 whatever the transmitter height. The best receiver orientation for scenario (a) is perpendicular to the ceiling, whereas for the scenario (b) it is with angles of 45° or 60° at the corners of the lighting panel. Regarding the transmitter height, the best performance has been obtained for scenario (a) when the transmitter is close to the floor.

However, we have shown that with body modeling the results are different because of body blocking effects. The best performance has been obtained for a transmitter at the highest

License CC BY-NC-ND 3.0

height i.e. far from the floor and the results highlighted the interest of scenario (b) compared to scenario (a).

Thus, the scenario (b) has been more deeply studied regarding the impact of the user body. The conclusions have confirmed the values of optimal orientation angles of the receivers at the panel, i.e. 45° and 60°, in addition to the optimal half-power angle of the source (m=2). Moreover, we have shown that it is not necessary to take into account variations in the transmitter orientations. On the other hand, it is essential to know the optical properties of the body as precisely as possible, especially when the transmitter is close to the ground.

The last part of the Chapter focused on the experimental validation of theoretical conclusions about the behavior of the channel. A setup corresponding to scenario (b) has been realized.

First, we performed tests with a mobile robotic platform to verify the results without the impact of the body. The main conclusions of the theoretical simulation study have been validated, concerning the receiver orientation angles and the half-power angle of the source.

We then presented tests results by carrying the emitters. This showed that the impact of the body is important even more as the source has a wide half-power angle. On the other hand, performance is better with a source that is not a very directive. It can be concluded that it is, therefore, essential to model the presence of the body to determine the IR uplink performances.

This will be done in the last chapter of the thesis for the performance evaluation of the monitoring system. Previously, we will study the downlink visible channel in the following chapter.

License CC BY-NC-ND 3.0

CHAPTER IV. MOBILE VLC CHANNEL BEHAVIOR

IV.1. Introduction

Recall that the objective of this thesis is to study the use of a single device placed on the environment ceiling, allowing both to illuminate the room and to receive infrared transmissions, but also to emit visible data. In this context, this chapter is devoted to the simulation and analysis of the downlink visible channel.

Unlike previous work [85], only one light source is considered here at the center of the ceiling. We study a monitoring scenario where the user can receive data on a receiver worn in front of him as in the case of a smartphone or a tablet. The studied configuration is described in the first paragraph.

We then present the modeling and simulation of the visible downlink channel based on the use of the MCRT approach thanks to RaPSor tool. The parameters affecting the performance of the channel, which is the body of the user carrying the receiver and the movements associated with its mobility, are taken into account and their impact analyzed.

To evaluate the relevance of the proposed model, some experiments based on commercial VLC devices have been performed. The results are presented in the last part before the conclusion.

IV.2. Description of visible downlink configuration

We suppose that the lighting device is in the central position on the ceiling of the same room as previously, of dimensions (6.7×6.6×2.8) m^3. Moreover, it is situated 20cm from the ceiling as in IR scenario (b). The light source is a white LED directed towards the ground, which radiation pattern is a Lambertian corresponding to a half-power angle $\boldsymbol{\varphi_{1/2} = 60°}$ (order m=1). We assume that it is possible to control the brightness of the LED and so perform visible light communications.

The patient randomly moves in the room while holding a device equipped with a VLC receiver (see Figure 4.1). We consider that this device is held at a distance of $\boldsymbol{D_b}$ in front of the body and at a fixed height of $\boldsymbol{H_{T-VLC}}$ from the ground. Patient positions anywhere in the room induce non-directed LOS links related to the optical properties of the environment. In addition, the patient's body can cause blockages or reflections depending on its reflectivity properties. As mobility also implies body movements and consequently receiver orientation variations, we investigate random changes of Rx orientation angles.

License CC BY-NC-ND 3.0

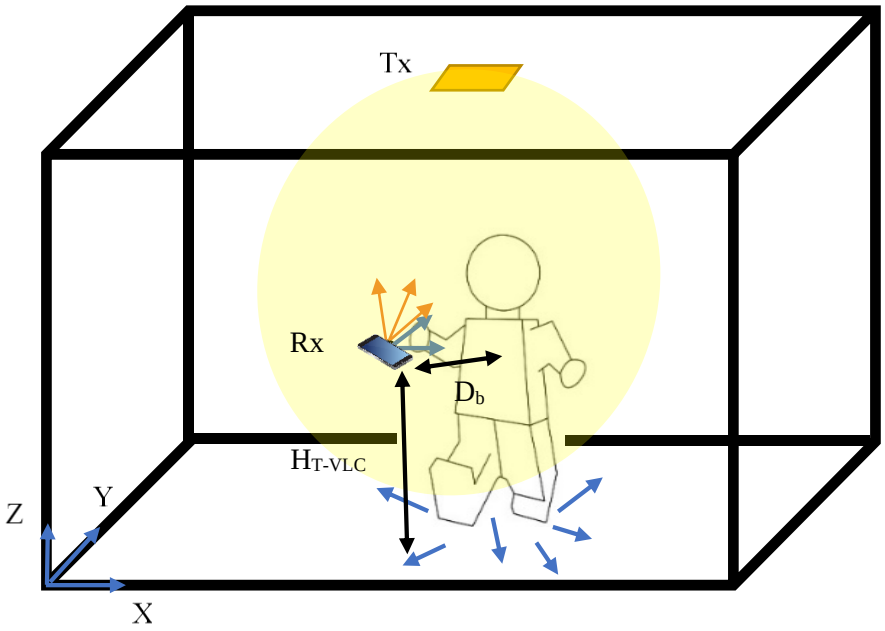

Figure 4.1. Illustration of VLC downlink scenario

In the following paragraph, we present simulation results using RaRSor, regarding the impact of user body, movements, and mobility.

IV.3. Simulation of Visible channel

We consider the same body model as for IR channel i.e. a 3D object characterized by reflectivity coefficient ρ, with a height of 1.8m. The distance H_{T-VLC} from the floor is set to 1.2m, which corresponds to the hand level (see Figure 4.2). Moreover, we suppose a distance $D_b = 20cm$ between the receiver Rx and the user body.

As for IR channel, the ρ values of human body surfaces exposed to light propagation vary according to the light wavelength and the nature of the surface (skin, clothes). Figure 4.3 presents an example of reflectivity coefficients in visible range [132]. In this work, we consider the mean values of the reflectivity coefficient in the visible range. Therefore, to take into account a large range we consider values between ρ=0.1 to 0.9. A weak value represents very absorbing surfaces, while a high value is associated with very shiny ones.

The Rx orientation regarding its normal axis is defined by the polar and azimuthal angles α and φ (see Figures 4.2 and 4.4). These angles can randomly vary to simulate hand user movements. The motion scenario traducing a receiver hold by a patient, it is assumed that the

License CC BY-NC-ND 3.0

Rx can neither be directed toward the ground. However, we supposed that Rx can be oriented towards the ceiling (α=0°). In addition, we consider that the angle α can be tilted up to 60°. Consequently, we investigate the following 3 values of angle: $\alpha \in \left[0; \frac{\pi}{6}; \frac{\pi}{3}\right]$. Moreover, as we suppose that $\varphi \in [0; 2\pi]$ with a step of $\frac{\pi}{6}$, the scenario corresponds to 25 pairs $(\varphi; \alpha)$ of possible angle values.

To model the random mobility of user carrying Rx, we consider a set of Rx coordinates [X Y] randomly and uniformly distributed in the plane at H_{T-VLC}=1.2m.

The simulation parameters for Tx and Rx are listed in Table 4.1. In this chapter, all the physical parameters of transceivers (i.e. Tx half-power angle and radiation pattern, Rx FOV, photodiode physical surface and responsivity) are fixed. We vary the Rx geometrical parameters (2D location and orientation angles) and the reflectivity properties of the user body.

As for IR channel, RaPSor provides the impulse response $h(t)$ for one configuration of (Tx, Rx). From $h(t)$ and according (2.19) we can determine the DC gain H_0 for each link configurations. We consider a random variable H_{0-VLC} taking a value among a set $\{H_0\}$ with a given probability $p(H_{0-VLC} = H_0)$. In the following, we analyze the visible channel behavior by

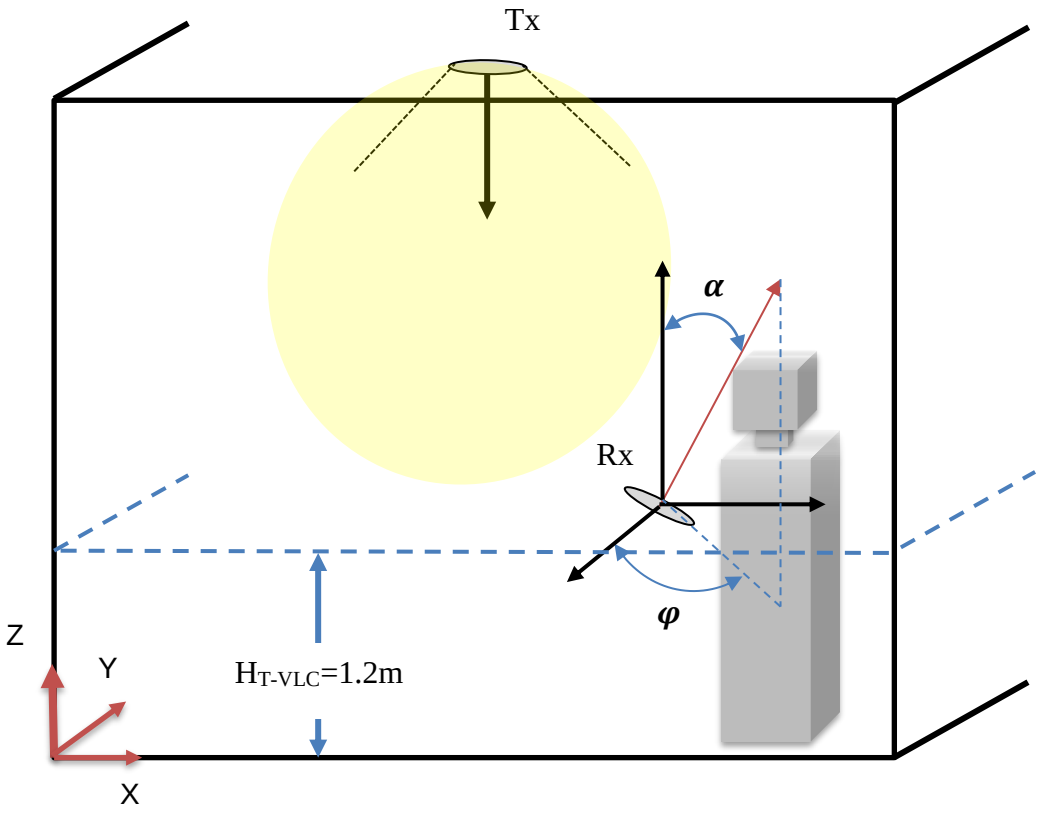

Figure 4.2. VLC downlink definition

License CC BY-NC-ND 3.0

discussing the evolution of $CDF(H_0)$.

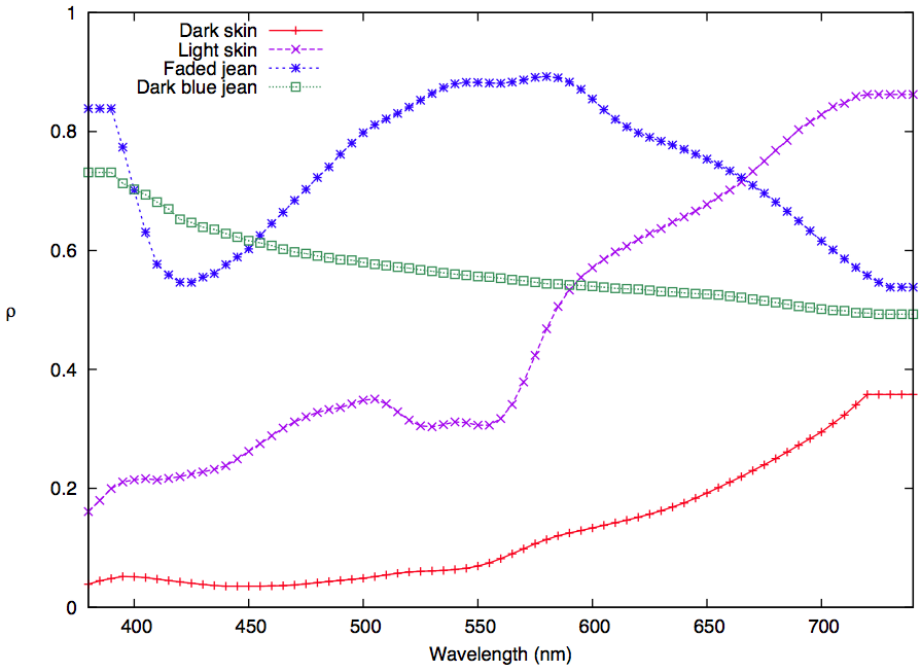

Figure 4.3. Evolution of some body-related ρ according to the light wavelength [132]

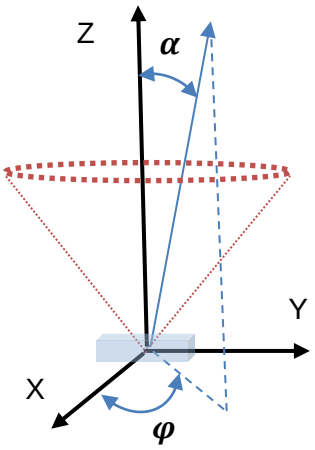

Figure 4.4. Rx orientation changes definition

Table 4.1. Parameters for VLC downlink channel simulation

Parameter	Values
Transmitter Tx	
Number of transmitters	1
Tx orientation angle β (°)	0
Tx Lambertian order m	1

License CC BY-NC-ND 3.0

Tx coordinates [XYZ] (m)	[3.3 3.35 2.8]
Receiver Rx	
Rx coordinates [XYZ] (m)	[XY] variable at $H_{T-VLC} = 1.2$m from the floor Distance from the body D_b=20cm
Rx orientation angles (φ;α) (°)	Variable $\alpha = 0°;\ \alpha \in \left[\frac{\pi}{6};\frac{\pi}{3}\right]$ $\varphi \in [0; 2\pi]$ with a step of $\frac{\pi}{6}$.
Physical active area A_r (m²)	10^{-4}
Field of View FOV (°)	65
Number of receivers	1
Responsivity (A/W)	1
Environment	
Dimensions	6.7*6.6*3 m
Number of optical reflections *k*	3
Reflectivity coefficient of surfaces	0.8
Objects inside the room	3D body defined in Figure 3.20 characterized by reflectivity coefficient ρ

IV.3.1. Impact of body

Firstly, we investigate the effect of body presence considering that Rx orientation is perpendicular (α=φ=0°). We have reported in Figure 4.5 the evolution of $CDF(H_0)$ for the random 2D position of receiver in the room. The simulation has been realized considering the cases without body and with 3D and 2D blocking body model (ρ=0.1).

We observe that body presence even with high blocking optical property has a quite small impact on the channel behavior. This is because Rx is located at 20cm from the body and is always directed towards the ceiling so that the beam collection is not so much affected.

Moreover, we notice that 2D and 3D body models lead to the same results. This means that this is the surface in front of the Rx, which is the most impacting.

License CC BY-NC-ND 3.0

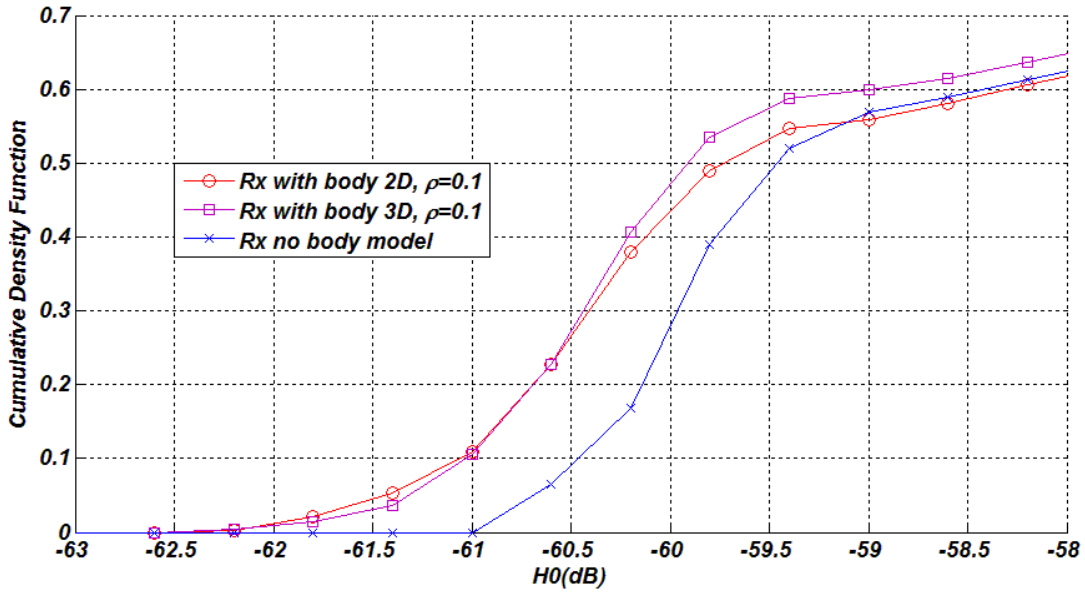

Figure 4.5. Visible channel $CDF(H_0)$; case no body and 3D body with ρ=0.1; α=φ=0°

IV.3.2. Impact of Rx orientation

Here, we consider orientation angle changes as defined previously in Table 4.1. We investigate Rx orientation impact whether body or not. The results are shown in Figure 4.6 where we have added two more curves corresponding to the cases where Rx is perpendicular.

We observe that visible channel is highly impacted when considering body along with random Rx orientation changes. Indeed, in this case, some optical rays cannot be collected by the photodetector FOV when the angle α is too high. In addition, the body can attenuate them. Consequently, for visible downlink channel characterization, it is important to model body presence along with the random orientation of Rx.

To complete these results, we investigate the impact of the body reflectivity ρ. The $CDF(H_0)$ evolution is plotted in Figure 4.7 for three different values of body reflectivity ρ: 0.1; 0.5 and 0.9.

License CC BY-NC-ND 3.0

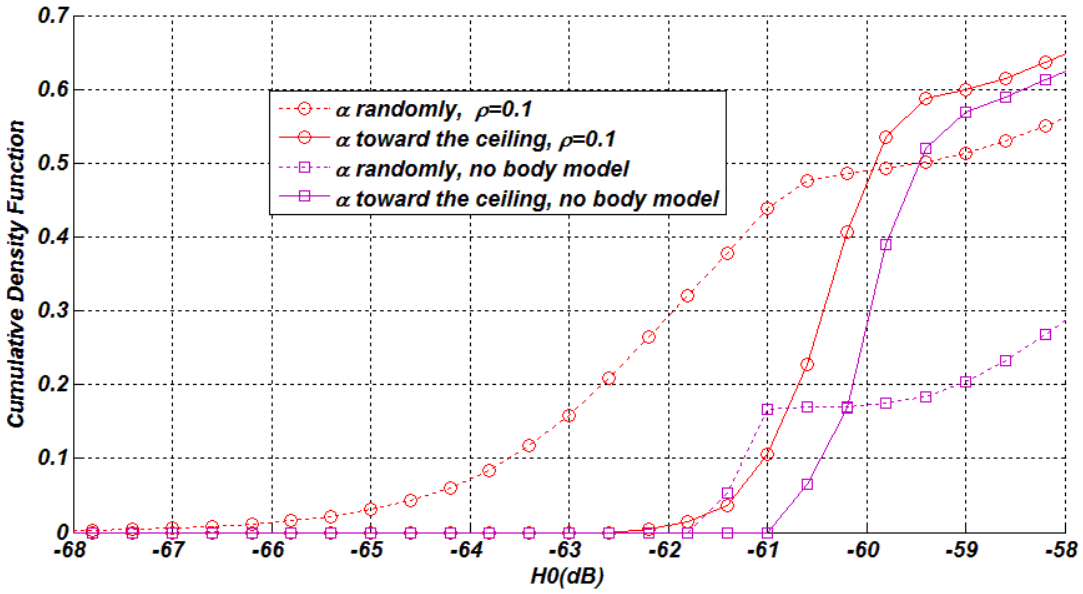

Figure 4.6. Visible channel $CDF(H_0)$; case no body and 3D body with ρ=0.1; random values of Rx orientation angles (φ; α)

As expected DC gain is degraded when ρ diminishes. We note a difference of 4dB on the DC gain value when ρ varies from 0.1 to 0.9. Thus, it is also important to take into account body reflectivity properties in order to well-estimating performance.

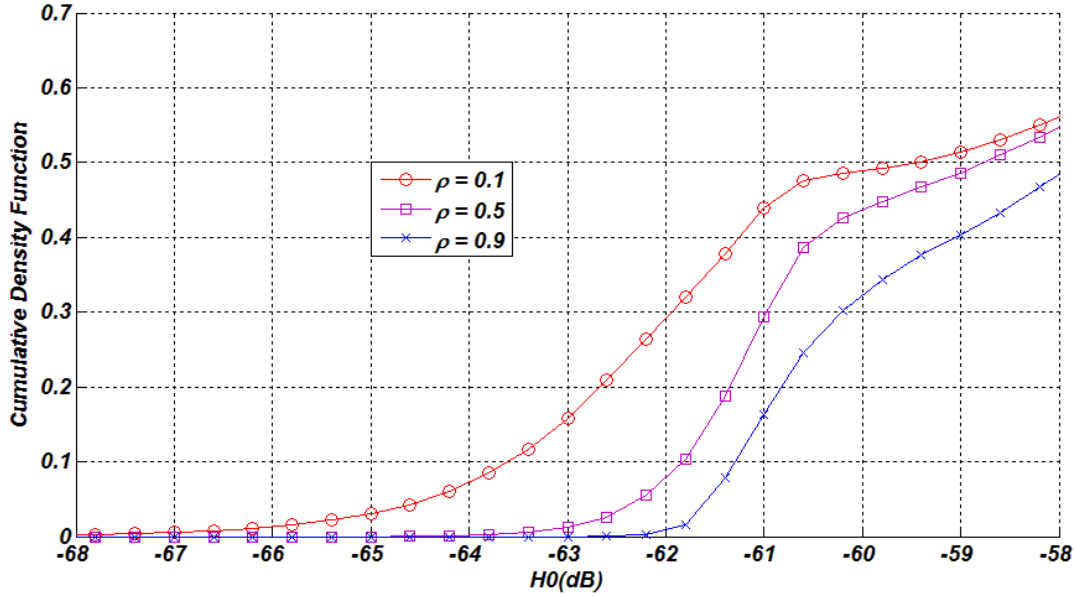

Figure 4.7. Visible channel $CDF(H_0)$; 3D body with ρ=0.1; 0.5; 0.9; random values of Rx orientation angles (φ;α)

License CC BY-NC-ND 3.0

IV.3.3. Impact of distance to body

The previous results have been obtained considering that the receiver is at a distance $\boldsymbol{D_b = 20\ cm}$ in front of the body.

Figure 4.8 shows that if the distance diminishes (10 cm) or increases (until 40cm) the $\boldsymbol{CDF(H_0)}$ evolution is unchanged. Consequently, we will study in the following a scenario with a distance of 20cm.

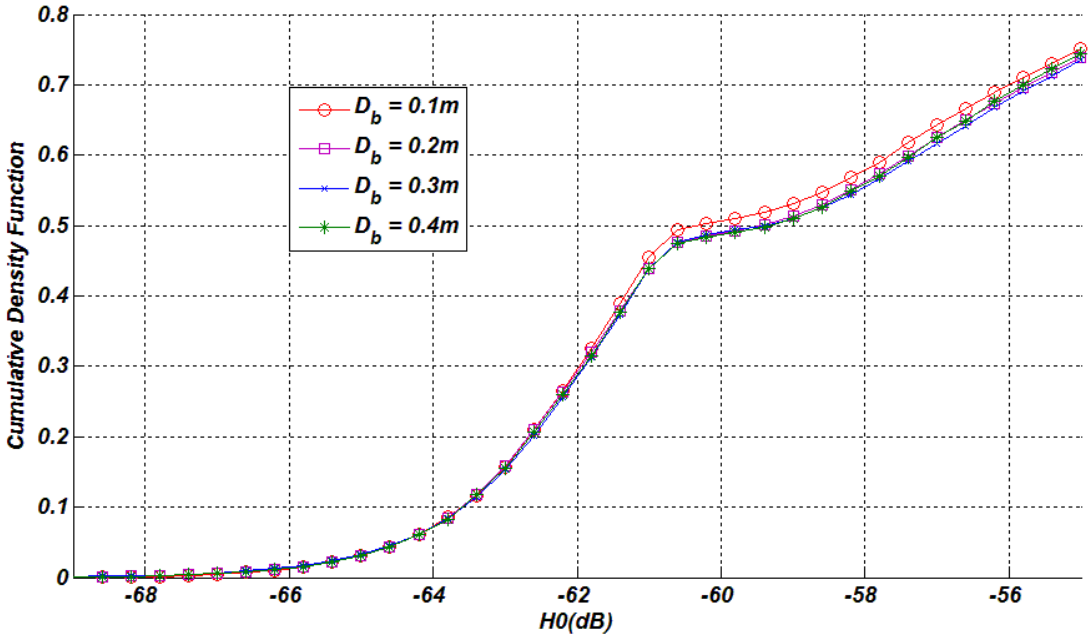

Figure 4.8. Visible channel $\boldsymbol{CDF(H_0)}$ as a function of distance to the body D_b; 3D body with ρ=0.1; random values of Rx orientation angles (φ; α)

IV.3.4. Comparison of VLC and IR channel behavior

Figure 4.9 compares the IR uplink and VLC downlink behaviors in terms of PDF, considering the extreme case for IR channel i.e. a sensor positioned at the ankle. We have set the IR channel parameters of scenario (b) to the best ones obtained in Chapter 3 that is Rx orientation angle of 45° and 60° and Tx Lambertian order m=2.

License CC BY-NC-ND 3.0

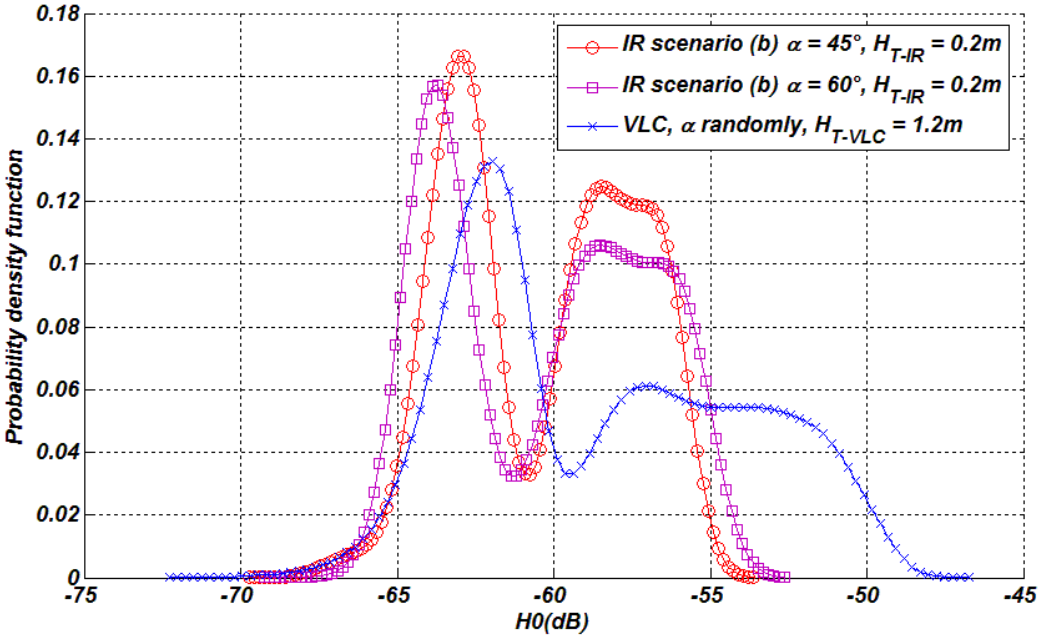

Figure 4.9. IR scenario (b) and Visible channel $PDF(H_0)$; 3D body with ρ=0.1; $H_{T\text{-}VLC}$=1.2m; $H_{T\text{-}IR}$=0.2m

We observe that DC gain spreading is different between IR and VLC channels. More precisely, the optical gain values for IR channel, respectively VLC channel, are between [-69dB; -52dB], respectively [-72dB; -46dB]. Indeed considering the VLC emitter position at the center of the room, there are few LOS link cases for VLC, all within a small area compared to the size of the environment. This explains the very low values of $PDF(H_0)$ of around -72dB. Nevertheless, when the VLC receiver is located under the lighting device, the optical gain is maximal, that corresponds to the few high values of $PDF(H_0)$.

To expand our observation, we have plotted in Figure 4.10 the CDF for the three previous cases. We can clearly see the VLC link behavior compared to the IR one. Indeed, we observe that in terms of channel attenuation, the IR uplink highly overcomes the VLC downlink and this for each IR receiver orientation (45°or 60°). However, it is important to highlight that both links may be used with different constraints regarding emitted power, ambient noise or data rates.

In the next chapter, we will investigate the global performance of the dual link IR/VLC according to the specific power and data rate in order to achieve a fixed quality of service for monitoring application.

License CC BY-NC-ND 3.0

Before concluding this chapter, we present some experimental results with VLC downlink scenario.

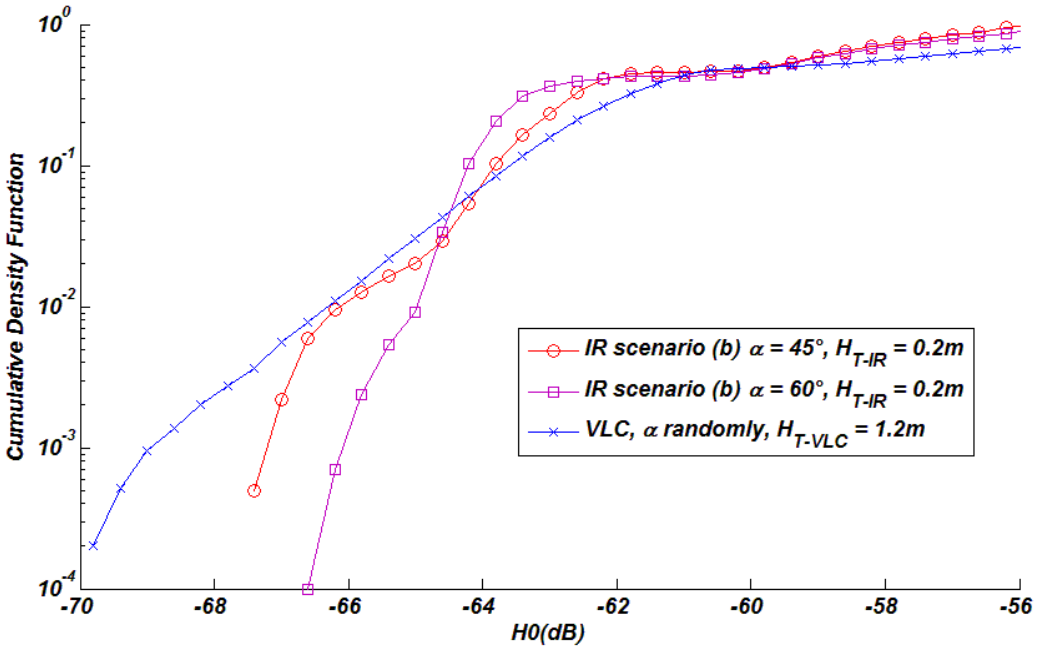

Figure 4.10. IR scenario (b) and Visible channel $CDF(H_0)$; 3D body with ρ=0.1; $H_{T\text{-}VLC}$=1.2m; $H_{T\text{-}IR}$=0.2m

IV.4. Experiments

From the theoretical analysis of visible downlink channel, taking into account body presence along with receiver orientations variations, are key points for the determination of performance.

The experiments we have performed, contribute to validate this conclusion. They have been realized using commercial VLC modules.

IV.4.1. Setup description

We use a VLC luminaire associated with a LiFi dongle, provided by PureLiFi [44] and presented in Figure 4.11.

License CC BY-NC-ND 3.0

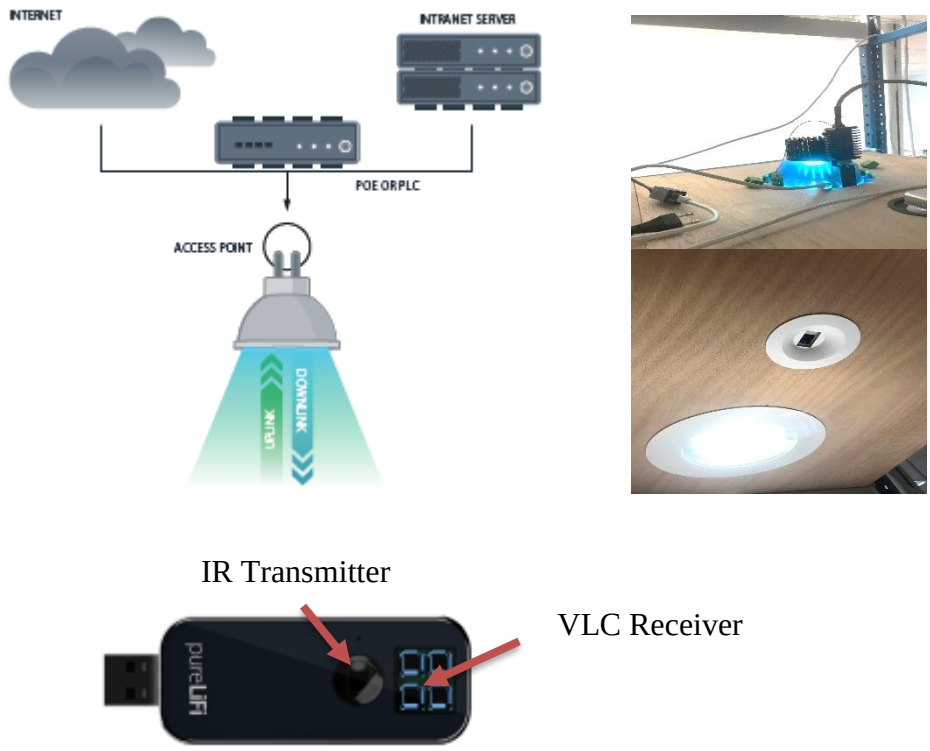

Figure 4.11. VLC luminaire and LiFi dongle from starter kit of PureLiFi [44]

Our objective is to measure the visible power received at the same position than the dongle during LiFi network traffic. This allows evaluating visible link behavior related to body presence and for different orientations of the VLC receiver.

For this purpose, we first defined a Li-Fi network as illustrated in Figure 4.12. The luminaire (access point AP) connected to the PoE module has been included on the ceiling of a box we have constructed with dimensions of (0.6×0.6×1.8) m^3. The PoE module provides power to luminaire and connects this latter to the network.

At the receiver end, we use a Raspberry Pi3 (RPi3) on which the Pure-Li-fi dongle (client) is connected to provide an interface. The native RJ45 interface of the RPi3 is connected to the control network.

To measure visible power at the location of the dongle, we use an integrating sphere power sensor (S140C Thorlabs) with silicon detector designed to measure the optical power of an incoming beam (wavelength range of 350 nm to 1100 nm) independent of the divergence and beam shape. The sensor is in the same position as the dongle and with the same orientation. They are both attached on a device allowing the orientation control as illustrated in Figure 4.13.

In addition, the S140C is connected to a power meter display unit (PM100USB).

License CC BY-NC-ND 3.0

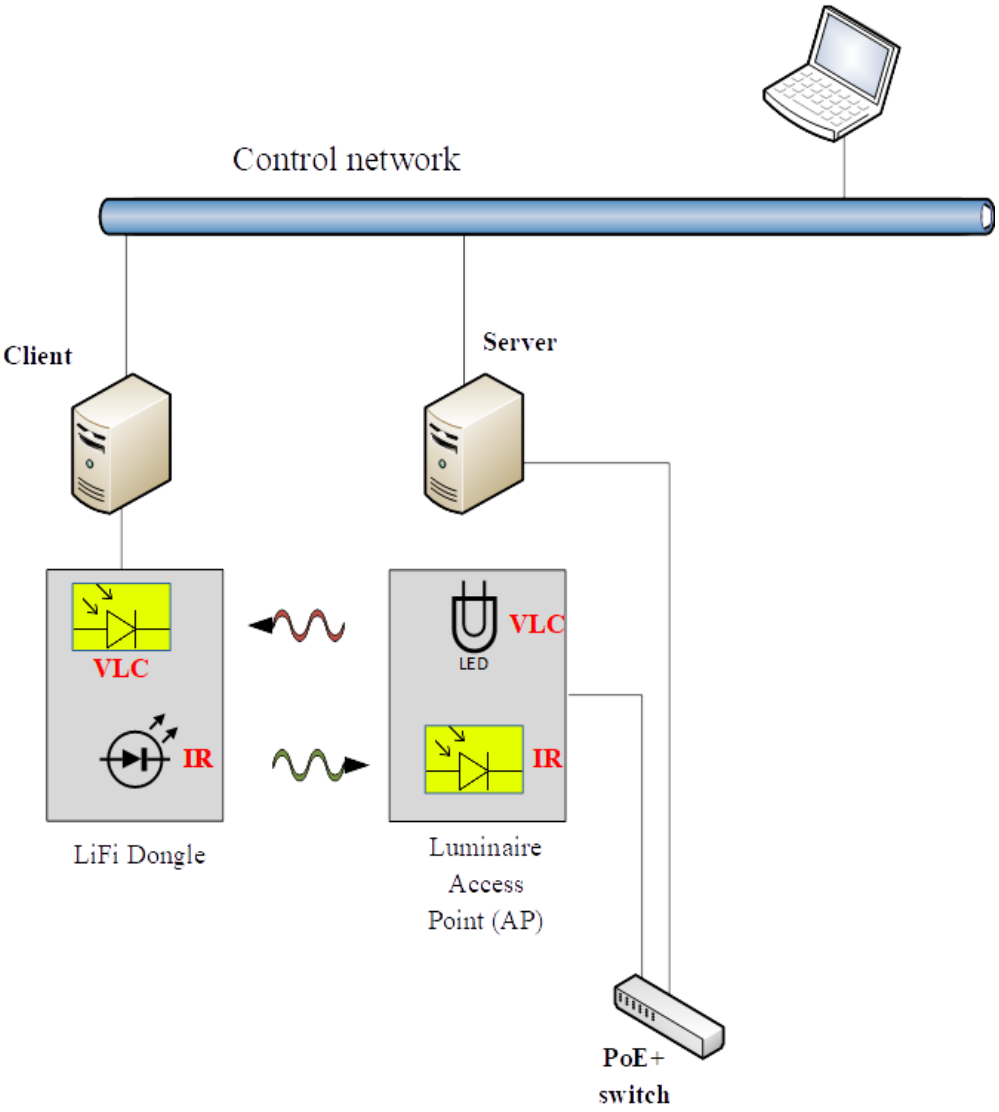

Figure 4.12. LiFi network

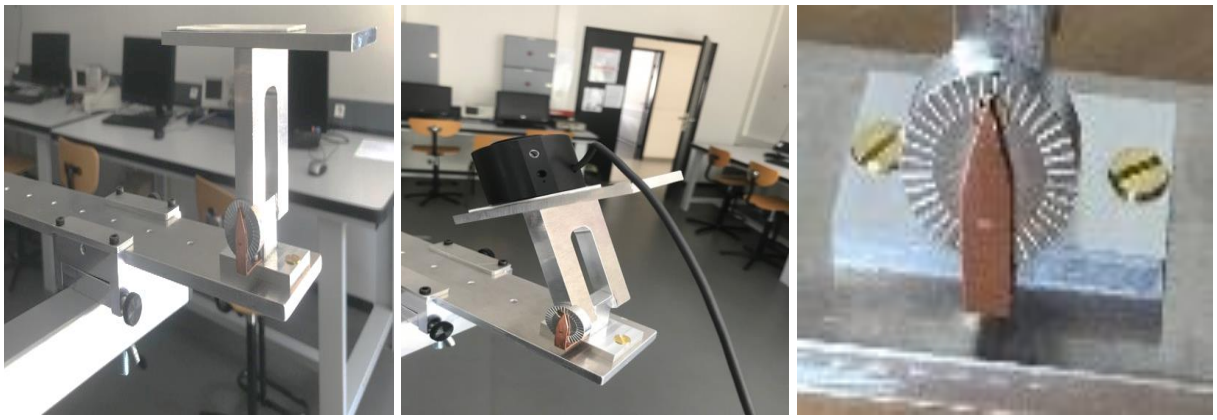

Figure 4.13. Photos of device for the control of receiver orientation

License CC BY-NC-ND 3.0

IV.4.2. Experimental results

We have first measured received power at 400 nm according to the receiver orientation and the presence of the body in front of the dongle as shown in Figure 4.14.

The receiver is positioned at coordinates [XYZ] = [0.1 0.3 1.2] m and the orientation angle α varies between 0° (perpendicular) and 70° in the [YZ] plane.

Figure 4.15 shows the experimental received power measured at 400nm without and with body presence. As expected, the received power is attenuated when the body is in front of the device. In addition, the power decreases as the angle increases. From about 40 ° the attenuation is very strong because the Rx FOV collects almost no more rays. However, this behavior is unchanged whether body or not.

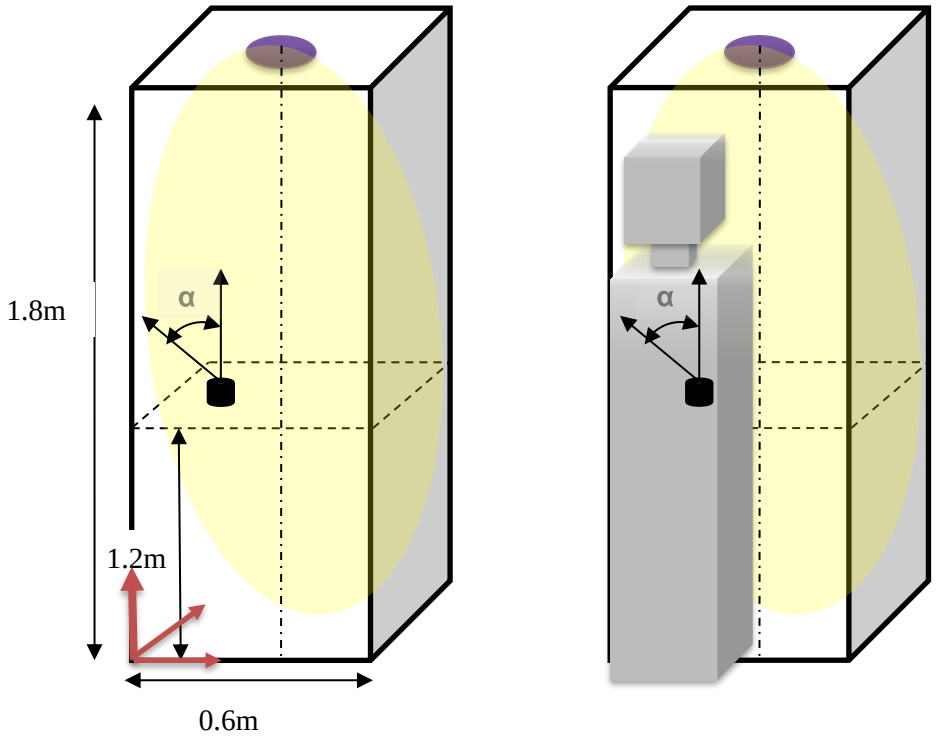

Figure 4.14. Illustration of experiment protocol

License CC BY-NC-ND 3.0

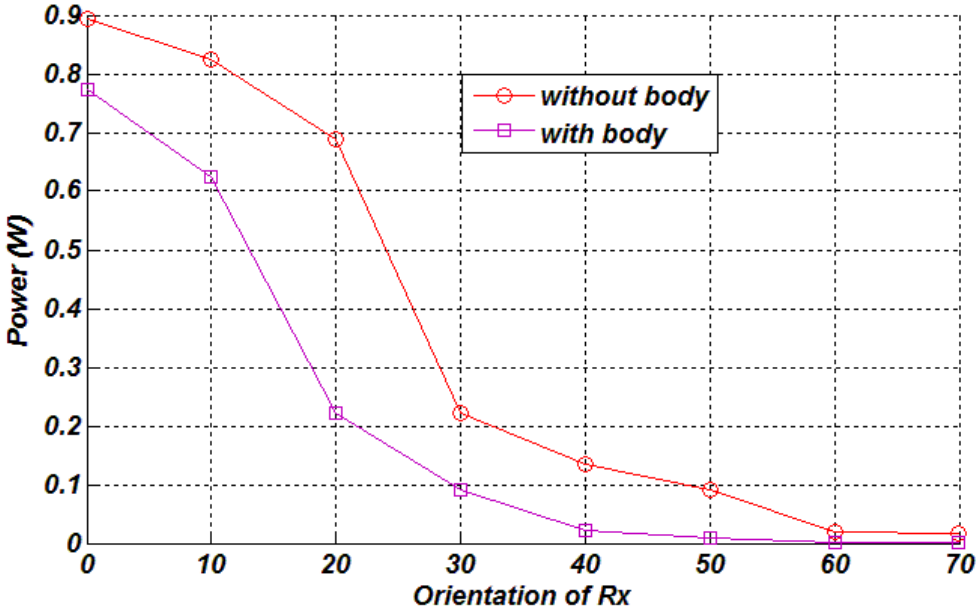

Figure 4.15. Received power at 400nm without and with body presence

On the other hand, we have determined by simulation the DC gain value of the configuration described in Figure 4.14 according to the Rx orientation angle. The transceiver physical parameters are those used in the previous study, reported in Table 4.1. The reflectivity coefficient of the body has been set to 0.1.

The results are shown in Figure 4.16. We note that the DC gain decreases as a function of orientation angle and that the behavior is the same whether body presence or not.

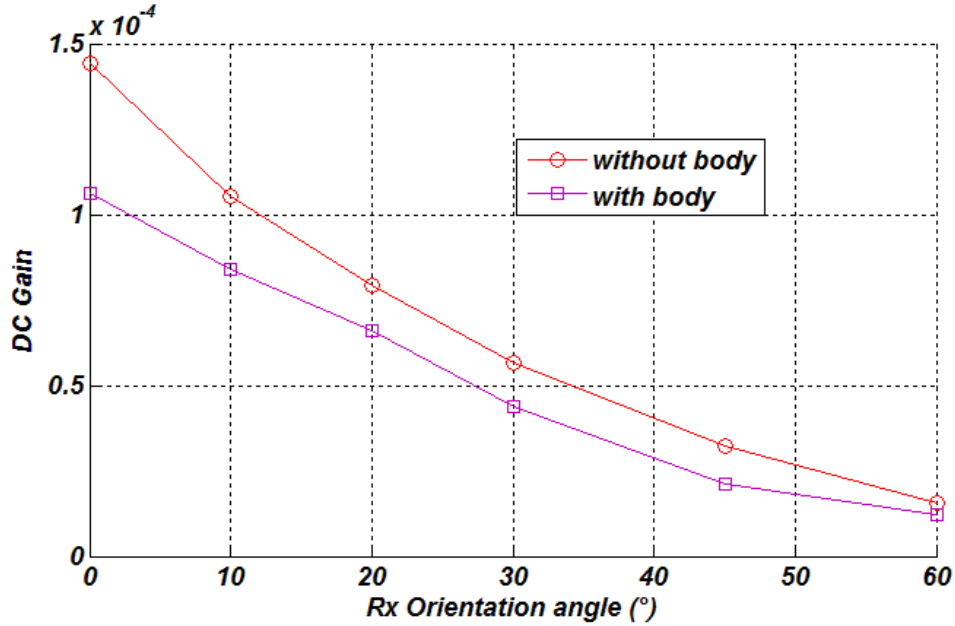

Figure 4.16. DC gain of visible channel without and with body presence

License CC BY-NC-ND 3.0

We can conclude that experiments confirm the simulation results obtained using our channel model.

Experiments have been conducted for the same configuration, at different wavelengths in the visible range. The results are shown in Figure 4.17 and confirm the observed behavior.

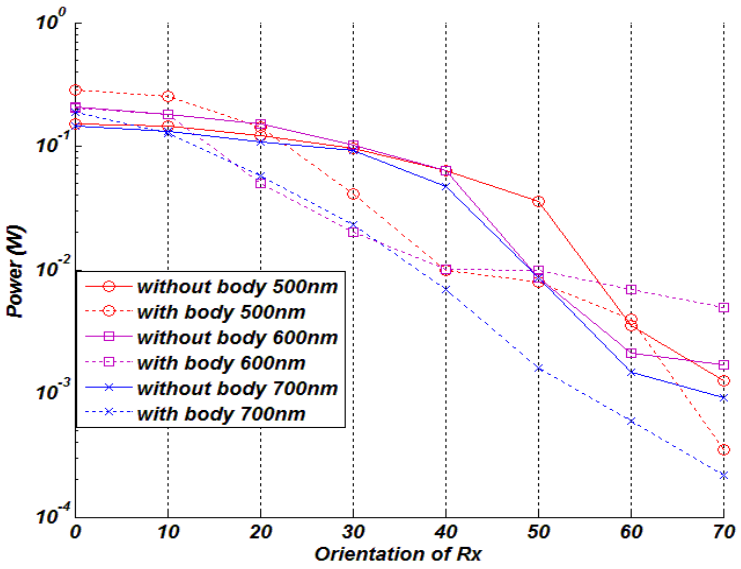

Figure 4.17. Received power at 500nm, 600nm and 700nm without and with body presence

Finally, we have also investigated received power at different positions of the dongle and the power sensor in the plane at 1.2m from the floor. As an example, we present in Figure 4.18 (a) and (b) the results obtained at 500nm without and with the body in front of the devices.

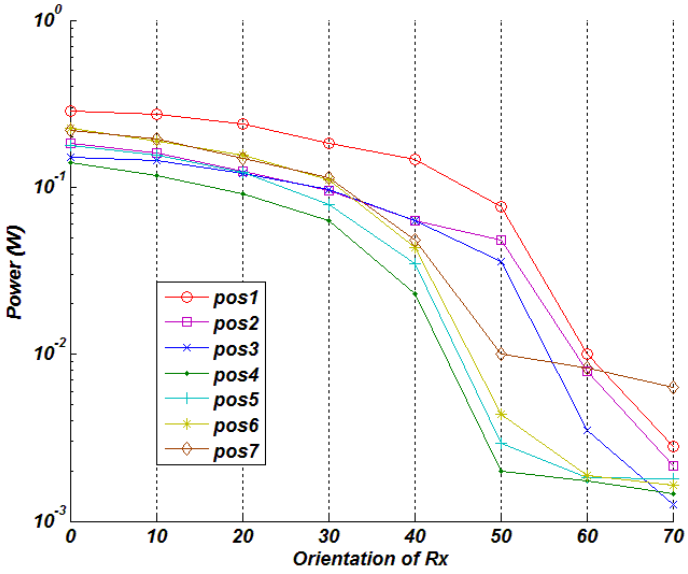

(a) Without body

License CC BY-NC-ND 3.0

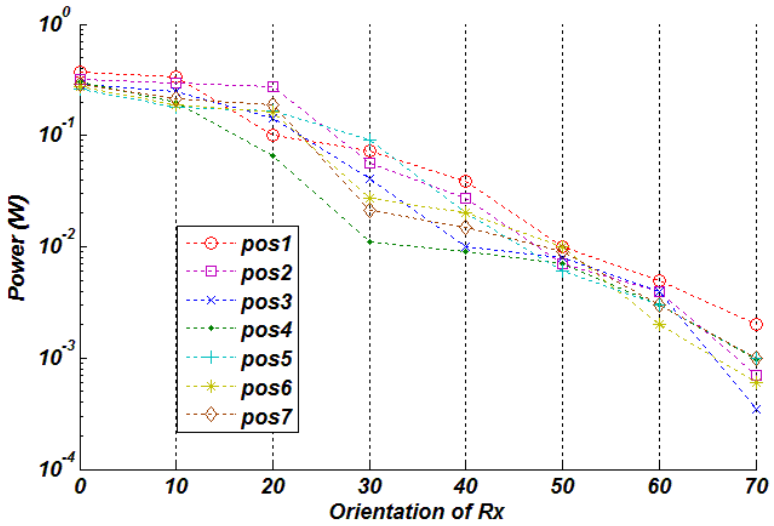

(b) With body

Figure 4.18. Received power at 500nm at different Rx locations without (a) and with (b) body

The results show that body and Rx orientation affect the received power and thus that it is important to take into account this impact to estimate performance.

IV.5. Conclusion

In this chapter, we considered the same environment as in Chapter III where a patient moves randomly. The objective here was to study the downlink transmission channel between a centrally located LED lighting on the ceiling and a receiver brought to a given position in front of the patient.

The approach was based on the MCRT method including 3D modeling of the patient's body as before. On the other hand, we verified that the preponderant element is the surface in front of the receiver as well as its reflectivity properties.

We also simulated and underlined in the case of the visible channel the significant impact of the changes of orientations of the receiver, related to the mobility of the patient, contrary to the case of the infrared channel. This effect has been confirmed by some experiments with commercially available LiFi products.

License CC BY-NC-ND 3.0

Besides, we found that the distance between the receiver and the body had almost no effect on the channel behavior when it is considered that the receiver is carried at the hand.

Consequently, in order to evaluate the overall performance of a bidirectional infrared-visible link, we will use the channel simulation results obtained by considering both the presence of the body, its reflectivity coefficient and the random variations of the VLC receiver orientation.

License CC BY-NC-ND 3.0

License CC BY-NC-ND 3.0

CHAPTER V. BODY SENSOR-BASED MONITORING SYSTEM PERFORMANCE

V.1. Introduction

The objective of the thesis consists in exploring the performance of both IR and visible technologies for sensor-based health monitoring. The main issues are related to the optical technology robustness regarding user body presence and moving.

In previous chapters, we have studied IR uplink and visible downlink behaviors thanks to the MCRT simulation approach, allowing taking into account these challenges. In particular, the results of theoretical analysis have shown that it is essential to model the user body for both links, especially when the sensor is worn at a position below the knee.

In addition, we also have investigated a new scenario for IR and visible transceivers that can facilitate design and deployment. In this configuration, IR receivers and visible source are in the same device, which is a central lighting panel as illustrated in Figure 5.1. The optimal physical and geometrical parameters of IR and visible transceivers have been determined from the theoretical studies, supported by experiments carried out for each link.

Figure 5.1. Illustration of body sensor-based monitoring system.

In this chapter, we use the previously established channel gain statistical distributions to evaluate the performance of each link in terms of link failure. This concerns the IR link between sensor and fixture and visible link between the luminaire and the worn receiver. Considering a

License CC BY-NC-ND 3.0

given noise level, the probability of failure is related to power and data rate. We first assume a given data rate corresponding to the classical requirement for medical monitoring and focus on power to discuss performance.

Then, we study the overall performance of the total link between the worn sensor and the receiver also worn. Considering a given quality of service corresponding to medical constraints and for OOK modulation, we address power and data rate trade-offs of both technologies used regarding body impact.

V.2. IR uplink performance

We study in this part the performance of scenario (b) defined in chapter III in (6.7×6.6×3) m^3 room.

Based on theoretical conclusions, the orientation angles α of the receivers at the central panel are set to the best values: 45° and 60°. In addition, the half-power angle of the Lambertian IR source is set to $\boldsymbol{\varphi_{1/2} = 45°}$ (m=2) and the emitter is supposed to be oriented toward the ceiling (β=0°).

The IR channel gain $\boldsymbol{H(0)}$ follows a statistical distribution related to random (X Y) coordinates of the transmitter worn on the body and supposed to be at a given height $\boldsymbol{H_{T-IR}}$ from the floor. The body is modeled by a 3D object. A reflectivity coefficient between 0.1 and 0.9 is affected by body surfaces whereas all the environment surfaces are characterized by the reflectivity coefficient of 0.8.

V.2.1. Definitions

Linked to the channel gain $H(0)$ and depending on the system modulation, the Signal to Noise Ratio (SNR) is a key metric used to evaluate performance, taking into account emitter power and noise contribution. The performance at bit rate R_b is related to the received electrical SNR of the equivalent baseband channel:

$$SNR = \frac{R^2 P_r^2}{N_0 R_b} = \frac{R^2 H(0)^2 P_t^2}{N_0 R_b} \qquad (5.1)$$

R is the responsivity of the photo-detector; P_r respectively P_t is the average received respectively transmitted power; N_0 is the double-side spectral density of noise assumed to be an Additive White Gaussian Noise (AWGN).

We have seen in paragraph II.5 that a classical assumption is to consider:

$$N_0 \approx 2qI_B \qquad (5.2)$$

With $I_{BIR} = 200\mu A$ for the IR channel.

License CC BY-NC-ND 3.0

Based on SNR, the Bit Error Rate (BER) is classically used to discuss the performance of modulation schemes. For example for OOK and M-PPM, it is given by:

$$BER_{OOK} = \frac{1}{2} erfc(\sqrt{\frac{SNR}{2}}) \quad (5.3)$$

$$BER_{M-PPM} = \frac{1}{2} erfc(\frac{\sqrt{M.log_2 M.SNR}}{2}) \quad (5.4)$$

However, in our scenario, the channel gain $H(0)$ follows a statistical distribution because of the patient moving within the environment. Consequently, SNR also randomly varies. Therefore, the system BER varies according to the patient's position and the movements of the IR transmitter.

To account for these variations, we use a metric based on the probability of meeting a given performance in terms of BER.

A given performance corresponds to an SNR limit value called SNR_0. As an example, if the targeted BER is around 10^{-9} which corresponds to medical requirements [82], this means that limit SNR for OOK modulation is $SNR_0 = 15.6$dB. If the SNR is smaller than SNR_0 the targeted performance cannot be reached and the system is an outage.

Therefore, we discuss link performance considering the outage probability P_{out} expressed as:

$$P_{out} = p(SNR < SNR_0) \quad (5.5)$$

The quality of the link will be better if the probability P_{out} is low for a given SNR_0.

V.2.2. Performance analysis

In this part, we consider a given data rate $\boldsymbol{R_b = 1Mbps}$ to illustrate performance. This data rate is higher than the ones required for the temperature sensor, accelerometer, SP02 or ECG devices [82].

We first investigate the performance as a function of the IR average transmitted power $\boldsymbol{P_{t-IR}}$ for a sensor positioned at $\boldsymbol{H_{t-IR} = 1.5m}$.

The outage probability versus $\boldsymbol{SNR_0}$ is plotted in Figure 5.2 for receivers oriented at 45° at the corners of the panel and in Figure 5.3 for the orientation at 60°. Body reflectivity is set to ρ=0.1.

License CC BY-NC-ND 3.0

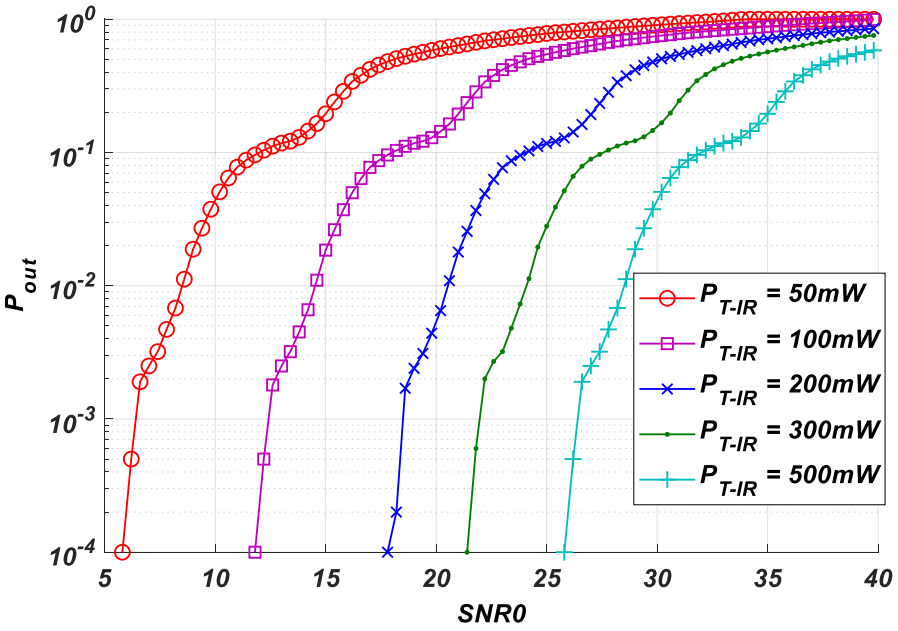

Figure 5.2. Outage probability of IR channel scenario (b), Rx orientation 45°, m=2, $H_{t-IR} = 1.5m$, body reflectivity ρ=0.1; $R_b = 1Mbps$

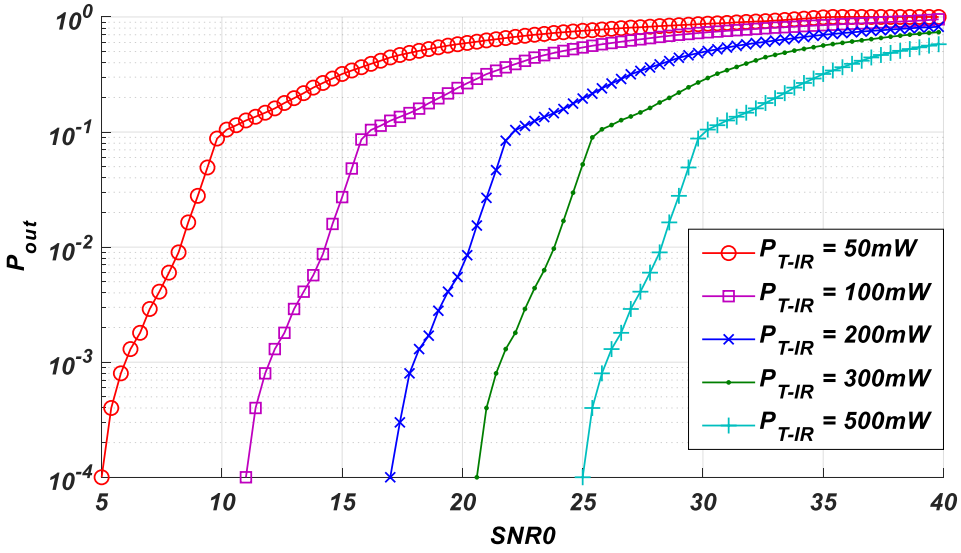

Figure 5.3. Outage probability of IR channel scenario (b), Rx orientation 60°, m=2, $H_{t-IR} = 1.5m$, body reflectivity ρ=0.1; $R_b = 1Mbps$

As expected, we observe that the outage probability increases with the SNR_0 for both orientations of receivers. Moreover, if the emitted power increases, performance is enhanced as the curves shift towards higher values of SNR_0.

License CC BY-NC-ND 3.0

To compare the results for the two orientations, we can extract from the two figures the values of SNR_0 corresponding to different qualities of service and that according to the emitted power. This is illustrated in Figure 5.4 for $P_{out} = \{10^{-1}; 10^{-2}; 10^{-3}\}$.

The results first confirm that the two orientations allow obtaining quite the same performance especially for low outrage probabilities that are high link quality. In the following, we focus on the scenario with 45° oriented receivers. All the figures for the 60° angle are provided in Appendix 07.

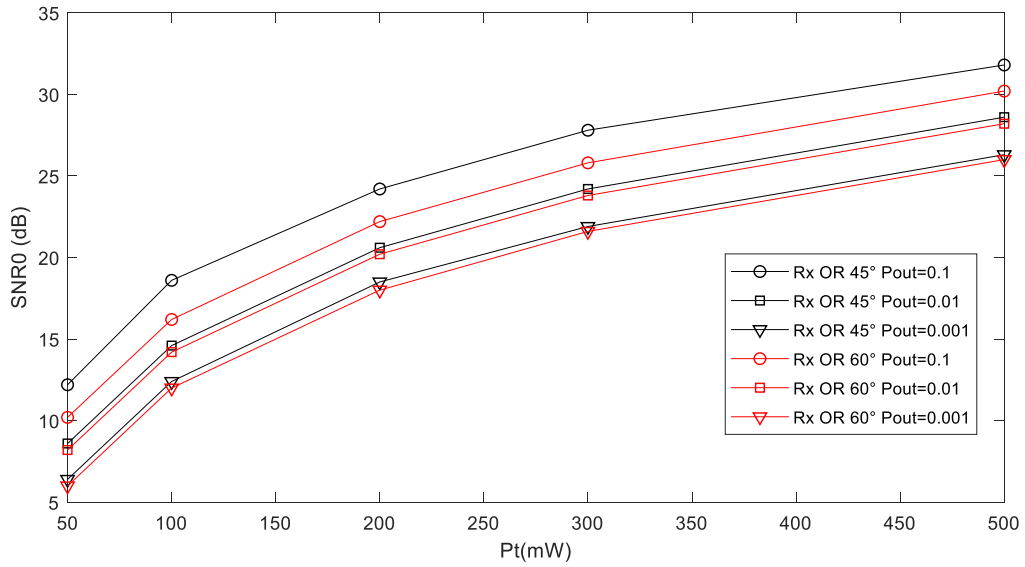

Figure 5.4. SNR_0 versus emitted power P_{t-IR} ; IR channel scenario (b), Rx orientation 45° and 60°, m=2, $H_{t-IR} = 1.5m$, body reflectivity ρ=0.1; $R_b = 1Mbps$

From Figure 5.4, the minimum power to be emitted for a given modulation can be determined in order to reach the targeted BER with a certain quality. As an example, for OOK modulation with a targeted BER of 10^{-9} that is $\text{SNR}_0 = 15.6\text{dB}$, we can see that the minimal power with Rx orientation of 45° is around $P_{t-IR} = \{75; 120; 155\}\, mW$ for $P_{out} = \{10^{-1}; 10^{-2}; 10^{-3}\}$.

Using (2.10) we can then determine the maximal axial intensity of the LED with m=2. We can remark that it is much lower than the maximal one required with standards [86, 87].

However, this conclusion can be different when the sensor is at a closer distance from the floor. We have reported in Figure 5.5 the outage probability for Rx orientation of 45°, considering that the emitter is at the ankle ($\boldsymbol{H_{t-IR} = 0.2m}$). As an example, for $\boldsymbol{P_{out} = 10^{-2}}$ the needed emitted power for $\boldsymbol{BER_{OOK} = 10^{-9}}$ is around 200mW (instead of 120mW when $\boldsymbol{H_{t-IR} = 1.5m}$).

License CC BY-NC-ND 3.0

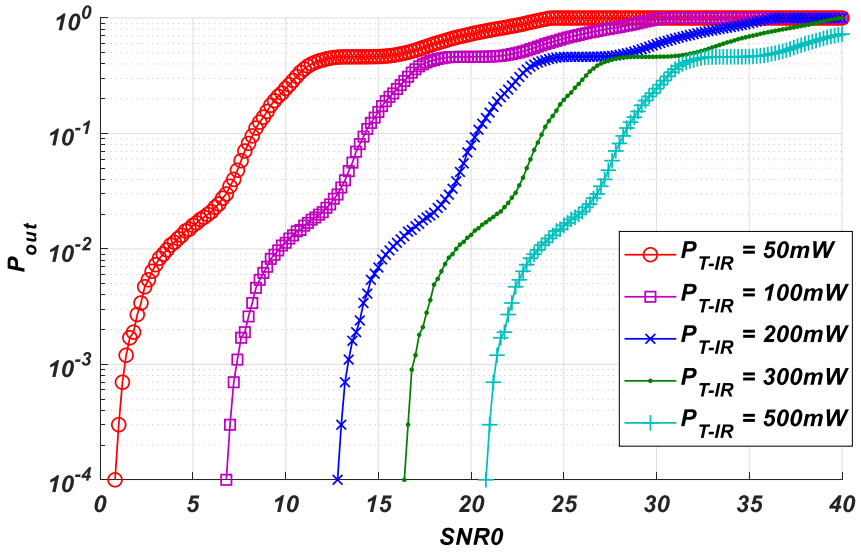

Figure 5.5. Outage probability of IR channel scenario (b), Rx orientation 45°, m=2, $H_{t-IR} = 0.2m$, body reflectivity ρ=0.1; $R_b = 1Mbps$

Finally, according to the conclusions of chapter III, the impact of the presence of the body is shown in Figure 5.6 for 45° oriented receivers, an ankle sensor and an emitted power of 100mW. Three reflectivity values of the body are considered.

We can remark that the SNR_0 value (that is BER for a given modulation) is all the more impacted as the targeted quality in terms of P_{out} is low. As an example, for a targeted $BER_{OOK} = 10^{-9}$, the outage probability is highly affected regarding body properties. Actually, P_{out} is about 10^{-2} for ρ=0.9 whereas it is of 2.10^{-1} for ρ=0.1.

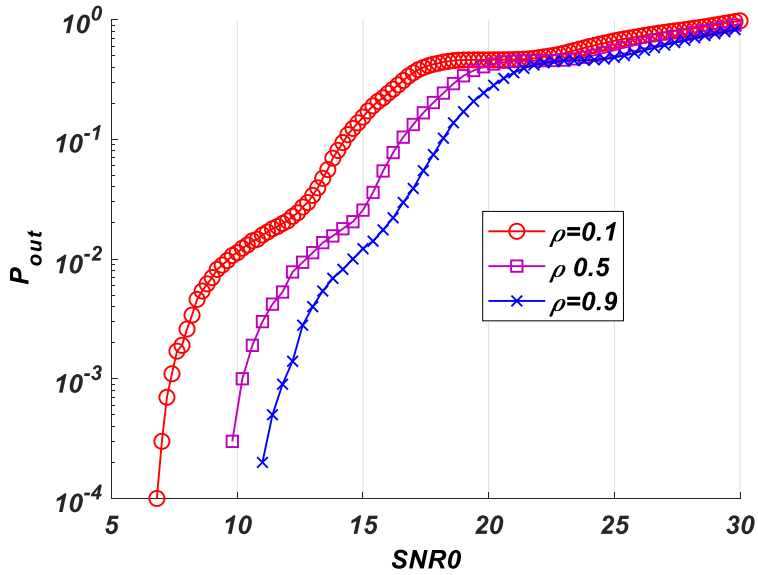

Figure 5.6. Outage probability of IR channel scenario (b), Rx orientation 45°, m=2, $H_{t-IR} = 0.2m$, $P_{t-IR} = 100mW$;body reflectivity ρ=0.1;0.5;0.9; $R_b = 1Mbps$

License CC BY-NC-ND 3.0

V.3. Visible downlink performance

We study in this part the performance of VLC link in the room of dimensions (6.7×6.6×3) m^3. Based on the theoretical study of chapter 4, the channel gain $\boldsymbol{H(0)}$ follows a statistical distribution related to random (X Y) coordinates and orientations of the VLC receiver carried by the moving patient. The receiver is supposed to be at a height $\boldsymbol{H_{T-VLC} = 1.2m}$ from the floor and 20cm in front of the patient body.

As for IR channel, a reflectivity coefficient between 0.1 and 0.9 is affected to body surfaces whereas all the environment surfaces are characterized by reflectivity a coefficient of 0.8.

Using the same definitions as in V.2, we determine the outage probability for the VLC downlink as a function of the emitted power $\boldsymbol{P_{t-VLC}}$ from the visible source (m=1) at the center of the room ceiling. Concerning the noise, the visible channel is more impacted by the background noise than IR. Thus, we consider here a noise power spectral density (equation (2)) with $\boldsymbol{I_{BVLC} = 5100\mu A}$ [110].

The results for a data rate of $\boldsymbol{R_b = 1Mbps}$ and considering a blocking body (ρ=0.1) are presented in Figure 5.7.

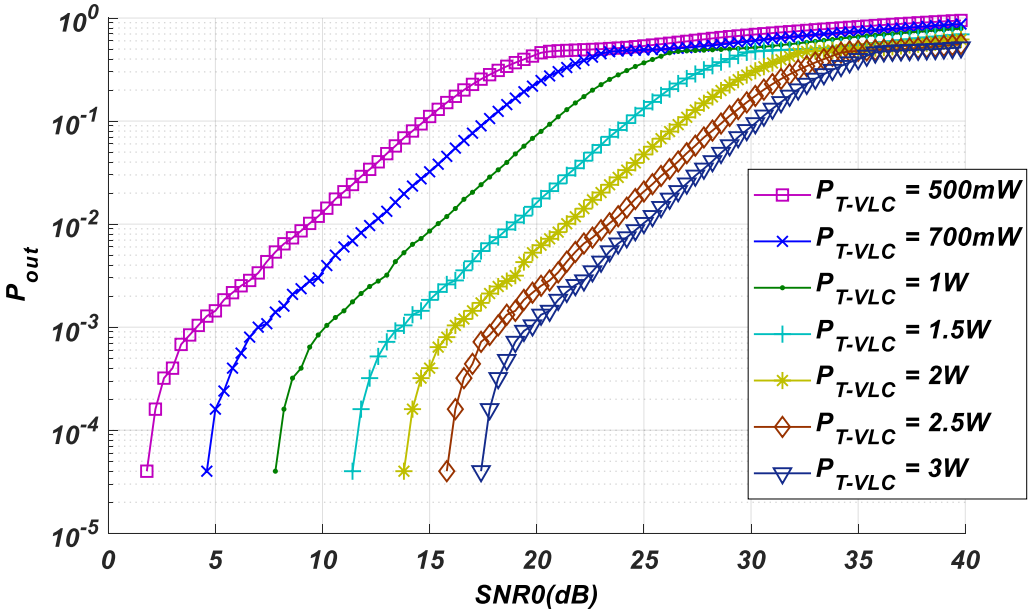

Figure 5.7. Outage probability of VLC channel, random Rx orientation, m=1, $\boldsymbol{H_{t-VLC} = 1.2m}$;body reflectivity ρ=0.1; $\boldsymbol{R_b = 1Mbps}$

License CC BY-NC-ND 3.0

The curves exhibit the same behavior as previously, performance degrading as the emitted power diminishes. However, we remark that the power values are higher than for IR channel that is obvious as noise impact is higher.

For example, for $\boldsymbol{P_{out} = 10^{-2}}$ the needed emitted power for $\boldsymbol{BER_{OOK} = 10^{-9}(SNR_0 = 15.6dB)}$ is around 1W (instead of 120mW for IR channel when $\boldsymbol{H_{t-IR} = 1.5m}$). For $\boldsymbol{P_{out} = 10^{-1}}$, respectivly $\boldsymbol{P_{out} = 10^{-3}}$, we find $\boldsymbol{P_{t-VLC} = 0.5W}$, respectively $\boldsymbol{P_{t-VLC} = 2W}$. Thus, as we have concluded from Figure 4.10, the VLC channel has lower performance than IR one.

Note that a visible power of 1W corresponds to an axial intensity of around 0.3W/m² for a Lambertian source (m=1). According to the power spectral profile and luminous efficacy of the lighting, this could lead to illumination much lower than typical value for the medical room [Table II-4 in 85].

The IR and VLC channels are different from the performance impact related to the reflectivity coefficient of the body. Indeed, it can be seen in Figure 5.8 that performance degradation is not linear as a function of ρ. The probability is much more impacted when the reflectivity coefficient is less than 0.5. As an example, for a targeted $\boldsymbol{BER_{OOK} = 10^{-9}}$, the outage probability $\boldsymbol{P_{out}}$ is about $\boldsymbol{10^{-2}}$ for ρ=0.1 whereas it is lower than $\boldsymbol{10^{-5}}$ for ρ≥0.5.

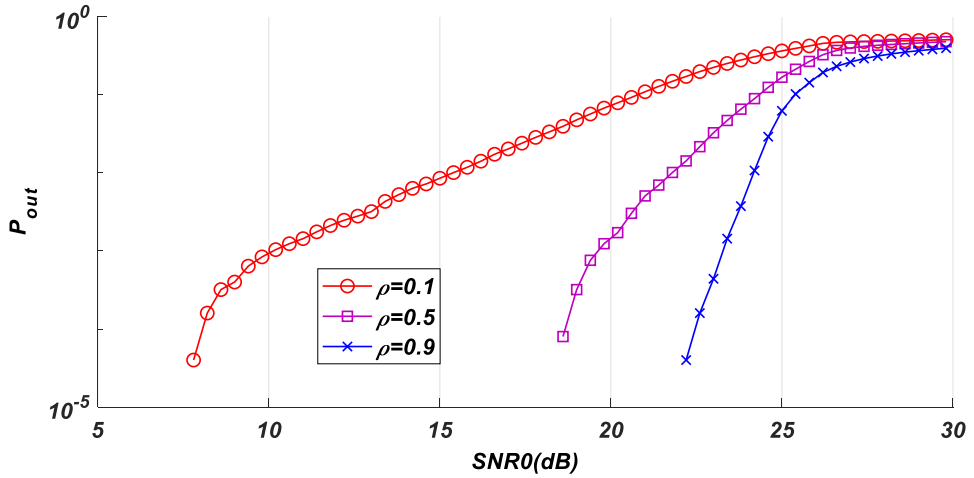

Figure 5.8. Outage probability of VLC channel, random Rx orientation, m=1, $\boldsymbol{H_{t-VLC} = 1.2m}$; $\boldsymbol{R_b = 1Mbps}$;body reflectivity ρ=0.1;0.5;0.9

License CC BY-NC-ND 3.0

V.4. Overall performance of IR uplink and visible downlink

To determine the potential of a luminaire incorporating IR receivers and a VLC transmitter as a medical monitoring system, we studied the performance of the IR and visible channels separately. The goal now is to determine overall performance.

V.4.1. Definitions

As we have seen, statistical channel behaviors are different for VLC and IR links. So, we use two different outage probabilities corresponding to each link and involving pairs of emitted power and data rates (P_{t-IR}, R_{b-IR}) respectively (P_{t-VLC}, R_{b-VLC}):

$$P_{out-IR} = p(SNR_{IR} < SNR_{0-IR})$$
$$P_{out-VLC} = p(SNR_{VLC} < SNR_{0-VLC}) \quad (6)$$

Considering that the system is in outage as soon as one of the links (uplink or downlink) is an outage (defined in relation to a given SNR_{0-IR} resp. SNR_{0-VLC}), we determine the global outage probability to evaluate the system performance as follows:

$$\begin{aligned} P_{out} &= p(SNR_{IR} < SNR_{0-IR} \cup SNR_{VLC} < SNR_{0-VLC}) \\ &= p(SNR_{IR} < SNR_{0-IR}) + p(SNR_{VLC} < SNR_{0-VLC}) \\ &\quad - p(SNR_{IR} < SNR_{0-IR}).p(SNR_{VLC} < SNR_{0-VLC}) \\ &= P_{out-IR} + P_{out-VLC} - P_{out-IR}.P_{out-VLC} \end{aligned} \quad (7)$$

The SNR limit values (SNR_{0-IR} and SNR_{0-VLC}) can be different depending on the target application for which different kinds of data can be sent in the uplink and downlink.

In this study, we consider that they are fixed to the same value: $SNR_{0-IR} = SNR_{0-VLC}$ = 15.6 dB, corresponding to a BER of around 10^{-9} for OOK modulation.

However, we will consider in the analysis that data rates and emitted powers are different and the aim is to evaluate which pairs satisfy a targeted global outage probability.

V.4.2. Results analysis

In this part, we consider the IR channel with only Rx orientation at 45°.

Considering the conclusions of the IR and VLC channels, the first discussion concerns the overall performance for different positions of the IR transmitter on the body. This analysis is done for a fixed data rate $R_{b-IR} = R_{b-VLC} = 1Mbps$.

From expression (7), and knowing the SNR distributions for a given system configuration, it is possible to determine which pairs (P_{t-VLC}, P_{t-IR}) generate a given P_{out}.

License CC BY-NC-ND 3.0

An example is given in Figure 5.9 for $SNR_{0-IR} = SNR_{0-VLC} = 15.6dB$ and for two positions of the IR emitter, H_{T-IR}=0.2m and H_{T-IR}=1.5m, assuming body reflectivity ρ = 0.1. We determined the pairs (P_{t-VLC}, P_{t-IR}) for 3 different targeted P_{out} and a data rate of R_b=1Mbps in VLC downlink and IR uplink.

Firstly, regardless of the H_{T-IR} value, the required VLC or IR powers are higher as the overall P_{out} target weakens. This is consistent with the IR channel behavior with regard to the emitter position on the body. In addition, to guarantee a given overall quality of service, if the IR power decreases, the VLC power related to the lighting level of the room must be increased and vice versa. From these curves, we can thus extract the two pairs of limit values for IR and VLC powers.

For example, for P_{out}=0.1 and H_{T-IR}=0.2m, the first pair of values corresponds to a minimal IR power $P_{t-IR-min}$ around 117mW with a maximal VLC power $P_{t-VLC-max}$ of 1.25W. The other pair is $P_{t-VLC-min}$ around 0.55W with a $P_{t-IR-max}$ of 228mW. However, the range of power values is reduced when the target outage probability P_{out} becomes low, i.e. when the quality of service is high.

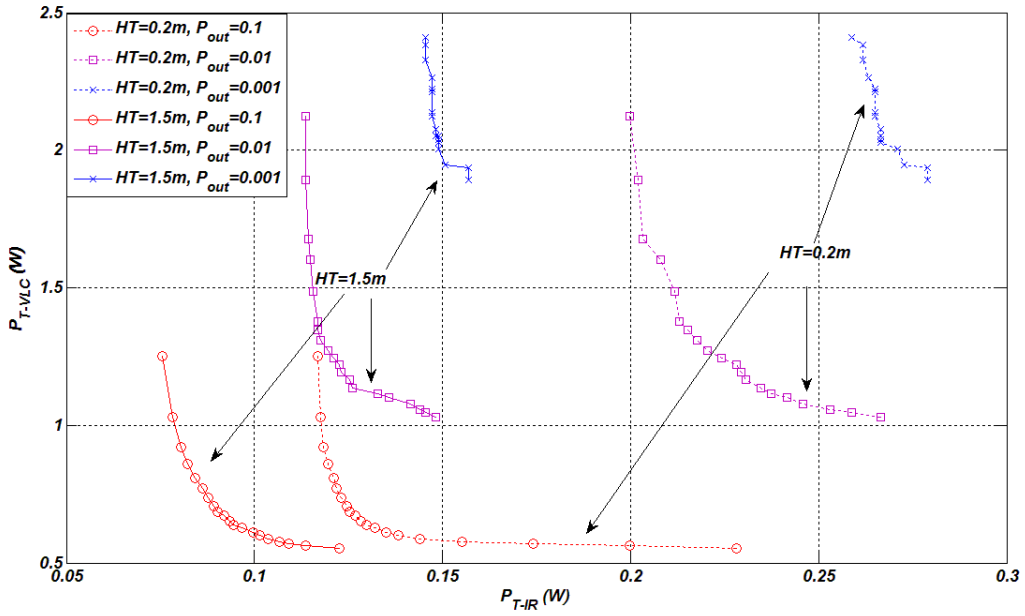

Figure 5.9. Evolution of IR and VLC emitted powers for 3 given values of P_{out} ; body reflectivity ρ=0.1, Height H_{T-IR}=0.2m and H_{T-IR}=1.5m; data rate $R_b = 1Mbps$.

We focus now on the more sensitive sensor location regarding body impact that is H_{T-IR}=0.2m. The goal is to show the potential of the proposed technology for this sensor position, the most impacted by body presence**.** For this sensor position, Figure 5.10 shows the pairs of

License CC BY-NC-ND 3.0

values ($P_{t-IR-min}$, $P_{t-VLC-max}$) corresponding to 3 different outage probabilities as a function of body reflectivity value ρ.

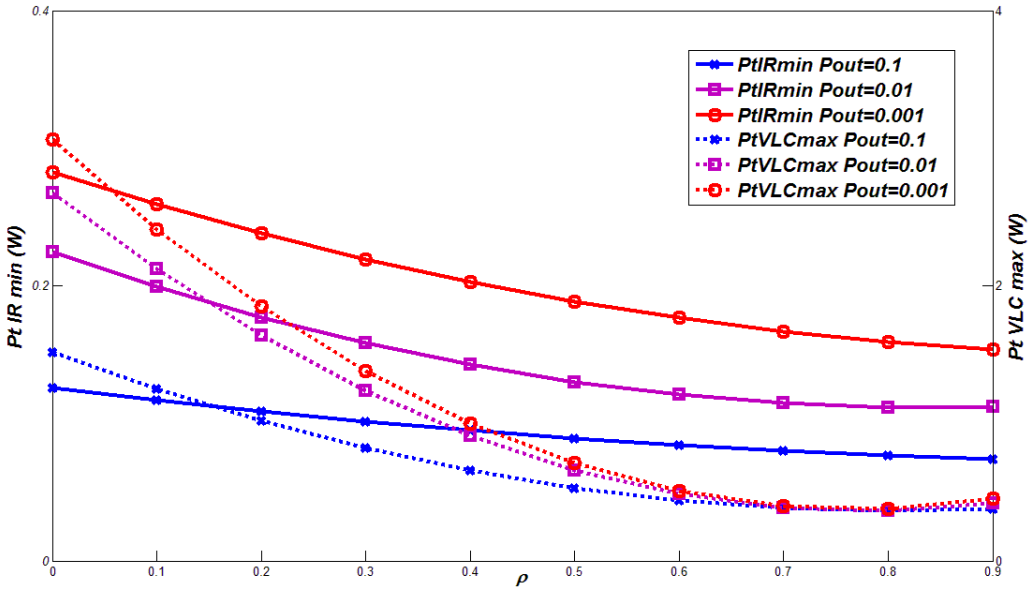

Figure 5.10. Evolution of, $P_{t-IR-min}$ (in plain lines) and $P_{t-VLC-max}$ (in dotted lines) for 3 given values of P_{out} as a function of body reflectivity ρ Height H_{T-IR} =0.2m; $R_b = 1Mbps$.

For $P_{t-IR-min}$, (curves in plain lines) and P_{out}=0.1, the reflectivity value ρ does not have a significant impact, whereas the impact is more important when the required outage probability is lower.

$P_{t-VLC-max}$ evolution does not follow the same pattern of behavior. It is not so heavily impacted by the required outage probability, regardless of the reflectivity value ρ. In addition, the reflectivity value has an impact only for ρ values lower than 0.5 which is consistent with the results of Figure 5.8.

For the same configuration, i.e. H_{T-IR}=0.2m and for the 3 different targeted outage probabilities, Figure 5.11 shows the corresponding pairs of values ($P_{t-VLC-min}$, $P_{t-IR-max}$).

$P_{t-VLC-min}$ variations, as for the $P_{t-VLC-max}$ value, do not depend on reflectivity values when ρ is higher than 0.5. However, for lower ρ values, they vary as a function of ρ and also as a function of the required outage probability.

Finally, the maximal power $P_{t-IR-max}$ for the IR link, is always lower than the classical admissive value for IR diffuse radiation considering laser safety standard (around 300mW [86]).

License CC BY-NC-ND 3.0

This is of great importance for consumption and highlights the potentiality of this VLC/IR solution for body sensor communication.

In addition, the results indicate that VLC power is always lower than 2W. This corresponds to weak illumination which can be important for monitoring applications for which data transmission has to be reliable whatever the lighting conditions.

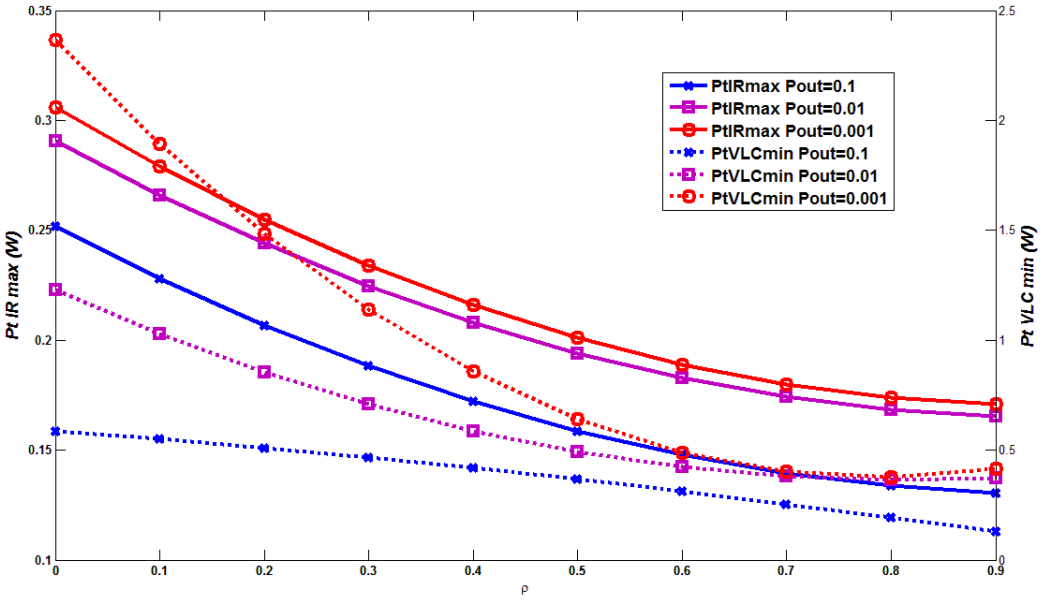

Figure 5.11. Evolution of, $P_{t-IR-max}$ (in plain lines) and $P_{t-VLC-min}$ (in dotted lines) for 3 given values of P_{out} as a function of body reflectivity ρ, Height H_{T-IR}=0.2m; $R_b = 1Mbps$.

To extend the conclusions, this analysis can be done for any other data rates, which are not necessarily the same for IR and VLC links. Thus, we analyze the variations of available data rates to reach a given outage for fixed power values.

We consider a particular case where P_{t-IR}=300mW. We assume also that P_{t-VLC} =2W.

Results are shown in Figure 5.12 for a reflectivity value ρ=0.1 and H_{T-IR}=0.2m and for the different levels of quality of service corresponding to P_{out}={10^{-1}; 10^{-2}; 10^{-3}}.

For all cases, the curves indicate that the proposed system can operate at data rates higher than 1 Mbps. For example, the pairs of maximal data rates for IR and VLC are ($R_{b-IR-max}$= 1.7 Mbps, $R_{b-VLC-max}$=13 Mbps) for P_{out}=0.1 and ($R_{b-IR-max}$= 1.2 Mbps, $R_{b-VLC-max}$=3.7 Mbps) for P_{out}=0.01. As expected, the range of data rate is reduced when the targeted outage probability is lower.

For P_{out}= 10^{-3} we are at the limit where $R_{b-IR-max}$~$R_{b-VLC-max}$~$1Mbps$.

License CC BY-NC-ND 3.0

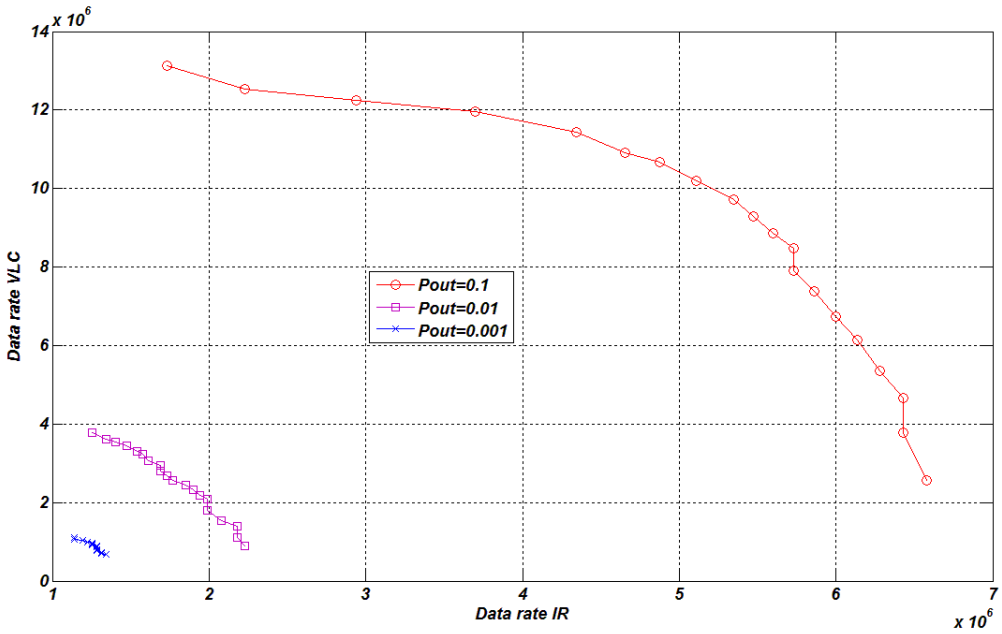

Figure 5.12. Evolution of, data rate for IR and VLC links for 2 given values of P_{out} ; P_{t-IR}=300mW and P_{t-VLC}=2W ; body reflectivity ρ=0.1, Height H_{T-IR}=0.2m

V.4. Conclusion

In this part, we proposed to evaluate the performance of an all-optical communication system using infrared uplink and visible downlink for body-sensor medical applications.

The studied scenario, named scenario (b) in the document, considered an IR communicating sensor worn by a patient and associated receivers positioned in a central ceiling luminaire. This luminaire can communicate in the visible range with a receiver also worn by the patient.

Performance has been analyzed taking into account the movements and the mobility of the patient in the environment, the position of the communicating sensor on the body and the impact of the body on optical propagation.

We have used channel statistics established in the previous chapters to first determine the outage probability for both links separately. A data rate of 1 Mbps was considered because it corresponds to the classic requirements for a large category of health-related sensors.

Concerning IR uplink, the results have shown that performance is quasi identical for the two values of receiver orientation determined in Chapter III that is 45° and 60°. As expected, we

License CC BY-NC-ND 3.0

have verified that the infrared link is degraded when the transmitted power decreases and / or when the sensor is placed closer to the ground. Body presence also has a strong impact on the probability of blockage.

On the same manner, VLC performance has been established in terms of outage probability for the same data rate. The behavior with respect to the transmitted power is the same, even if the power values are higher than for IR channel. This is because of the higher noise power considered in the visible range. However, there is a difference between the two links regarding the impact of body reflectivity. Visible downlink performance is more affected than IR for blocking bodies.

Then, we have determined the overall performance in terms of outage probability, jointly considering IR uplink and visible downlink transmissions. We focused on a scenario with a data rate of 1Mbps and OOK modulation with BER of 10^{-9} for both links.

The analysis of overall performance was first done by examining the emitting power-related issues. We determined the compromises required in IR and VLC powers to satisfy a given quality of service. Thus, the minimum power possible in infrared will correspond to maximum power in visible and vice versa.

An important result is that even with a sensor close to the ground e.g. at the ankle, the maximum power for the uplink did not exceed the maximum permissible value in IR diffuse emission.

Moreover, when the IR emitted power was minimized, the corresponding maximum VLC power did not depend on the quality of service or body reflectivity when it was greater than 0.5. This was the same when considering minimal VLC power and maximal IR one, versus body reflectivity. We also found that VLC maximal power corresponds to a low level of illumination, so the application does not highly dependent on lighting conditions.

Finally, we determined the maximum rates for which these conclusions are still valid. We have observed that for all outage probabilities values the proposed system can operate at data rates higher than 1 Mbps, which shows the potentialities of optical wireless technology in a body sensor context.

License CC BY-NC-ND 3.0

CONCLUSIONS AND PERSPECTIVES

Conclusion

With the spectral resources already saturated in the RF spectrum, it becomes more difficult to achieve wireless communications that can accommodate the growth of data traffic. As a result, wireless communications based on spectrum resources in the high-frequency ranges are considered. OWC is one of the most promising solutions, in particular in visible range because of LED lighting developments.

Applications and main challenges about OWC in infrared, visible and UV ranges have been presented in the first chapter of the thesis document.

In addition, RF technology cannot be used in areas sensitive to electromagnetic interference or when there are limitations and questions about the impact on health. The use of optical technology is therefore of great interest in these contexts. That is why we have studied in this thesis, the potentialities of this technology for a health monitoring system.

We have proposed to use IR technology for the data transmission between a worn sensor and receivers included at the corners of a central lighting panel. Visible link is then used for data transmission from the luminaire towards the patient carrying a VLC receiver. This all-optical configuration allows avoiding RF impact. Moreover, there are no interferences between uplink and downlink. For such a scenario, the main challenge is the link robustness regarding mobility and impact of user body because of sensor location. The data rate of the majority of health data is generally below the Mbps.

After the first chapter outlining the objectives, we presented in chapter II the different technical concepts related to infrared and visible optical communications. In particular, we defined the principles of intensity modulation and direct detection, as well as the characteristics of optical emission and reception components. We also presented the different configurations of indoor optical propagation, noise and modulation techniques.

In the majority of published works about IR technology, the body carrying infrared emitter is not taken into account. Therefore, the first goal in this thesis was to analyze the IR uplink channel behavior regarding both patient movement and sensor location on the body. This is the objective of Chapter III.

In the first part of this chapter, we first introduced the approach taken to study the channel. It is based on the Ray-Tracing technique associated with the Monte-Carlo method, implemented using a software developed at XLIM called RaPSor. This software provides the

License CC BY-NC-ND 3.0

impulse response of a wireless optical link. From the impulse response, we determined the static gain of the channel which is the main parameter representing the performance. Considering that the static gain is a random variable because the patient is mobile, the analysis was done statistically by mainly observing the cumulative density function. In addition, thanks to the simulation approach, we studied the effect of the human body carrying the transmitter. A 3D shape was used to model the body.

The study was conducted for two single-input-multiple-output (SIMO) scenarios named (a) and (b) that correspond to: (a) a system with four receivers uniformly distributed on the room ceiling; (b) a system with four receivers at the corners of a LED panel in the ceiling center. We have shown that when considering body modeling, the scenario (b) exhibits better performance compared to the scenario (a).

For the scenario (b), we then determined the optimal physical and geometrical parameters related to transmitters and receivers in order to guarantee the best performance. We showed that the four receivers included at the corners of the LED panel had to be oriented at angles of 45 ° or 60 °. Regarding the transmitter, we found that the best half-power angle of the source is 45° corresponding to a Lambertian order of 2. We also verified that, regardless of the position of the sensor on the body, it was not necessary to take into account the variations of the orientation angle of the transmitter. Therefore, the modeling of the scenario can be simplified by considering a perpendicular transmitter. In addition, we emphasized the importance of taking into account the body and its reflectivity, especially when the transmitter is close to the ground, e.g. at the ankle.

In the last part of the chapter, we presented the results of experimental tests of scenarios (a) and (b). We measured the packet loss for different sensor heights and with different methods. In particular**,** we have compared the results when the transmitter is worn at the ankle and when it is placed on a mobile platform at the same height. The results confirmed the significant impact of the body on performance. We also validated the main conclusions of the theoretical study with respect to the orientation angles of the receiver and the half-power angle of the source. The impact of the body is all the more important as the source has a wide half-power angle.

Therefore, it has been concluded that it is essential to model the presence of the body to determine the performance of the IR uplink for the body-sensor monitoring application.

Chapter IV deals with the study of the visible downlink. The channel behavior was studied by simulation as before using RaPSor. The same 3D body model was considered. The source lighting is supposed ideal and Lambertian, perpendicular to the ceiling. The VLC receiver is at a fixed position, carried at the user’s hand.

License CC BY-NC-ND 3.0

We pointed out that the parameters affecting performance were the body surface in front of the receiver and changes in receiver orientations related to patient movement. Besides, we found that the distance between the hand-held receiver and the body had almost no effect on the channel behavior.

We also presented an experimental part that used a LiFi fixture associated with a dongle. Measurements of the received power as a function of the body presence have confirmed that it is essential to take account of body and receiver orientations.

The overall performance of the system has been discussed in Chapter V.

We first studied the performance of each link from the static gains distributions established in previous chapters. The probability of link failure was determined considering a data rate of 1 Mbps.

For the IR uplink, the results showed that the performances are almost identical for the two orientation values of the receiver determined in Chapter III. As expected, we verified that the infrared link degraded as the transmitted power decreased. In addition, this was all the more significant as the sensor was placed closer to the ground. The body also has a high impact on outage probability.

In the same way, the visible downlink performance is degraded as the transmitted power decreases. As noise is more penalizing for the visible link, emitted power required for a given performance is higher than the one of the IR channel. In addition, we noted a difference between the two links with respect to the impact of body reflectivity. Visible downlink performance was more affected than IR for body blocking.

Next, we determined the overall performance for a data rate of 1Mbps and an OOK modulation with a BER of 10^{-9} for both links. We have determined the tradeoffs required between IR and VLC powers to satisfy a given quality of service.

For an ankle sensor, regardless of the quality of service, the IR power of the uplink did not exceed the maximum allowed by eye safety. In addition, the transmitted power required by the VLC depends nor on the quality of service neither on the body reflectivity when it is greater than the mean value. We also found that the maximum visible power corresponded to a low level of illumination, which means that this scenario can perform well under different lighting conditions. Finally, we determined the maximum rates and found that the proposed system could still operate at rates above 1 Mbps.

All of these theoretical conclusions confirm and emphasize the potential of all-optical wireless transmissions for medical surveillance based on body sensors.

License CC BY-NC-ND 3.0

Thus, the initial objective of the thesis has been reached from a theoretical point of view. Several experiments have partially validated the results but it remains to implement the complete system.

Perspectives

The first obvious prospect is to perform experiments for the global system. For this, we must develop our own VLC system to control the emitted powers, the data rate and modulation. There are also efforts to evaluate the level of noise but also the reflectivity of the surfaces of the environment and the body.

Simulations effort can be continued by taking into account more realistic modeling of movements. Studies are currently being conducted in our team on discretized movements based on animations made using the Blender software. This may be of interest especially for the study of the wrist-worn sensor, which is the most logical location for commercial products in health surveillance.

In addition, the studied system has been applied to the hospital and concerned adults. However, there are limitations and even precautionary principles (in France, the Abeille law of 2015) regarding the use of RF in the close environment of young children. It is, therefore, a perspective of our work by imagining scenarios for the surveillance of children, at school, in the nursery, in hospital maternity, pediatric or neonatal services as an example.

In addition, we can also study the performance of the system in the case where many people wear the same device and move in the same room. The idea here is that each person will have their own character and that these will have an impact on the performance of the system. For example, each person will have a different sensor, a different body reflection and also different activities. This will have an effect on the behavior of the channel. On the other hand, we can imagine that people in the same room can be connected to other people in another room and from there we can study the overall performance of all system.

More generally, health applications are one of the main contexts for the future deployment of optical technology, in particular, LiFi. In addition to monitoring scenarios that can improve the patient-centered approach and provide information and alert caregivers, there are other possible applications. For example, the LiFi can provide high-speed communications directly to the patient's bed without RF waves. It can offer secure and private communications, can track and move the positions of major medical devices or patients with behavioral disorders

License CC BY-NC-ND 3.0

according to their pathology. It is likely that when this technology reaches the level of maturity allowing access to the mass market, other scenarios will be imagined.

This work has led to four scientific publications. A first one has been presented at the international conference IEEE Healthcom in collaboration with another Ph.D. Student (C. Le Bas)

C. Le Bas, T. B. Hoang, S. Sahuguede and A. Julien-Vergonjanne, "Lighting fixture communicating in infrared and visible for indoor health monitoring," *2017 IEEE 19th International Conference on e-Health Networking, Applications and Services (Healthcom)*, Dalian, 2017, pp. 1-6.

In this publication, a mobile IR / VLC scenario was studied, but for a sensor position on the shoulder, so that the behavior of the IR channel was not affected by the body presence. Therefore, the body was not modeled for the analysis of the IR channel.

The in-depth study of the uplink IR channel has been the subject of two papers in international conferences. We presented the results concerning the optimization of the orientation of the receivers at the corners of the luminaire and the impact of the body, especially when the sensor is at the ankle.

T. B. Hoang, S. Sahuguede and A. Julien-Vergonjanne, "Behavior of non-directed optical wireless channel considering receiver orientation," *2017 20th International Symposium on Wireless Personal Multimedia Communications (WPMC)*, Bali, 2017, pp. 223-228.

T. B. Hoang, S. Kandukuri, S. Sahuguede, and A. Julien-Vergonjanne, "Infrared Mobile Transmissions for Smart Indoor Applications," *2018 11th International Symposium on Communication Systems, Networks & Digital Signal Processing (CSNDSP)*, Budapest, 2018, pp. 1-6.

A longer article on overall performance, essentially the results of Chapter V is under review:

T. B. Hoang, S. Sahuguede and A. Julien-Vergonjanne, “Optical wireless technology for body-sensor based monitoring” *2019 Hindawi - International Journal of Wireless Communications and Mobile Computing, (), 1-19.*

License CC BY-NC-ND 3.0

License CC BY-NC-ND 3.0

REFERENCES

[1] J. Gubbi, R. Buyya, S. Marusic, and M. Palaniswami, 'Internet of Things (IoT): A vision, architectural elements, and future directions', *Future Generation Computer Systems*, vol. 29, no. 7, pp. 1645–1660, Sep. 2013.

[2] X. Ge, H. Cheng, M. Guizani, and T. Han, '5G Wireless Backhaul Networks: Challenges and Research Advance', *IEEE Network*, vol. 28, no. 6, pp. 6–11, Nov. 2014.

[3] D. Evans, 'How the Next Evolution of the Internet Is Changing Everything', 2011.

[4] L. Hanzo, H. Haas, S. Imre, D. O'Brien, M. Rupp, and L. Gyongyosi, 'Wireless Myths, Realities, and Futures: From 3G/4G to Optical and Quantum Wireless', *Proceedings of the IEEE*, vol. 100, no. Special Centennial Issue, pp. 1853–1888, May 2012.

[5] A. G. Bell, "On the production and reproduction of sound by light", American Journal of science, no. 118, pp. 305-324, 1880.

[6] F. E. Goodwin, 'A review of operational laser communication systems', *Proceedings of the IEEE*, vol. 58, no. 10, pp. 1746–1752, 1970.

[7] N. Zheludev, 'the life and times of the LED — a 100-year history', *Nature Photonics*, vol. 1, no. 4, pp. 189–192, Apr. 2007.

[8] N. Holonyak and S. F. Bevacqua, 'Coherent (visible) light emission from Ga(As1-xPx) junctions', *Applied Physics Letters*, vol. 1, no. 4, pp. 82–83, Dec. 1962.

[9] S. Arnon, J. Barry, G. Karagiannidis, R. Schober, and M. Uysal, *Advanced Optical Wireless Communication Systems*. Cambridge University Press, 2012.

[10] Z. Ghassemlooy, W. Popoola, S. Rajbhandari, 'Optical Wireless Communications: System and Channel Modelling with MATLAB®', *CRC Press*, 2012.

[11] D. Karunatilaka, F. Zafar, V. Kalavally, and R. Parthiban, 'LED Based Indoor Visible Light Communications: State of the Art', *IEEE Communications Surveys & Tutorials*, vol. 17, no. 3, pp. 1649–1678, 2015.

[12] S. Arnon, 'Visible Light Communication', *Cambridge University Press New York, NY, USA ©*, vol. 1st, p. 264, 2015.

[13] S. Dimitrov and H. Haas, *Principles of LED Light Communications: Towards Networked Li-Fi*. Cambridge University Press, 2015.

[14] Z. Ghassemlooy, L. N. Alves, S. Zvanovec, M. A. Khalighi, 'Visible Light Communications: Theory and Applications', *CRC Press*, 2017.

[15] Z. Xu and B. M. Sadler, 'Ultraviolet Communications: Potential and State-Of-The-Art', *IEEE Communications Magazine*, vol. 46, no. 5, pp. 67–73, May 2008.

License CC BY-NC-ND 3.0

[16] Z. Ghassemlooy, S. Arnon, M. Uysal, Z. Xu, and J. Cheng, ‘Emerging Optical Wireless Communications Advances and Challenges’, *IEEE Journal on Selected Areas in Communications*, vol. 33, no. 9, pp. 1738–1749, Sep. 2015.

[17] M. Z. Chowdhury, M. T. Hossan, A. Islam, and Y. M. Jang, ‘A Comparative Survey of Optical Wireless Technologies: Architectures and Applications’, *IEEE Access*, vol. 6, pp. 9819–9840, 2018.

[18] M. A. Khalighi and M. Uysal, ‘Survey on Free Space Optical Communication: A Communication Theory Perspective’, *IEEE Communications Surveys & Tutorials*, vol. 16, no. 4, pp. 2231–2258, 2014.

[19] E. Leitgeb, ‘Future applications of Optical Wireless and combination scenarios with RF technology’, in *2017 40th International Convention on Information and Communication Technology, Electronics and Microelectronics (MIPRO)*, Opatija, Croatia, 2017, pp. 404–406.

[20] V. W. S. Chan, ‘Optical satellite networks’, *Journal of Lightwave Technology*, vol. 21, no. 11, pp. 2811–2827, Nov. 2003.

[21] Y. Tanaka, S. Haruyama, and M. Nakagawa, ‘Wireless optical transmissions with white colored LED for wireless home links’, in *11th IEEE International Symposium on Personal Indoor and Mobile Radio Communications. PIMRC 2000. Proceedings (Cat. No.00TH8525)*, London, UK, 2000, vol. 2, pp. 1325–1329.

[22] ‘Visible Light Communications Consotium (VLCC) - LED’. [Online]. Available: http://www.vlcc.net/?ml_lang=en. [Accessed: 21-Mar-2019].

[23] IEEE Standard for Local and Metropolitan Area Networks--Part 15.7: Short-Range Wireless Optical Communication Using Visible Light, IEEE, Sep. 2011.

[24] N. Lourenco, D. Terra, N. Kumar, L. N. Alves, and R. L. Aguiar, ‘Visible Light Communication System for outdoor applications’, in *2012 8th International Symposium on Communication Systems, Networks & Digital Signal Processing (CSNDSP)*, Poznan, Poland, 2012, pp. 1–6.

[25] V. M. Baeza, M. Sanchez-Fernandez, A. G. Armada, and A. Royo, ‘Testbed for a LiFi system integrated in streetlights’, in *2015 European Conference on Networks and Communications (EuCNC)*, Paris, France, 2015, pp. 517–521.

[26] B. Bechadergue, ‘Mesure de distance et transmission de données inter-véhicules par phares à LED. Thèse de Doctorat: Traitement du signal et de l’image. Université Paris-Saclay, 2017’, p. 255.

License CC BY-NC-ND 3.0

[27] P. H. Pathak, X. Feng, P. Hu, and P. Mohapatra, 'Visible Light Communication, Networking, and Sensing: A Survey, Potential and Challenges', *IEEE Communications Surveys & Tutorials*, vol. 17, no. 4, pp. 2047–2077, 2015.

[28] A. R. Ndjiongue and H. C. Ferreira, 'An overview of outdoor visible light communications: *Transactions on Emerging Telecommunications Technologies*, vol. 29, no. 7, p. e3448, Jul. 2018.

[29] H. Kaushal and G. Kaddoum, 'Underwater Optical Wireless Communication', *IEEE Access*, vol. 4, pp. 1518–1547, 2016.

[30] C. Gabriel, M.-A. Khalighi, S. Bourennane, P. Léon, and V. Rigaud, 'Monte-Carlo-Based Channel Characterization for Underwater Optical Communication Systems', *Journal of Optical Communications and Networking*, vol. 5, no. 1, p. 1, Jan. 2013.

[31] F. R. Gfeller and U. Bapst, 'Wireless in-house data communication via diffuse infrared radiation', *Proceedings of the IEEE*, vol. 67, no. 11, pp. 1474–1486, 1979.

[32] D. C. O'Brien *et al.*, 'High-speed integrated transceivers for optical wireless', *IEEE Communications Magazine*, vol. 41, no. 3, pp. 58–62, Mar. 2003.

[33] H. Elgala, R. Mesleh, and H. Haas, 'Indoor optical wireless communication: potential and state-of-the-art', *IEEE Communications Magazine*, vol. 49, no. 9, pp. 56–62, Sep. 2011.

[34] 'Infrared Data Association (IrDA)'. [Online]. Available: http://www.irda.org/. [Accessed: 21-Mar-2019].

[35] A. Boucouvalas, P. Chatzimisios, Z. Ghassemlooy, M. Uysal, and K. Yiannopoulos, 'Standards for indoor Optical Wireless Communications', *IEEE Communications Magazine*, vol. 53, no. 3, pp. 24–31, Mar. 2015.

[36] J. M. Kahn and J. R. Barry, 'Wireless Infrared Communications', in Proceeding of the IEEE, vol. 85, no. 2, p. 34, 1997.

[37] D. K. Borah, A. C. Boucouvalas, C. C. Davis, S. Hranilovic, and K. Yiannopoulos, 'A review of communication-oriented optical wireless systems', *EURASIP Journal on Wireless Communications and Networking*, vol. 2012, no. 1, Dec. 2012.

[38] G. W. Marsh and J. M. Kahn, 'Performance evaluation of experimental 50-Mb/s diffuse infrared wireless link using on-off keying with decision-feedback equalization', *IEEE Transactions on Communications*, vol. 44, no. 11, pp. 1496–1504, Nov. 1996.

[39] S. T. Jovkova and M. Kavehard, 'Multispot diffusing configuration for wireless infrared access', *IEEE Transactions on Communications*, vol. 48, no. 6, pp. 970–978, Jun. 2000.

[40] D. R. Kolev, M. Matsumoto, K. Wakamori, T. Kubo, T. Yamada, and N. Yoshimoto, 'Hybrid line-of-sight indoor infrared laser wireless link with 10Gbps downlink and 1Gbps

License CC BY-NC-ND 3.0

uplink', in *2013 2nd International Workshop on Optical Wireless Communications (IWOW)*, Newcastle upon Tyne, United Kingdom, 2013, pp. 132–136.

[41] T. Koonen, 'Indoor Optical Wireless Systems: Technology, Trends, and Applications', *Journal of Lightwave Technology*, vol. 36, no. 8, pp. 1459–1467, Apr. 2018.

[42] A. Nirmalathas *et al.*, 'Multi-gigabit indoor optical wireless networks — Feasibility and challenges', in *2016 IEEE Photonics Society Summer Topical Meeting Series (SUM)*, Newport Beach, CA, USA, 2016, pp. 130–131.

[43] https://www.oledcomm.net: [Accessed: 21-Mar-2019].

[44] https://purelifi.com: [Accessed: 21-Mar-2019].

[45] H. Haas, 'LiFi is a paradigm-shifting 5G technology', *Reviews in Physics*, vol. 3, pp. 26–31, Nov. 2018.

[46] T. Nguyen, 'OCC Standardization Roadmap', *Optical Camera Communication*, 12-Aug-2018. [Accessed: 21-Mar-2019].

[47] T. Komine and M. Nakagawa, 'Fundamental analysis for visible-light communication system using LED lights', *IEEE Transactions on Consumer Electronics*, vol. 50, no. 1, pp. 100–107, Feb. 2004.

[48] S. Al-Ahmadi, O. Maraqa, M. Uysal, and S. M. Sait, 'Multi-User Visible Light Communications: State-of-the-Art and Future Directions', *IEEE Access*, vol. 6, pp. 70555–70571, 2018.

[49] 'LiFi Technology - Velmenni | Optical Wireless Data Transmission'. [Online]. Available: https://www.velmenni.com/. [Accessed: 21-Mar-2019].

[50] 'Vlncomm - Limitless connectivity', *Superior, Enterprise-Grade, Light-Based Wireless Connectivity Platform*. [Online]. Available: https://vlncomm.com/. [Accessed: 21-Mar-2019].

[51] T.-H. Do and M. Yoo, 'An in-Depth Survey of Visible Light Communication Based Positioning Systems', *Sensors*, vol. 16, no. 5, p. 678, May 2016.

[52] H. Elgala, R. Mesleh, and H. Haas, 'Practical considerations for indoor wireless optical system implementation using OFDM', *ConTEL 2009. 10th International Conference on, 25-29*, p. 5, 2009.

[53] M. Biagi and A. M. Vegni, 'Enabling high data rate VLC via MIMO-LEDs PPM', in *2013 IEEE Globecom Workshops (GC Wkshps)*, Atlanta, GA, 2013, pp. 1058–1063.

[54] R. X. G. Ferreira *et al.*, 'High Bandwidth GaN-Based Micro-LEDs for Multi-Gb/s Visible Light Communications', *IEEE Photonics Technology Letters*, vol. 28, no. 19, pp. 2023–2026, Oct. 2016.

License CC BY-NC-ND 3.0

[55] R. Bian, I. Tavakkolnia, and H. Haas, ‘10.2 Gb/s Visible Light Communication with Off-the-Shelf LEDs’, in *2018 European Conference on Optical Communication (ECOC)*, Rome, 2018, pp. 1–3.

[56] H. Haas, L. Yin, Y. Wang, and C. Chen, ‘What is LiFi?’, *Journal of Lightwave Technology*, vol. 34, no. 6, pp. 1533–1544, Mar. 2016.

[57] N. Anous, T. Ramadan, M. Abdallah, K. Qaraqe, and D. Khalil, ‘Impact of blue filtering on effective modulation bandwidth and wide-angle operation in white LED-based VLC systems’, *OSA Continuum*, vol. 1, no. 3, p. 910, Nov. 2018.

[58] C. Le Bas, S. Sahuguede, A. Julien-Vergonjanne, A. Behlouli, P. Combeau, and L. Aveneau, ‘Impact of receiver orientation and position on Visible Light Communication link performance’, in *2015 4th International Workshop on Optical Wireless Communications (IWOW)*, Istanbul, Turkey, 2015, pp. 1–5.

[59] A. A. Purwita, M. Dehghani Soltani, M. Safari, and H. Haas, ‘Impact of terminal orientation on performance in LiFi systems’, in *2018 IEEE Wireless Communications and Networking Conference (WCNC)*, Barcelona, 2018, pp. 1–6.

[60] T. Borogovac, M. B. Rahaim, M. Tuganbayeva, and T. D. C. Little, ‘Lights-off visible light communications’, in *2011 IEEE GLOBECOM Workshops (GC Wkshps)*, Houston, TX, USA, 2011, pp. 797–801.

[61] J. E. Bardram, ‘Hospitals of the Future – Ubiquitous Computing support for Medical Work in Hospitals’, *UbiHealth 2003: The 2nd International Workshop on Ubiquitous Computing for Pervasive Healthcare Applications*, p. 8.

[62] D. Dias, P. S. Cunha, J, ‘Wearable Health Devices-Vital Signs Monitoring’, the Systems and Technologies. Sensors, Basel, Switzerland, 2018, pp. 18(8), 2414.

[63] H. Karvonen, K. Mikhaylov, M. Hamalainen, J. Iinatti, and C. Pomalaza-Raez, ‘Interference of wireless technologies on BLE based WBANs in hospital scenarios’, in *2017 IEEE 28th Annual International Symposium on Personal, Indoor, and Mobile Radio Communications (PIMRC)*, Montreal, QC, 2017, pp. 1–6.

[64] ‘IEC 60601-1.2014, Medical electrical equipment - 62A : Common aspects of electrical equipment used in medical practice'

[65] ‘ISO/IEEE International Standard Health informatics - Point-of-care medical device communication - Transport profile - Infrared’, in ISO/IEEE 11073-30300:2004(E), vol., no., pp.1-0, 15 Dec.2004.

License CC BY-NC-ND 3.0

[66] S. S. Torkestani, S. Sahuguede, A. Julien-Vergonjanne, and J. P. Cances, 'Indoor optical wireless system dedicated to healthcare application in a hospital', *IET Communications*, vol. 6, no. 5, p. 541, 2012.

[67] S. S. Torkestani, N. Barbot, S. Sahuguede, A. Julien-Vergonjanne, and J. P. Cances, 'Performance and transmission power bound analysis for optical wireless based mobile healthcare applications', in *2011 IEEE 22nd International Symposium on Personal, Indoor and Mobile Radio Communications*, Toronto, ON, Canada, 2011, pp. 2198–2202.

[68] S. S. Torkestani, S. Sahuguede, A. Julien-Vergonjanne, J. Cances, and J. C. Daviet, 'Infrared Communication Technology Applied to Indoor Mobile Healthcare Monitoring System':, *International Journal of E-Health and Medical Communications*, vol. 3, no. 3, pp. 1–11, Jul. 2012.

[69] A. M. Khalid, G. Cossu, and E. Ciaramella, 'Diffuse IR-optical wireless system demonstration for mobile patient monitoring in hospitals', in *2013 15th International Conference on Transparent Optical Networks (ICTON)*, Cartagena, Spain, 2013, pp. 1–4.

[70] P. Toumieux, S. Sahuguède, L. Chevalier, and A. Julien-Vergonjanne, 'Optical wireless connected objects for healthcare', *Healthcare Technology Letters*, vol. 2, no. 5, pp. 118–122, Oct. 2015.

[71] E. A. Alyan and S. A. Aljunid, 'Development of wireless optical CDMA system for biosignal monitoring', *Optik*, vol. 145, pp. 250–257, Sep. 2017.

[72] L. Chevalier, S. Sahuguede, and A. Julien-Vergonjanne, 'Optical Wireless Links as an Alternative to Radio-Frequency for Medical Body Area Networks', *IEEE Journal on Selected Areas in Communications*, vol. 33, no. 9, pp. 2002–2010, Sep. 2015.

[73] Yee Yong Tan, Sang-Joong Jung, and Wan-Young Chung, 'Real time biomedical signal transmission of mixed ECG Signal and patient information using visible light communication', in *2013 35th Annual International Conference of the IEEE Engineering in Medicine and Biology Society (EMBC)*, Osaka, 2013, pp. 4791–4794.

[74] Y.-K. Cheong, X.-W. Ng, and W.-Y. Chung, 'Hazardless Biomedical Sensing Data Transmission Using VLC', *IEEE Sensors Journal*, vol. 13, no. 9, pp. 3347–3348, Sep. 2013.

[75] T. Yee-Yong and C. Wan-Young, 'Mobile health monitoring system through visible light communication', *Bio-Medical Materials and Engineering*, no. 6, pp. 3529–3538, 2014.

[76] W. Noonpakdee, 'Performance analysis of passive. Active optical wireless transmission for personal health monitoring', in *2014 Sixth International Conference on Ubiquitous and Future Networks (ICUFN)*, Shanghai, China, 2014, pp. 17–21.

License CC BY-NC-ND 3.0

[77] W. A. Cahyadi, T.-I. Jeong, Y.-H. Kim, Y.-H. Chung, and T. Adiono, 'Patient monitoring using Visible Light uplink data transmission', in *2015 International Symposium on Intelligent Signal Processing and Communication Systems (ISPACS)*, Nusa Dua Bali, Indonesia, 2015, pp. 431–434.

[78] D. R. Dhatchayeny, A. Sewaiwar, S. V. Tiwari, and Y. H. Chung, 'EEG biomedical signal transmission using visible light communication', in *2015 International Conference on Industrial Instrumentation and Control (ICIC)*, Pune, India, 2015, pp. 243–246.

[79] A. Al-Qahtani *et al.*, 'A non-invasive remote health monitoring system using visible light communication', in *2015 2nd International Symposium on Future Information and Communication Technologies for Ubiquitous HealthCare (Ubi-HealthTech)*, Beijing, China, 2015, pp. 1–3.

[80] V. P. Rachim, J. An, P. N. Quan, and W.-Y. Chung, 'A novel smartphone camera-LED Communication for clinical signal transmission in mHealth-rehabilitation system', in *2017 39th Annual International Conference of the IEEE Engineering in Medicine and Biology Society (EMBC)*, Jeju Island, South Korea, 2017, pp. 3437–3440.

[81] C.R. Uma Kumari, S. Dhanalakshmi, 'All Optical Health Monitoring System: An Experimental Study on Visible Light Communication in Biomedical Signal Transmission', *Saini H., Singh R., Reddy K. (Eds) Innovations in Electronics and Communication Engineering. Lecture Notes in Networks and Systems, vol 7. Springer, Singapore*, 2018, pp 361-370.

[82] A. Julien-Vergonjanne, S. Sahuguède, and L. Chevalier, 'Optical Wireless Body Area Networks for Healthcare Applications', in *Optical Wireless Communications*, M. Uysal, C. Capsoni, Z. Ghassemlooy, A. Boucouvalas, and E. Udvary, Eds. Springer International Publishing, 2016, pp. 569–587.

[83] A. Hadjidj, M. Souil, A. Bouabdallah, Y. Challal, and H. Owen, 'Wireless sensor networks for rehabilitation applications: Challenges and opportunities', *Journal of Network and Computer Applications*, vol. 36, no. 1, pp. 1–15, Jan. 2013.

[84] A. Behlouli, 'Simulation du canal optique sans fil. Applications aux communications optiques sans fil', *Thèse de doctorat en Électronique des hautes fréquences, photonique et systèmes - Université de Poitiers 2016*.

[85] C. Le Bas, 'Système de télésurveillance médicale utilisant la technologie de transmission optique sans fil', *Thèse de doctorat en Électronique des hautes fréquences, photonique et systèmes Université de Limoges 2017*.

[86] 'IEC 60825-1.2007, Safety of laser products — Part1 Equipment classification and requirement'.

License CC BY-NC-ND 3.0

[87] ‘IEC 62471 (2006) Photobiological safety of lamps and lamp systems (identical with CIE S009)’.

[88] TSAL6400 data sheet https://www.vishay.com/docs/81011/tsal6400.pdf.

[89] M. Kavehrad, M.I.S. Chowdhury, Z. Zhou, ‘Short Range Optical Wireless: Theory and Applications’, Wiley Telecom, Oct. 2015.

[90] S. Muthu, F. J. P. Schuurmans, and M. D. Pashley, ‘Red, green, and blue LEDs for white light illumination’, *IEEE Journal of Selected Topics in Quantum Electronics*, vol. 8, no. 2, pp. 333–338, Apr. 2002.

[91] P. Louro, V. Silva, I. Rodrigues, M. A. Vieira, and M. Vieira, ‘Transmission of Signals Using White LEDs for VLC Applications1’, *Materials Today: Proceedings*, vol. 3, no. 3, pp. 780–787, 2016.

[92] S. Tanabe, S. Fujita, S. Yoshihara, A. Sakamoto, and S. Yamamoto, ‘YAG glass-ceramic phosphor for white LED (II): luminescence characteristics’, presented at the Optics & Photonics 2005, San Diego, California, USA, 2005, p. 594112.

[93] P. A. Haigh, Z. Ghassemlooy, S. Rajbhandari, and I. Papakonstantinou, ‘Visible light communications using organic light emitting diodes’, *IEEE Communications Magazine*, vol. 51, no. 8, pp. 148–154, Aug. 2013.

[94] CIE Commission Internationale de l’Eclairage Proceedings (Cambridge University Press, Cambridge, 1931).

[95] ‘CIE 1988 2° spectral luminous efficiency function for photopic vision | CIE’. [Online]. Available: http://www.cie.co.at/publications/cie-1988-2-spectral-luminous-efficiency-function-photopic-vision. [Accessed: 21-Mar-2019].

[96] OSRAM, Application Note AN002 Details on photobiological safety of LED light sources.

[97] R. E. Levin, ‘Photobiological Safety and Risk—ANSI/IESNA RP-27 Series’, *Journal of the Illuminating Engineering Society*, vol. 27, no. 1, pp. 136–143, Jan. 1998.

[98] R. Ramirez Iniguez, S. M. Idrus, Z. Sun: Optical Wireless Communications: IR for Wireless Connectivity, *CRC Press, Apr 2008*.

[99] M. E. Marhic, M. D. Kotzin, and A. P. van den Heuvel, ‘Reflectors and immersion lenses for detectors of diffuse radiation’, *Journal of the Optical Society of America*, vol. 72, no. 3, p. 352, Mar. 1982.

[100] J. R. Barry, *Wireless Infrared Communications*. The Springer International Series in Engineering and Computer Science, Springer US, 1994.

License CC BY-NC-ND 3.0

[101] N. T. Le, M. S. Ifthekhar, Y. M. Jang, and N. Saha, ‘Survey on optical camera communications: challenges and opportunities’, *IET Optoelectronics*, vol. 9, no. 5, pp. 172–183, Oct. 2015.

[102] S. Zhang *et al.*, ‘Organic solar cells as high-speed data detectors for visible light communication’, *Optica*, vol. 2, no. 7, p. 607, Jul. 2015.

[103] J. R. Barry, J. M. Kahn, W. J. Krause, E. A. Lee, and D. G. Messerschmitt, ‘Simulation of multipath impulse response for indoor wireless optical channels’, *IEEE Journal on Selected Areas in Communications*, vol. 11, no. 3, pp. 367–379, Apr. 1993.

[104] J. B. Carruthers and J. M. Kahn, ‘Modeling of Nondirected Wireless Infrared Channels’, *IEEE Transactions on Communications*, vol. 45, no. 10, p. 9, 1997.

[105] F. J. Lopez-Hernandez, R. Perez-Jimenez, and A. Santamaria, ‘Monte Carlo calculation of impulse response on diffuse IR wireless indoor channels’, Lett., 34, no. 12, pp. 1260–1262, p. 3, Jun. 1998.

[106] A. Behlouli, P. Combeau, L. Aveneau, S. Sahuguede, and A. Julien-Vergonjanne, ‘Efficient Simulation of Optical Wireless Channel Application to WBANs with MISO Link’, *Procedia Computer Science*, vol. 40, pp. 190–197, 2014.

[107] K. Lee, H. Park, and J. R. Barry, ‘Indoor Channel Characteristics for Visible Light Communications’, *IEEE Communications Letters*, vol. 15, no. 2, pp. 217–219, Feb. 2011.

[108] A. M. Baldridge, S. J. Hook, C. I. Grove, and G. Rivera, ‘The ASTER spectral library version 2.0’, *Remote Sensing of Environment*, vol. 113, no. 4, pp. 711–715, Apr. 2009.

[109] A. C. Boucouvalas, “Indoor ambient light noise and its effect on wireless optical links”, in IEEE Proceedings - Optoelectronics, vol. 143, no. 6, pp. 334-338 Dec. 1996.

[110] A. J. C. Moreira, R. T. Valadas, and A. M. de Oliveira Duarte, ‘Characterisation and modelling of artificial light interference in optical wireless communication systems’, in *Proceedings of 6th International Symposium on Personal, Indoor and Mobile Radio Communications*, Toronto, Ont., Canada, 1995, vol. 1, pp. 326–331.

[111] 'Ethernet Over Light', Philip Mark, McGill University, 2011.

[112] A. J. C. Moreira et al., ‘Reducing the effects of artificial light interference in wireless infrared transmission systems’, in *IEE Colloquium on Optical Free Space Communication Links*, London, UK, 1996, vol. 1996.

[113] ‘K. Cui, Physical Layer Characteristics and Techniques for Visible Light Communications, PhD. dissertation, Univerity of California, Riverside, 2012’.

[114] S. B. Alexander, *Optical communication receiver design*. Bellingham, Wash., USA; London, UK: SPIE Optical Engineering Press ; Institution of Electrical Engineers, 1997.

License CC BY-NC-ND 3.0

[115] J. B. Carruthers and J. M. Kahn, 'Multiple-Subcarrier Modulation for Nondirected Wireless Infrared Communication', *IEEE Journal on selected areas in Communications*, vol. 14, no. 3, p. 9, 1996.

[116] S. C. J. Lee, S. Randel, F. Breyer, and A. M. J. Koonen, 'PAM-DMT for Intensity-Modulated and Direct-Detection Optical Communication Systems', *IEEE Photonics Technology Letters*, vol. 21, no. 23, pp. 1749–1751, Dec. 2009.

[117] H. Elgala, R. Mesleh, H. Haas, and B. Pricope, 'OFDM Visible Light Wireless Communication Based on White LEDs', in *2007 IEEE 65th Vehicular Technology Conference - VTC2007-Spring*, Dublin, Ireland, 2007, pp. 2185–2189.

[118] J. Armstrong and A. J. Lowery, 'Power efficient optical OFDM', *Electronics Letters*, vol. 42, no. 6, p. 370, 2006.

[119] M. S. Islim and H. Hass, 'Modulation Techniques for Li‑Fi', *ZTE Commun*, vol. 14, no. 2, pp. 29–40, 2016.

[120] RaPSor. http://rapsor.sourceforge.net

[121] J. Lopez-Hernandez, R. Perez-Jimenez, and A. Santamaria, "Modified Monte Carlo scheme for high-efficiency simulation of the impulse response on diffuse IR wireless indoor channels". *Electronics Letters*, 34(19):1819–1820, Sep 1998.

[122] M. I. S. Chowdhury, W. Zhang, and M. Kavehrad, "Combined deterministic and modified Monte Carlo method for calculating impulse responses of indoor optical wireless channels," *J. Light. Technol.*, vol. 32, no. 18, pp. 3132–3148, Sep. 2014.

[123] A. Behlouli, P. Combeau and L. Aveneau, "MCMC Methods for Realistic Indoor Wireless Optical Channels Simulation," in *Journal of Lightwave Technology*, vol. 35, no. 9, pp. 1575-1587, 1 May1, 2017.

[124] S. M. Navidpour, M. Uysal and M. Kavehrad, "BER Performance of Free-Space Optical Transmission with Spatial Diversity," in *IEEE Transactions on Wireless Communications*, vol. 6, no. 8, pp. 2813-2819, August 2007.

[125] T. Fath and H. Haas (2013) Performance comparison of MIMO techniques for optical wireless communications in indoor environments. *IEEE Transactions on Wireless Communications* 61(2):733–742.

[126] A. Goldsmith, *Wireless Communications.* Cambridge University Press, 2005

[127] P. Toumieux. Conception d'un système d'évaluation à distance de la dépense énergétique liée à une activité physique : Application à la supervision de la dépense énergétique de patients en post - AVC. *Thèse de doctorat en Électronique des hautes fréquences, photonique et systèmes Université de Limoges, 2015.*

License CC BY-NC-ND 3.0

[128] http://www.lucibel.io/web/lucibel-btob/etablissement-sante-ehpad-led

[129] D. Wu, Z. Ghassemlooy, W. Zhong, et al “Effect of optimal lambertian order for cellular indoor optical wireless communication and positioning systems”. *Optical Engineering*. 0001; 55(6):066114. 2016

[130] T. Komine and M. Nakagawa, "A study of shadowing on indoor visible-light wireless communication utilizing plural white LED lightings," *1st International Symposium on Wireless Communication Systems, 2004.* Mauritius, 2004, pp. 36-40.

[131] https://mentor.ieee.org/802.11/dcn/18/11-18-1582-04-00bb-ieee-802-11bb-reference-channel-models-for-indoor-environments.pdf

[132] A.S. Glassner, “*Principles of Digital Image Synthesis*”, Morgan Kaufmann Publishers Inc., 1994.

License CC BY-NC-ND 3.0

License CC BY-NC-ND 3.0

APPENDIX 01: Matlab program corresponding to the creation of a scene in RaPSor

```
clear all;
close all;
% ----------Initial attributions for the scene----------
scene.ATTRIBUTE.physics='Light';          % we choose light propagation (not RF)
scene.ATTRIBUTE.script='yes';             % we choose using script in simulation
scene.frequencies=[300000000000000 300000000000000 500];   % generate a frequency flag start stop and step (Hz) corresponding to the frequency range of simulation; this implies that there is the same number of reflectivity coefficient as the frequency number.
scene.area.ATTRIBUTE.noFace='true'; % meaning that we describe the face of environment
scene.area.CONTENT =[-1 -1 8 8]; % Corresponding to the size of RapSor interface
%-----------------------------------------------------------------------------------------------------------
for i=1:1        % i corresponds to the number of scenes we want to create

% ----------Simulation parameters ----------
   scene.simulator.ATTRIBUTE.model='MC Ray Gathering';  % setup the algorithm simulator
   scene.simulator.ATTRIBUTE.mode='SISO';               % or SIMO or MISO
   scene.simulator.nbRay=40000; % number of rays simulated. In this case we took the value equal to 40000 (just an example)
   scene.simulator.nbThreads=9; number considered after zero
   scene.simulator.useDirect='yes'; % means that LOS path is collected;
   scene.simulator.onlyLastReflection='no'; % if yes it's only take the last reflection
   scene.simulator.step=1.5E-10; % time step for each impulse response (s)
   scene.simulator.length=60.0E-9; % duration of the observation (s)
   scene.reflectionNumber=3; % Number of optical reflection
   %-----------------------------------------------------------------------------------------------------------

   % -----Definition of the surface type and reflection coefficients----------
   Rho=0.8;    % value of reflectivity coefficient Rho (in our case we took only one value of rho = 0.8)
   scene.brdf(1).ATTRIBUTE.name='general';       % four side of the room
```


License CC BY-NC-ND 3.0

```
scene.brdf(1).ATTRIBUTE.model='Lambertian';  % model is Lambertian
   scene.brdf(1).rho=Rho;

   scene.brdf(2).ATTRIBUTE.name='ceiling';        %celling of the room
   scene.brdf(2).ATTRIBUTE.model='Lambertian';
   scene.brdf(2).rho=Rho;

   scene.brdf(3).ATTRIBUTE.name='floor';          % floor of the room
   scene.brdf(3).ATTRIBUTE.model='Lambertian';
   scene.brdf(3).rho=Rho;

   scene.brdf(4).ATTRIBUTE.name='body';           % body
   scene.brdf(4).ATTRIBUTE.model='Lambertian';
   scene.brdf(4).rho=0.5;                 % the reflectivity coefficient of the body is set to 0.5.
   %-----------------------------------------------------------------------------------------------------

   % --------------------Moving object parameters----------------------------------------------------
   % the moving object do not only include object's surface but also
   % Transmitter(s)/Receiver(s) that will move with the object.
   %
   scene.receivers.ATTRIBUTE.model='Disc';
% the characteristics of the receivers like positions (m) and direction, and etc,
   posRx =[3.05  3  2.8;     3.05  3.6   2.8;       3.65  3   2.8;        3.65   3.6   2.8];
   dirRx  =[-0.3536  -0.3536  -0.8660;     -0.3536  0.3536  -0.8660;       0.3536  -0.3536  -0.8660;
0.3536 0.3536 -0.8660];   % x=sin(φ)*cos(Θ); y=sin (φ)*sin(Θ); z=cos(φ)
   for iRx=1:4
      scene.receivers.receiver(iRx).position=posRx(iRx, :);
      scene.receivers.receiver(iRx).direction=dirRx(iRx,:);
      scene.receivers.receiver(iRx).area=0.0000345; % Physical surface of receiver in m²
      scene.receivers.receiver(iRx).fov=45;  %Field of View (°)
   end;

   %%                    coordinates (m) of the object in the simulation concern
   Xtrans=0.10;
```


License CC BY-NC-ND 3.0

```
Ytrans=0.53;
Ztrans=1.50;

scene.object.ATTRIBUTE.name ='Object1';
scene.object.color = [1 0 0];                % Color for 3D visualization
scene.object.position = [0 0 0];             % Initial position of the object (m)
scene.object.direction = [1 0 0];            % Initial direction vector of the object

%% parameters of the transmitters
scene.object.Transmitter.ATTRIBUTE.model='Point';          % model of Tx
scene.object.Transmitter.position=[Xtrans Ytrans Ztrans];  % position of Tx (m)
scene.object.Transmitter.direction=[0 0 1];                % direction vector of Tx

directivity = 45;                                          % half power angle in °
transmitter_order= round(-log(2)/log(cosd(directivity))); % lambertian order

scene.object.Transmitter.order=transmitter_order; % Initial transmitter direction
scene.object.Transmitter.m=transmitter_order;

strobject=fileread('body3D.xml'); % load the body 3D environment description (presented in appendix 03 (in this case the file will read the file named “"body3D.xml”))
%-------------------------------------------------------------------------------------------------------
% ----------------------Creation of the xml file-----------------------

xmlstr1 = xml_formatany(scene,'scene');
clear scene

strface=fileread('descrip_room_Exp.xml');        % load the 3D environment description (presented in the appendix 04)

fid=fopen(['scene_test',num2str(i),'.xml'],'wt');          % save the xml file
fprintf(fid,'<?xml version="1.0" encoding="UTF-8"?>');     % mandatory line
fprintf(fid,'%s',xmlstr1((1:length(xmlstr1)-19)));        % include transmitters, receivers and simulator parameters
```


License CC BY-NC-ND 3.0

```
    fprintf(fid,'%s',strobject);                % include if you have a mobile object
    fprintf(fid,'%s',strface);                  % include 3D environment description
    fprintf(fid,'</scene>');                    % instruction to close the scene file
    fclose(fid);
    %--------------------------------------------------------------------
    save(['filename.mat']);                 % save file in the .mat format
end
%----------------------------------------------------------------------
```


License CC BY-NC-ND 3.0

APPENDIX 02: Matlab program to create a script including moving object

```
%                this file allows creating a script run in the RaPSor simulation
% ------------------------------------------------------------------------
clear all;
close all;

% ------------------------------File Header-------------------------------
header = fileread(['header.xml']);      % load the header for the script (it includes the name of the scene that we have created in the appendix 01); presented in appendix 05

fid=fopen(['script_test1.xml'],'wt');              % Create an .xml named script_test

fprintf(fid,'%s',header);                  % write the header in the script_test.xml file

% ------------------------Definition of the objects parameters-----------------------------------
% random position of the objects inside the room, depending on the purpose of simulations
X = 6*rand(10000, 1) + 0.1;            %X varies from 3.3 to 6.4 in our case (m)
Y = 5.9*rand(10000, 1) + 0.1;          %Y is constant since we move along a line (m)
Z = zeros(10000,1) + 1.5;              %we say that the height is constant equal to 1.5m

BodyPositions=[X Y Z]; (m)

for i=1:10000            % Configure the number of simulations
simulation.moveto.ATTRIBUTE.object='Object1';          % Change the position of the object named "Object"
   simulation.moveto.position = BodyPositions(i,:);          % concern all the body positions

   xmlstr1 = xml_formatany(simulation);
   clear simulation
   fprintf(fid,' <simulation>\n');
   fprintf(fid,'%s',xmlstr1((28:length(xmlstr1)-9)));
```


License CC BY-NC-ND 3.0

```
    fprintf(fid,' </simulation>\n');

end
%--------------------------------------------------------------------------
fprintf(fid,'</script>');
fclose(fid);
%--------------------------------------------------------------------------
```


License CC BY-NC-ND 3.0

APPENDIX 03: Description of 3D body

```
<!-- describe a 3D body -->

<face brdf="body">          <!-- the back -->
  <vertices>
    0 0    0
    0 0.5  0
    0 0.5  1.5
    0 0    1.5
  </vertices>
 </face>


<face brdf="body">        <!-- the front -->
   <vertices>
    0.2  0     0
    0.2  0.5  0
    0.2  0.5  1.5
    0.2  0     1.5
   </vertices>
 </face>


<face brdf="body">       <!-- the feet -->
   <vertices>
          0    0     0
          0    0.5   0
          0.2  0.5   0
          0.2  0     0
   </vertices>
 </face>

<face brdf="body">      <!-- left side -->
   <vertices>
     0    0.5    0
     0.2  0.5   0
     0.2  0.5   1.5
     0    0.5   1.5
   </vertices>
 </face>

<face brdf="body">      <!-- right side -->
```


License CC BY-NC-ND 3.0

```
  <vertices>
    0    0    0
    0.2  0    0
    0.2  0    1.5
    0    0    1.5
  </vertices>
</face>

<face brdf="body">      <!-- back neck -->
  <vertices>
    0    0.185   1.5
    0    0.185   1.55
    0    0.265   1.55
    0    0.265   1.5
  </vertices>
</face>

<face brdf="body">      <!-- front neck -->
  <vertices>
    0.20    0.185   1.5
    0.20    0.185   1.55
    0.20    0.265   1.55
    0.20    0.265   1.5
  </vertices>
</face>

<face brdf="body">      <!-- left neck -->
  <vertices>
    0     0.185     1.5
    0.20  0.185   1.5
    0.20  0.185   1.55
    0     0.185     1.55
  </vertices>
</face>

<face brdf="body">      <!-- right neck -->
  <vertices>
    0     0.265     1.5
    0.20  0.265   1.5
    0.20  0.265   1.55
    0     0.265   1.55
  </vertices>
</face>
```


License CC BY-NC-ND 3.0

```
 <face brdf="body">      <!-- top neck -->
  <vertices>
    0    0.185     1.55
    0    0.265     1.55
    0.20 0.265   1.55
    0.20 0.185   1.55
  </vertices>
</face>

<face brdf="body">      <!-- bottom neck -->
  <vertices>
    0     0.185     1.5
    0     0.265     1.5
    0.20  0.265   1.5
    0.20  0.185   1.5
  </vertices>
</face>

 <face brdf="body">      <!-- back head -->
  <vertices>
    0    0.165   1.55
    0    0.165   1.7
    0    0.285   1.7
    0    0.285   1.55
  </vertices>
</face>

<face brdf="body">      <!-- front head -->
  <vertices>
    0.20    0.165   1.55
    0.20    0.165   1.7
    0.20    0.285   1.7
    0.20    0.285   1.55
  </vertices>
</face>

 <face brdf="body">      <!-- left head -->
  <vertices>
    0     0.165   1.55
    0.20  0.165   1.55
    0.20  0.165   1.7
    0     0.165     1.7
  </vertices>
</face>
```


License CC BY-NC-ND 3.0

```
 <face brdf="body">      <!-- right head -->
   <vertices>
     0     0.285     1.55
     0.20  0.285   1.55
     0.20  0.285   1.7
     0     0.285     1.7
   </vertices>
 </face>

 <face brdf="body">      <!-- top head -->
   <vertices>
     0     0.165     1.7
     0     0.285     1.7
     0.20  0.285   1.7
     0.20  0.165   1.7
   </vertices>
 </face>

 <face brdf="body">      <!-- bottom head -->
   <vertices>
     0      0.165     1.55
     0      0.285     1.55
     0.20   0.285   1.55
     0.20   0.165   1.55
   </vertices>
 </face>

</object>
```


License CC BY-NC-ND 3.0

APPENDIX 04: Description of the 3D environment

```
<!-- describe an empty room -->

<face brdf = "floor">          <!-- describe floor -->
   <vertices>
     0    0    0
     0    6.6  0
     6.7  6.6  0
     6.7  0    0
   </vertices>
 </face>

<face brdf = "ceiling">        <!-- describe celling -->
   <vertices>
     0    0    3
     0    6.6  3
     6.7  6.6  3
     6.7  0    3
   </vertices>
 </face>

<face brdf = "general">       <!-- describe the wall side 1-->
   <vertices>
     6.7  6.6  0
     6.7  6.6  3
     0    6.6  3
     0    6.6  0
   </vertices>
 </face>

<face brdf = "general">       <!-- describe the wall side 2-->
   <vertices>
     0    0  0
     0    0  3
     6.7  0  3
     6.7  0  0
   </vertices>
 </face>

<face brdf = "general">      <!-- describe the wall side 3-->
   <vertices>
```


License CC BY-NC-ND 3.0

```
      0   0     0
      0   0     3
      0   6.6   3
      0   6.6   0
    </vertices>
  </face>

<face brdf = "general">      <!-- describe the wall side 4-->
    <vertices>
      6.7   0    0
      6.7   0    3
      6.7   6.6  3
      6.7   6.6  0
    </vertices>
  </face>
```


License CC BY-NC-ND 3.0

APPENDIX 05: Header used in Appendix 02

```
<?xml version="1.0" encoding="UTF-8"?>
<script>
	<scene model="Save Accuracy to XML">
		<inputFile>scene_test1.xml</inputFile> <!-- Include the name of the scene -->
		<outputFile>Output.xml</outputFile>
	</scene>
	<exploitation model="Save Simulation to XML">
		<outputFile>RI_Output.xml</outputFile>
	</exploitation>
```


License CC BY-NC-ND 3.0

APPENDIX 06: Matlab program corresponding to extraction of .xml results from RaPSor

```
% ------------------------------------------------------------------------
clear all;
close all;

% ----------------------Definition of global variables--------------------
nb_points = 4;          % number of receivers in the simulations
nb_files = 10000;       % number of files to extract
reflection_number = 4; % reflection number = LOS + number of reflected path considered
length_RI = 400;        % length of the impulse response

G = zeros(nb_points,nb_files);
H = zeros(nb_points*nb_files,length_RI);
% ------------------------------------------------------------------------

% ---------------------Extraction from the files--------------------------
for n=1:nb_files                % iteration on all the file results from RaPSor

file=xml_load(['Output_Impulse_Response_scene_test1_SimulationNumber',num2str(n),'.xml
'],'off');                      % load the .xml results files from RaPSor. We can change the
directory of the results (./MyDirectory/..../results.xml)

   values = file;
   clear file

   for i=1:nb_points            % track all the receivers

      H_tempo=zeros(1,length_RI);

      for j=1:reflection_number     % total of all the reflection considered (LOS+NLOS)
```


License CC BY-NC-ND 3.0

```
        RI = str2num(values(i).irf.frequency(j).depth);     % refer to each variable in the results
        H_tempo(:)= RI(1:length_RI)+H_tempo;

        clear RI
    end

    G(i,n) = sum(H_tempo);                  % calculate the optical gain
     H(i,:) = H_tempo(1,:);

    % ===============Other informations
    Pos_Rx(i,:) = str2num(values(i).irf.Rx.pos);              % Retrieve Rx or Tx positions
    Orientation_Rx(i,:) = str2num(values(i).irf.Rx.dir);     % Retrieve Rx or Tx orientation
    end

end
% ------------------------------------------------------------------------
```

% ----------Clear useless information----------

```
clear nb_points
clear nb_files
clear length_RI
clear H_tempo
clear values
clear reflection_number
clear i
clear j
clear n
% ------------------------------------------------------------------------
```

% ----------Save the data in .mat file----------

```
save ('filename.mat');           %
% ------------------------------------------------------------------
```


License CC BY-NC-ND 3.0

APPENDIX 07: Figures of Chapter V for 60° oriented receivers

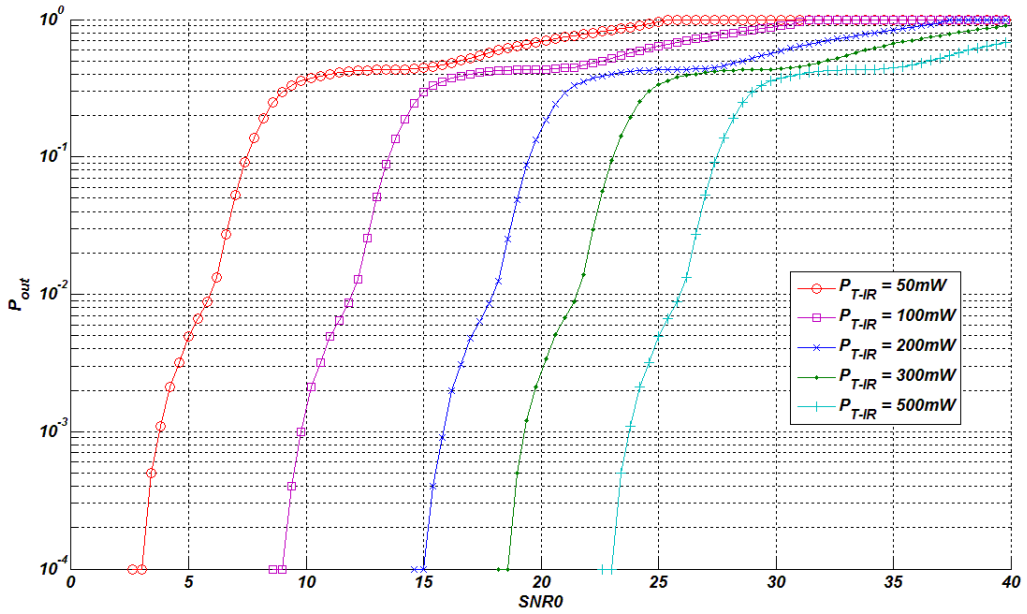

Figure corresponding to 5.5. Outage probability of IR channel scenario (b), Rx orientation 60°, m=2, $H_{t-IR} = 0.2m$, body reflectivity ρ=0.1; ; $R_b = 1Mbps$

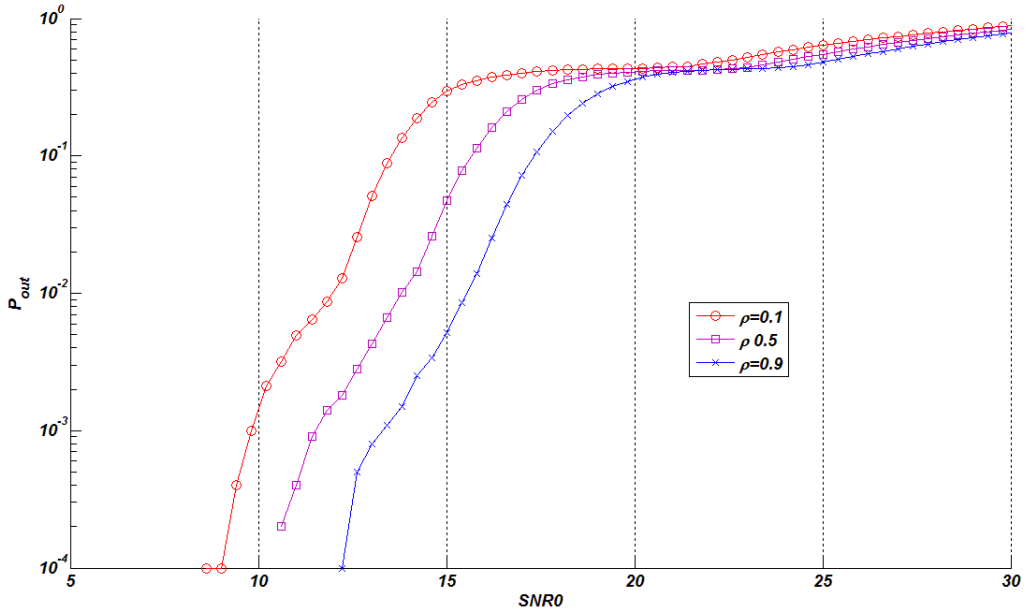

Figure corresponding to 5.6. Outage probability of IR channel scenario (b), Rx orientation 60°, m=2, $H_{t-IR} = 0.2m$, $P_{t-IR} = 100mW$;body reflectivity ρ=0.1;0.5;0.9; ; $R_b = 1Mbps$

License CC BY-NC-ND 3.0

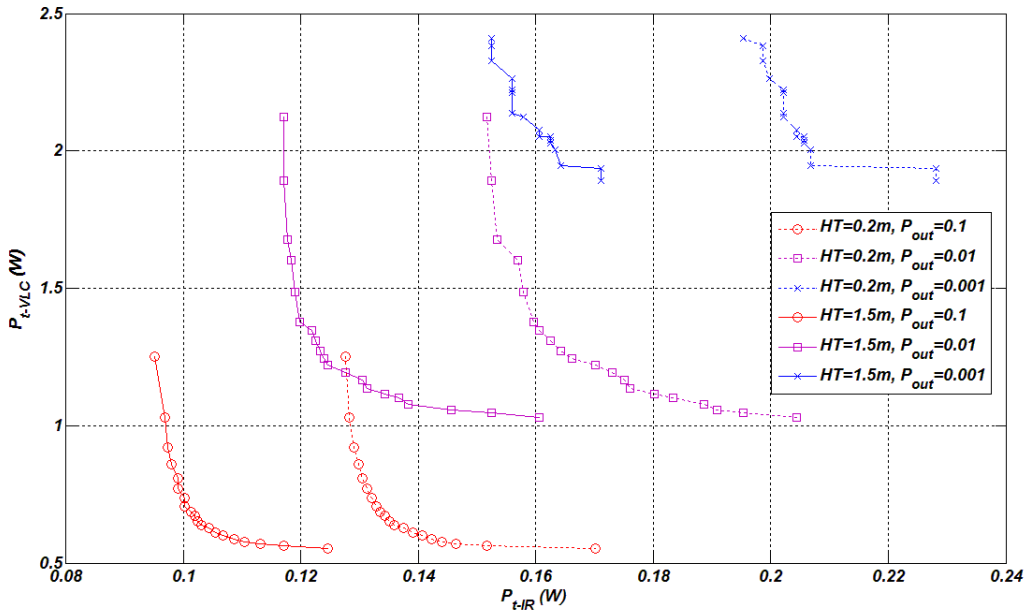

Figure corresponding to 5.9. Evolution of IR and VLC emitted powers for 3 given values of P_{out} ; Rx orientation 60°, m=2, body reflectivity ρ=0.1, Height H_{T-IR}=0.2m andH_{T-IR}=1.5m; data rate $R_b = 1Mbps$.

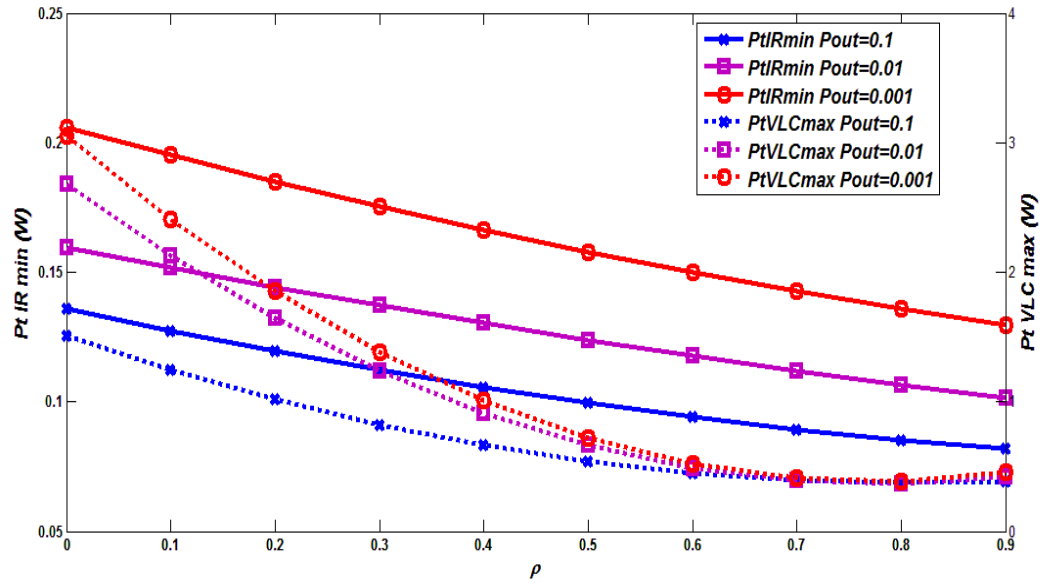

Figure corresponding to 5.10. Evolution of, $P_{t-IR-min}$ (in plain lines) and $P_{t-VLC-max}$ (in dotted lines) for 3 given values of P_{out} as a function of body reflectivity ρ Height H_{T-IR} =0.2m; Rx orientation 60°, $R_b = 1Mbps$.

License CC BY-NC-ND 3.0

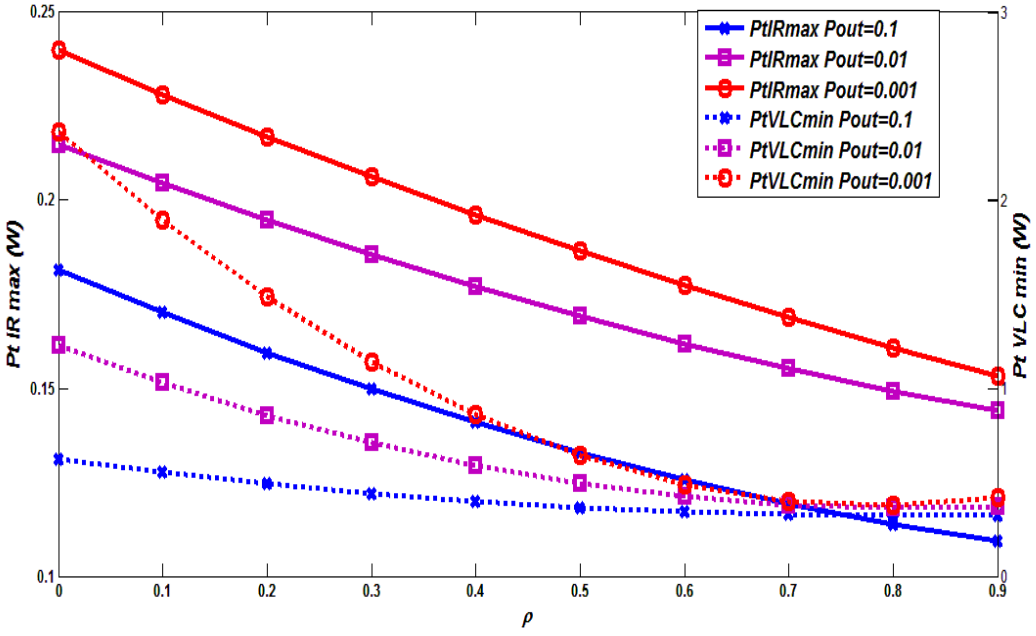

Figure corresponding to 5.11. Evolution of, $P_{t-IR-max}$ (in plain lines) and $P_{t-VLC-min}$ (in dotted lines) for 3 given values of P_{out} as a function of body reflectivity ρ, Rx orientation 60°, Height H_{T-IR}=0.2m; $R_b = 1Mbps$.

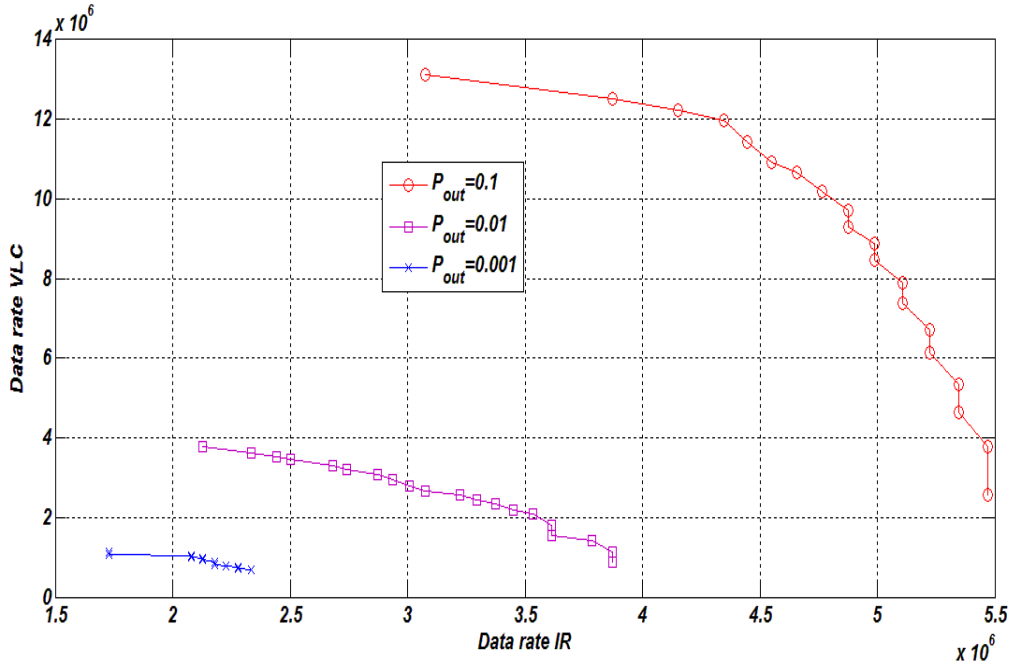

Figure corresponding to 5.12. Evolution of, data rate for IR and VLC links for 2 given values of P_{out} ; P_{t-IR}=300mW and P_{t-VLC}=2W ; Rx orientation 60°, body reflectivity ρ=0.1, Height H_{T-IR}=0.2m

License CC BY-NC-ND 3.0

[Technologie Optique Sans Fil Infrarouge et Visible pour la Connectivite de Capteurs Corporels]

Résumé: Cette thèse est axée sur le domaine de la communication optique sans fil en intérieur pour la surveillance de la santé basée sur des capteurs corporels. L'état de l'art des communications optique sans fil dans les domaines infrarouge, visible et UV ainsi que l'analyse des systèmes liés à la santé utilisant cette technologie ont été fournis. Cela a permis de définir les objectifs et l'orientation de cette thèse. Nous avons étudié l'utilisation de la technologie infrarouge pour la transmission de données entre un capteur porté par un patient et des récepteurs situés aux coins d'un panneau d'éclairage central au plafond de l'environnement. Un lien en visible a été utilisé pour la transmission de données du luminaire vers le patient portant un smartphone équipé d'un décodeur. Les principaux défis étaient la robustesse des liens infrarouge et visible en ce qui concerne la mobilité du patient et l'impact du corps de l'utilisateur en raison de l'emplacement du capteur. Les simulations de canaux réalisées grâce à la technique de Ray-Tracing associée à la méthode de Monte-Carlo ont permis de déterminer le gain de canal qui est le paramètre principal représentant la performance. En raison de la mobilité du patient, l'analyse a été réalisée de manière statistique et en tenant compte de différents emplacements du capteur sur le corps, de la cheville à l'épaule. Les paramètres physiques et géométriques optimaux relatifs aux émetteurs et aux récepteurs afin de garantir les meilleures performances ont été déduites. Il a été démontré qu'il est essentiel de modéliser la présence du corps pour les deux liaisons montante et descendante. Les performances globales du système ont mis en évidence le potentiel des transmissions sans fil entièrement optiques pour la surveillance médicale basée sur des capteurs corporels. Cela a été en partie confirmé par des expérimentations menées à partir de prototypes de capteur communicant en infrarouge et de produits commerciaux pour la liaison en visible.

Mots-clés: Communication optique sans fil, Infrarouge, Visible, Surveillance en santé, capteur corporel

[Infrared and visible wireless optical technology for body sensor connectivity]

Summary: This thesis is focused on the field of indoor optical wireless communication for health monitoring based on body sensors. The state of the art of optical wireless in the infrared, visible and UV domains as well as the analysis of health related systems using this technology have been provided. This helped to define the objectives and orientations of this thesis. We have studied the use of infrared technology for data transmission between a sensor worn by a patient and receivers located at the corners of a central lighting panel at the ceiling of the environment. A link in visible was used for the transmission of data from the luminaire to the patient carrying a smartphone equipped with a decoder. The main challenges were the robustness of the infrared and visible links with regard to patient mobility and the impact of the user's body due to the location of the sensor. The channel simulations performed using the Ray-Tracing technique associated with the Monte-Carlo method allowed determining the channel gain, which is the main parameter representing the performance. Due to the patient mobility, the analysis was performed statistically and taking into account different locations of the sensor

on the body, from the ankle to the shoulder. The optimal physical and geometrical parameters for transmitters and receivers to ensure the best performance have been deduced. It has been shown that it is essential to model the presence of the body for both uplink and downlink. The overall performance of the system has highlighted the potential of fully optical wireless transmissions for medical surveillance based on body sensors. This has been partly confirmed by experiments carried out from infrared communicating sensor prototypes and commercial products for the visible link.

Keywords: Optical Wireless Communication, Infrared, Visible Light Communication, Healthcare Monitoring, Body sensor